SURFACE THERMODYNAMIC PROPERTIES OF SUBSURFACE COLLOIDS

By

JIANYING SHANG

A dissertation submitted in partial fulfillment of
the requirements for the degree of

DOCTOR OF PHILOSOPHY

WASHINGTON STATE UNIVERSITY
Department of Crop and Soil Sciences

August 2008

To the Faculty of Washington State University:

The members of the Committee appointed to examine the dissertation of JIANYING SHANG find it satisfactory and recommend that it be accepted.

_____

Chair

_____

_____

Acknowledgements

I want to express my gratitude and appreciation to many people who gave me their support, friendship, encouragement and guidance. I would first like to thank my major advisor, Dr. Markus Flury, for his guidance, support, inspiration, patience, and encouragement. He has taught me how to solve a challenging problem, how to write a scientific paper, and how to be a better scientist, which are beneficial to me in my whole life. Without his assistance and supervision, this research and dissertation would not be accomplished.

I would like to thank my committee Dr. James B. Harsh and Dr. Richard L. Zollars for providing their scientific expertise, valuable advice, and guidance. Their advice and suggestions helped me to improve the quality of the research I performed. I acknowledge the assistance from Jon Mathison and Jeffrey Boyle for their technical support and suggestions during my experiments. I am extremely grateful to Dr. Youjun Deng and Dr. Geng Chen for their help with the experiments. I wish to express my gratitude to Dr. Joan Wu, Dr. William Pan, Dr. Alan Busacca, Dr. John Reganold and Dr. Lynne Carpenter-Boggs for their help and encouragement during my studies. Thanks are also given to my fellow lab-mate Prabhakar Sharma, and Shuhui Dun for discussion and help during my studies.

Finally, I would like to give my deepest gratitude to my parents, who give their largest support through my education, and family members Kesi, Jianhui, Dong, Jianhong, Jun for their support, understanding, and encouragement.

SURFACE THERMODYNAMIC PROPERTIES OF SUBSURFACE COLLOIDS

Abstract

by Jianying Shang, Ph.D.

Washington State University

August 2008

Chair: Markus Flury

Thermodynamic properties of subsurface colloids are important information for understanding a variety of phenomena, such as adhesion, flotation, mobility, fate, and transport of various colloids in the unsaturated subsurface environments. The goal of this research was to study contact angles of subsurface colloids and to elucidate the mechanism of colloid mobilization in unsaturated porous media. The main objectives were as follows:

1. To investigate the impact of water content during infiltration in porous media on colloid release patterns, rates, and quantity, and to elucidate the dominant colloid release mechanisms.

2. To compare different experimental methods to determine contact angles of subsurface colloids.

3. To investigate the effects of cations and humidity on contact angles and surface tensions of subsurface colloids.

4. To clarify the role of a moving air-water interface on colloid mobilization in porous media.

We conducted experiments on *in situ* colloid mobilization under transient conditions using columns repacked with sediments. The cumulative amount of colloids released was proportional to the column water content established after steady-state flow rates were achieved. According to DLVO theory and the Young-Laplace equation, the electrostatic, van der Waals, hydrodynamic, and capillary forces exerted on colloids were calculated and used to analyze the experimental results.

Five different methods, static sessile drop, dynamic sessile drop, Wilhelmy plate, thin-layer wicking, and column wicking, were used to measure the contact angles of subsurface colloids. The colloids were deposited on glass slides to make thin films. The colloidal films can be categorized into three types: (1) films without pores and with polar-liquid interactions (smectite), (2) films with pores and with polar-liquid interactions (kaolinite, illite, goethite), and (3) films without pores and no polar-liquid interactions (hematite). Based on our results, we could recommend specific methods for different colloids.

The effects of surface and interlayer cations, and relative humidity on contact angle measurements of colloids were investigated using the sessile drop method. Surface tension components and parameters of the colloids were calculated from contact angles

using the Lewis acid-base approach. The effects of cations and relative humidity were reflected in the surface tension components of the colloids.

To quantify the forces acting on a solid particle when an air-water interface passes over the particle, we used a tensiometer to measure the forces between the particle and the air-water interface. Theoretical calculations using the Young-Laplace equation were used to support the experimental data and conclusions. The theoretical forces as a function of ζ-potential, particle radius, and contact angle were calculated to unveil the mechanistic principle of colloid mobilization in the vadose zone.

Table of Contents

List of Tables

List of Figures

Chapter 1

Introduction

1.1 Background

Surface tension is a fundamental thermodynamic property in surface and interfacial sciences, and important for understanding a variety of phenomena, such as capillarity, adhesion, wetting and flotation. In subsurface hydrology, the surface tension plays an important role in water infiltration, and recently, has also been found significant to understand colloid fate and transport. The surface tension, as understood in this dissertation, relates to the energy per surface area, and applyies to liquids and solids. Surface tension of subsurface colloids provides useful information to study surface and interfacial interactions at the micro-scale. In a three phase contact situation (gas-liquid-solid), the surface tensions are usually balanced, and the force balance gives rise to a characteristic contact angle. This latter force balance is usually expressed in form of the Young Equation.

Surface tension is also an important property of subsurface particles. Colloid mo-

bilization and transport in partially saturated systems is a challenging topic that will lead us to better understand contamination problems. Surface tension and contact angle are helpful to determine how colloids interact with each other and other surfaces, such as solid surfaces and liquid-gas interfaces. Capillary forces controlled by the air-water interface and determined by surface tension and contact angle can immobilize colloids [*Wan and Tokunaga,* 1997*; Veerapaneni et al.,* 2000]. Field studies in the vadose zone showed that colloid mobilization coincides with increasing water flux [*El-Farhan et al.,* 2000*; Petersen et al.,* 2003]. Drying and rewetting processes also influence colloid release and retention during unsaturated flow [*El-Farhan et al.,* 2000]. The relationships among surface tension, contact angle, capillary force, colloid mobilization are important to understand the actual mechanisms of *in situ* colloid mobilization and transport in natural soils.

The solid surface tension is difficult to determine directly, and is usually obtained by indirect measurements. The measurement methods include particle sedimentation, capillary penetration into powders, contact angle measurements, film flotation [*Kwok and Neumann,* 1999]. Theoretical approaches have been developed, which include theory of molecular interactions and Lifshitz-vander Waals forces [*van Oss,* 2006]. The most common methods to determine solid surface tension are contact angle measurements.

The contact angle of subsurface colloids can be determined using several methods, including sessile or pendant drop and Wilhelmy plate methods. Wicking or capil-

lary rise method are used to measure contact angle for porous materials according to capillary theory [*Chibowski and Perea-Carpio,* 2002]. Force measurements [*Zhang et al.,* 1996*; Preuss and Butt,* 1998c], confocal microscopy [*Mohammadi and Amirfazli,* 2004], and film trapping [*Hadjiiski et al.,* 1996] have been used to determine contact angle for spherical colloidal particles. However, many of these methods are difficult to use with subsurface colloids, because subsurface colloids have heterogeneous surfaces, are variably charged, and cannot be prepared in a standardized manner for repeatable measurements. In addition, interactions between the fluid used to measure the contact angle and the solid itself can cause the contact angle to change with time. Therefore, a systematic evaluation and comparison of methods to determine contact angles of subsurface colloids is needed.

Measuring contact angles is a nontrivial, mainly owing to the large number of conditions that affect the measurements. Temperature [*King,* 1981*; Dekker et al.,* 1998*; She and Sleep,* 1998*; DeJonge et al.,* 1999], water content [*DeJonge et al.,* 1999*; Dekker and Ritsema,* 2000*; deJonge et al.,* 2007*; Bachmann et al.,* 2007], organic matters [*Woche et al.,* 2005], particle size [*DeJonge et al.,* 1999], surface roughness [*Eick et al.,* 1975*; Oliver et al.,* 1980*; Drelich et al.,* 1996], heterogeneous surface [*Johnson and Dettre,* 1964*; Dettre and Johnson,* 1965*; Long et al.,* 2005], and surface cations [*Chibowski et al.,* 1993*; Breiner et al.,* 2006] all have effects on contact angles. Little is known, however, about the effects of relative humidity and cations on clays. It is expected that the precise effects of relative humidity and cations on contact angles,

surface tensions, and interaction energies of subsurface colloids can be assessed by careful experimentation with changing humidity and cations.

To understand the actual mechanisms of *in situ* colloid mobilization and transport in natural soils, the relationships among contact angle, capillary force, colloid mobilization and transport need to be studied to illustrate the significant role of capillary force. Using tensiometry [*Zhang et al.,* 1996*; Zhang et al.,* 1997], the capillary forces acting between a particle and a liquid-gas interface can be measured and calculated. Using the Laplace equation [*Princen,* 1969*; Zhang et al.,* 1996*; Zhang et al.,* 1997*; Zhang et al.,* 1999], the capillary forces at the liquid-gas interface can be quantified. Force measurements and theoretical calculations will directly provide evidence for the importance of the capillary forces for colloid release from sediments.

The fate and mobility of colloid in vadose zone is a challenging environmental problem. Mobile colloidal particles can accelerate the movement of contaminants [*Grolimund et al.,* 1996*; Ryan et al.,* 1998]. Further knowledge and understanding of the relationships among surface tension, contact angle, and capillary force can help to unveil the mechanisms of *in situ* colloid mobilization in unsaturated system.

1.2 Objectives

The goal of this dissertation is to identify the dominant *in situ* colloid release mechanisms in partial-saturated system. To achieve this goal, we conducted *in situ* colloid mobilization and transport experiments using column techniques, evaluated the sur-

face tension characteristics of subsurface colloids, and examined capillary forces, by force measurements and theoretical numerical simulations. The specific objectives of these studies are as follows:

1. To assess the potential of *in situ* colloid mobilization from natural sediments under transient flow conditions and to investigate the impact of water content (or flow rate) during infiltration on colloid release patterns, colloid release rates, and colloid release quantities, with the purpose to identify colloid release mechanisms.

   We studied *in situ* colloid mobilization under transient flow conditions using columns repacked with Hanford sediments. Five series of column experiments were performed with initial infiltration rates of 0.018, 0.036, 0.072, 0.144 and 0.288 cm/min. We also estimated forces exerted on the colloids, including electrostatic, van der Waals, hydrodynamic, and capillary forces.

2. To compare different methods to determine contact angles of subsurface colloids.

   We used the sessile drop, Wilhelmy plate, capillary rise (column wicking), and thin-layer wicking methods to determine contact angles of five major types of subsurface colloids (swelling and non-swelling aluminosilicate clays, and (hydr)-oxides). We discuss advantages and disadvantages of the different methods, and make recommendations on the optimal methods of contact angle measurement for specific subsurface colloids.

3. To investigate the effects of different cations, and relative humidity on contact

angles and surface tensions of subsurface colloids.

The contact angles and surface tensions of three aluminosilicate clays, smectite, kaolinite, and illite, with four cations Na^+, K^+, Mg^{2+}, and Ca^{2+} were compared using the static sessile drop method, and the effects of four different relative humidities on contact angles were discussed.

4. To quantity the forces acting on a solid particle when an air-water interface passes over the particle, and to classify the role of a moving air-water interface on colloid mobilization in porous media.

   We quantified, both experimentally and theoretically, the forces acting on particles of different shape and discussed the implications for colloid mobilization under unsaturated flow conditions in porous media.

1.3 Thesis Outline

This dissertation includes an introduction, four major technical chapters, and a conclusion. One chapter has been accepted by a technical journal, another chapter has been submitted as technical paper, and two chapters have been prepared for submission to technical journals. Chapter 1 gives a brief introduction and the main objectives of the dissertation. In chapter 2, *in situ* colloid mobilization from natural sediments under transient flow conditions are investigated, and colloid release mechanisms are discussed. Chapter 3 reports on using different methods to determine contact angles

of five major types of subsurface colloids. The advantages and disadvantages of the different methods are discussed to give recommendations on the optimal methods for subsurface colloid contact angle determination. Chapter 4 deals with the effects of relative humidity and cations on contact angles and surface tensions, which are little known for subsurface colloids. Chapter 5 discusses the forces acting on particles of different shape at the liquid-gas interface by experimental and theoretical methods, and presents the important role of capillary forces for colloid mobilization in the vadose zone. In chapter 6, the major conclusions of the dissertation are given. Tables and figures are presented at the end of each chapter, conforming to the format for paper submission to a technical journal. Additional information on experimental procedures and supporting experiments, supportive data, and figures are included as Appendices in the related chapters. References are listed together at the end of the dissertation.

Chapter 2

Impact of Flow Rate, Water Content, and Capillary Forces on *In Situ* Colloid Mobilization during Infiltration in Unsaturated Sediments

2.1 Abstract

We studied *in situ* colloid mobilization under transient flow conditions using columns repacked with Hanford sediments. Rainfall infiltration was experimentally simulated using different flow rates and initial moisture conditions. Five series of column experiments were performed with initial infiltration rates of 0.018, 0.036, 0.072, 0.144 and 0.288 cm/min. The degree of water saturation ranged from 53 to 81%. The chemical

This chapter has been published: Shang, J., M. Flury, G. Chen and J. Zhuang, Impact of Flow Rate, Water Content, and Capillary Forces on In Situ Colloid Mobilization during Infiltration in Unsaturated Sediments, Water Resources Research, 44, DOI10.1029/2007WR006516, 2008.

conditions were unfavorable for colloid attachment to the sediments. Colloids were eluted by the infiltrating water with the peak colloid concentrations in the outflow coinciding with the arrival of the infiltration front. A larger flow rate led to a greater amount of colloids released from the column. The cumulative amount of colloids released was proportional to the column water content established after steady-state flow rates were achieved. We used the advection-dispersion equation with a first-order colloid release reaction to analyze the experimental data. The colloid release rate coefficient increased with the increase of water content. We calculated forces exerted on colloids, and found that electrostatic and van der Waals interactions, calculated based on the DLVO theory, and hydrodynamic forces, were all less important than capillary forces in controlling colloid release. In one experiment, the ionic strength of the infiltration solution was increased, such that colloid attachment was favorable. Nonetheless, colloids were mobilized and eluted with the infiltration front, implying that non-DLVO forces, such as capillary forces, played a prominent role in colloid mobilization.

2.2 Introduction

In situ colloid mobilization and transport has been extensively studied in different geological formations under both water saturated [*Ryan and Elimelech*, 1996*; Grolimund and Borkovec*, 1999*; Lenhart and Saiers*, 2003] and unsaturated conditions [*Ryan et al.*, 1998*; Laegdsmand et al.*, 1999*; Cherrey et al.*, 2003*; de Jonge et al.*, 2004]. In satu-

rated systems, the master variables controlling *in situ* colloid mobilization are solution ionic strength and pH [*Kretzschmar et al.*, 1999].

In the vadose zone, colloid mobilization is also controlled by the air-water interface. The air-water interface can cause strong capillary forces that can immobilize colloids [*Zimon*, 1969; *Wan and Tokunaga*, 1997; *Veerapaneni et al.*, 2000]. To understand the actual mechanisms of *in situ* colloid mobilization and transport in natural structured soils, researchers used undisturbed soil columns to study naturally occurring particles [*de Jonge et al.*, 1998; *Laegdsmand et al.*, 1999; *Petersen et al.*, 2003]. It has been postulated that *in situ* colloid mobilization from undisturbed, macroporous soils is controlled by two rate-limiting processes: a release of colloids from the soil matrix to the crust of macropore walls and diffusion of these colloids through a layer of immobile water lining the macropore [*Schelde et al.*, 2002]. Field studies in the vadose zone have also demonstrated that greater colloid mobilization coincides with increasing water flux [*Ryan et al.*, 1998; *El-Farhan et al.*, 2000; *Petersen et al.*, 2003].

Mechanical energy of moving water imposes a shear stress on the colloids, which can result in the release of colloidal particles. If the moving water imposes a torque such that shear forces exceed the forces that attach colloids to the sediments, colloids are released [*Ryan et al.*, 1998]. Increase in velocity will increase shear forces and consequent colloid release. There are studies supporting that under saturated conditions the amount of colloidal particles released is directly related to the flow rate [*Kaplan et al.*, 1993; *Gschwend et al.*, 1990]. On the other hand, the role shear forces play in

colloidal release under unsaturated flow conditions remains unclear. Experiments by *Levin et al.* [2006] suggested that colloid mobilization from an undisturbed soil core was mainly controlled by the number of pores that contributed to water flow and less by shear forces.

Several studies have indicated that colloids can associate to air-water interfaces [*Scheludko et al.*, 1976; *Preuss and Butt*, 1998a; *Wan and Tokunaga*, 1998] or be strained in water films thinner than the colloid diameters [*Wan and Tokunaga*, 1997]. Upon mobilization of these air-water interfaces, colloids can be released and transported [*Gao et al.*, 2006]. It was also proposed that colloids in unsaturated porous media preferentially associate with the air/water/solid interface [*Crist et al.*, 2005], or more precisely the air/water meniscus/solid interface, i.e., where the water film thickness approaches the size of the colloidal particles [*Chen and Flury*, 2005; *Zevi et al.*, 2005]. When water films expanded by re-saturating the sediments, retained colloids could be quantitatively recovered in the column outflow, showing that the retention of the colloids was reversible and mainly controlled by the degree of water saturation [*Chen and Flury*, 2005; *Crist et al.*, 2005], an interpretation supported by pore-scale mobilization studies [*Gao et al.*, 2006]. Increasing water saturation has consistently been shown to lead to increased colloid mobilization (e.g., *Saiers and Lenhart*, 2003; *Chen and Flury*, 2005; *Gao et al.*, 2006).

Drying and rewetting also influence colloid release and retention during unsaturated flow. *El-Farhan et al.* [2000] observed the greatest colloid flux following infiltration

into a dry soil, and smaller colloid fluxes when the soil was wet. The effect of wetting and drying may be different depending on soil texture. *Kjaergaard et al.* [2004] found little differences of colloid release in highly clayey soils (43% clay) at three distinctly different water contents, but large differences when the clay contents were smaller (12% clay). It was also reported that the duration of drying affects colloid mobilization [*Majdalani et al.*, 2007]. *Totsche et al.* [2007] reported that during a field study, colloid mobilization was maximal after high-intensity rainfall following an extensive drying period. Although drying often leads to increased hydrophobicity of the soil matrix [*Dekker et al.,* 2001], it may not necessarily also lead to increased hydrophobicity of dispersible colloids [*Klitzke and Lang,* 2007].

In natural soils, colloid release is affected by the presence of organic matter. Increased amount of organic matter usually leads to an increase of aggregate stability, and a decrease of colloid dispersibility [*Chenu et al.*, 2000]. On the other hand, dissolved organic matter enhances the stability of colloidal suspensions, leading to increased colloid mobility [*Kretzschmar et al.,* 1995*; Kaplan et al.,* 1997]. From leaching experiments, it was reported that soils with higher organic matter content showed more colloid release than soils with lower organic matter content, which is likely caused by increased amount of dissolved organic matter [*Laegdsmand et al.,* 2005]. It is often observed that dissolved organic matter flushes out of soil with the first infiltration front, and then its concentration decreases rapidly [*Kaiser and Zech,* 1998*; Cooper et al.*, 2007*; Totsche et al.,* 2007].

The colloid release has often been modeled by the advection-dispersion equation with a first-order colloid release [*Ruckenstein and Prieve,* 1976*; Dahneke,* 1975*; Roy and Dzombak,* 1996]. First-order colloid release should be valid if the colloid detachment step is rate-limiting [*Kretzschmar et al.,* 1999]. Researchers used the rate-limited model with a first-order diffusive mass transfer to describe *in situ* colloid release from intact soil columns [*Schelde et al.,* 2002*; Kjaergaard et al.,* 2004]. Grolimund and Borkovec [*Grolimund and Borkovec,* 1999*; Grolimund et al.,* 2001] observed that colloid release from packed natural soil materials did not follow simple first-order kinetics, but rather multiple first-order kinetics. Using unsaturated re-packed quartz sand columns with pre-deposited colloids, it was postulated that the first-order colloid release rate coefficients depend in an exponential fashion on the colloid concentration of the sediments [*Lenhart and Saiers,* 2003].

Saiers and Lenhart [2003] observed in a column experiment where colloids were initially deposited on a clean silica sand, that increasing the water flow rate led to colloid mobilization. At a given flow rate, only a limited amount of colloids could be released, but subsequent increases in flow rates led to additional colloid release. *Saiers and Lenhart* [2003] proposed that colloids are released from distinct compartments, each of which releases colloids at a critical moisture content. This concept was successfully applied to describe colloid mobilization from sand columns [*Saiers and Lenhart,* 2003*; Gao et al.,* 2004]. That transient flow enhances colloid mobilization compared to steady-state flow was also observed by *Zhuang et al.* [2007]. In these latter exper-

iments, not only infiltration but also drainage led to mobilization of colloids [*Zhuang et al.*, 2007].

There is evidence that colloid mobilization during unsaturated flow is controlled by capillary forces that act between colloids and the air-water interface. *Sharma et al.* [2008] used flotation-type of experiments where unsaturated sediments were infiltrated from the bottom with solutions of various ionic strengths, and they observed that colloids preferentially attached to the air-water interface.

Here we report on colloid mobilization from natural sediments. Our overall objective was to assess the potential of *in situ* colloid mobilization from natural sediments under transient flow conditions. We experimentally simulated rainfall infiltration into sediment columns. Our specific objectives were to investigate the impact of water content (or flow rate) during infiltration on (1) colloid release patterns, (2) colloid release rates, and (3) colloid release quantities, with the purpose to identify colloid release mechanisms. The dominant colloid release mechanisms were elucidated by estimating forces exerted on the colloids, including electrostatic, van der Waals, hydrodynamic, and capillary forces.

2.3 Materials and Methods

2.3.1 Sediments and Sediment Characterization

Hanford sediments used in this research were obtained from the Hanford Environmental Restoration Disposal Facility (ERDF), located 8 miles from the Columbia River between the 200 East and 200 West Areas of the Hanford Site (southcentral Washington State, USA). The sediments were collected from 17-m depth below surface, and were similar to those used in previous colloid mobilization experiments [*Zhuang et al.,* 2007]. The sediments were air-dried and then sieved through a 20-mm square screen to remove the few big pebbles. The pH of the sediments in water was 8.9 using a soil-to-solution ratio of 1:2.5 by weight. The cation exchange capacity was 25.4±0.4 $mmol_c$/kg, and the base saturation was 87.2%, with the following cation distribution: 14.1 $mmol_c$/kg Ca, 5.7 $mmol_c$/kg Mg, 1.1 $mmol_c$/kg Na, and 1.3 $mmol_c$/kg K. The mineralogical composition of bulk Hanford sediments includes quartz, feldspar, mica, magnetite, pyroxene, hornblende, kaolinite, illite, and smectite; the colloidal fraction consisted mainly of quartz, kaolinite, illite, and smectite [*Mashal et al.,* 2004*; Czigany et al.,* 2005]. The geometric mean grain size was 797 μm, and the sand, silt, and clay fractions were 92%, 6%, and 2% by weight, respectively. The specific surface area of the sediments, determined by BET gas adsorption using N_2 (ASAP2010, Micromeritics, Norcross, GA), was 4.7±0.3 m^2/g. The carbon content of the sediments was determined by combusting air-dried sediment samples at 1350^{o}C and quantify-

ing the resulting CO_2 using IR radiation (LECO CNS-2000, Carbon, Nitrogen, and Sulfur Analyzer, LECO Corp., St. Joseph, MI). The inorganic carbon content was determined by first heating the samples to 600^oC to remove organic carbon, and than analyzing the remaining carbon content with the CNS-analyzer. The organic carbon content of the sediments was 146±85 mg/kg, calculated from the difference between total and inorganic carbon content.

Before packing into the column, the sediments were moisturized to a volumetric water content of 0.09 cm^3/cm^3, by thoroughly mixing the appropriate amount of water with air-dry soil. This moisturizing ensured that the initial water content in the column was uniform, and also helped to bind fine material to the coarse fraction of the sediments. Moisturized sediments were uniformly packed into an air-filled acrylic column of 5-cm i.d. × 30-cm length. The bulk density of the packed sediments was 1.57 g/cm^3.

2.3.2 Column Transport Experiments

Column experiments were conducted with the column vertically oriented, and inflow was applied using a sprinkler consisting of 12 hypodermic needles (30-gauge) and a peristaltic pump. The bottom of the column was equipped with two layers of a nylon membrane (500 mesh, 25 μm pore opening, Gilson Company, Lewis Center, OH). The pore opening was confirmed by scanning electron microscopy. The nylon membrane had a bubbling pressure of -75 cm-H_2O as measured experimentally. Five 3-mm

diameter holes were evenly distributed along the perimeter 2 cm above the bottom of the column to allow air to escape during infiltration. The column itself was mounted on an electronic load-cell to monitor the overall gravimetric water content. A constant tension of -10 cm-H_2O was maintained at the bottom of the column using a hanging water column. Column outflow was collected with a fraction collector.

We monitored the matric potential inside the column with five tensiometers (PX170-28DV, Omega Engineering, Inc., Stamford, CT), which were evenly aligned along the length of the column and connected to a Campbell Scientific CR-7X datalogger (Campbell Scientific, Inc., Logan UT). Five 3-rod time domain reflectometer (TDR) probes were mounted horizontally at the same elevation as the five tensiometers. These TDR probes were made of $1/6''$ stainless steel rods, 5.5 cm long, and connected to a TDR100 system (Campbell Scientific, Inc.). The TDR probes were individually calibrated with the Hanford sediments.

We used deionized water (pH 7, electrical conductivity 1 μS/cm) as the infiltrating solution. Infiltration experiments were conducted with different flow rates and by sequentially increasing the flow rates (and consequently increasing the water contents). We conducted the following 5 series of column experiments: Series 1: initial flow rate of 0.018 cm/min, then step-wise increase of the flow rate to 0.036 cm/min, 0.072 cm/min, 0.144 cm/min and 0.288 cm/min; Series 2: initial flow rate of 0.036 cm/min, then step-wise increase to 0.072 cm/min, 0.144 cm/min and 0.288 cm/min; Series 3: initial flow rate of 0.072 cm/min, then step-wise increase to 0.144 cm/min and 0.288

cm/min; Series 4: initial flow rate of 0.144 cm/min, then increase to 0.288 cm/min; Series 5: flow rate of 0.288 cm/min. For each flow rate, the flow was kept steady-state, with inflow equal outflow rate, for an extensive period of time until colloid outflow concentrations stabilized, then the flow rate was increased to the next level. For each of the 5 series, a new sediment column was used.

We measured effluent pH, electrical conductivity, colloid concentrations, electrophoretic mobilities, average colloid sizes, and dissolved organic carbon content. No flocculation of colloids was observed visually in the effluent. Colloid concentrations were determined by turbidity measurements (HP8452A Diode Array Spectrophotometer) at a wavelength of 300 nm and electrophoretic mobilities and colloid sizes were measured by dynamic light scattering (Zetasizer 3000HAS, Malvern Instruments Ltd., Malvern, UK). A colloid concentration calibration curve was obtained by using colloids fractionated from Hanford sediments as source colloids. To fractionate these source colloids, we dispersed the Hanford sediments in deionized water. Supernatant was decanted and centrifuged at 3000 g for 15 min to separate particles smaller than 1 μm in diameter, which were then used to determine a calibration curve. The concentration of dissolved organic carbon was determined with a Shimadzu TOC-Vcsh total organic carbon analyzer (Shimadzu, Osaka, Japan) after acidification to remove inorganic carbon.

Infiltration of deionized water creates chemical conditions unfavorable for colloid attachment, thereby favorable for colloid mobilization. To test colloid mobilization under favorable attachment (or unfavorable mobilization conditions), we increased the

ionic strength of the infiltration solution with 0.5 M $CaCl_2$. For these experiments, we used flow rates of 0.018, 0.036, 0.072, 0.144, and 0.288 cm/min, each with newly packed sediments.

All experiments were repeated twice. Data showed good reproducibility; an example of colloid release breakthrough curves for Series 2 is shown in Figure 2.1. Only one of the two replicates is shown in the remaining figures. A dye tracer test, using Brilliant Blue FCF as tracer [*Flury and Wai,* 2003], was conducted to examine whether the infiltration front developed preferential flow pathways. We observed the dye infiltration visually during infiltration, and then sectioned the column for detailed inspection. No evidence of preferential flow was found.

2.4 Theory

2.4.1 Water Flow

Water flow inside the column was described by the Richards' equation. The hydraulic properties were represented by the Mualem-van Genuchten functions [*van Genuchten,* 1980]: $S_e = [1 + (\alpha h)^n]^{(1/n-1)}$ and $K = K_s S_e^l [1 - (1 - S_e^{1/(1-1/n)})^{(1-1/n)}]^2$, where K and K_s are the unsaturated and saturated hydraulic conductivities (cm/min), respectively, h is the hydraulic head (cm-H_2O), S_e is the effective water saturation, calculated by $S_e = (\theta - \theta_r)/(\theta_s - \theta_r)$, where θ is the volumetric water content (cm^3/cm^3), θ_r is the residual water content (cm^3/cm^3), θ_s is the saturated water content (cm^3/cm^3), l is

a hydraulic conductivity parameter (−), α is inversely related to the air-entry value (cm^{-1}), and n is a pore size distribution parameter (−).

The parameters of the hydraulic functions were determined by inverse modeling using the Hydrus-1D code [*Simunek et al.,* 1998]. The model was simultaneously fitted to both, the measured water contents and water potentials, for optimizing the model parameters [*Simunek et al.,* 2002]. The five locations that were instrumented in the column were assumed to have identical hydraulic properties. The fitting was done for each experimental series separately, resulting in one set of hydraulic parameters for each of the 5 experimental series. The initial condition for each series was set to the measured potentials at the beginning of each experiment (−45 cm-H_2O). For the upper boundary, a specified water flow rate q was used:

$$J_w = q \qquad \text{at} \quad x = 0 \tag{2.1}$$

where $J_w = v\theta$ is the flow rate (cm/min), v is the pore velocity (cm/min), and q equals the experimental flow rates. The bottom boundary condition was set to a constant potential of −10 cm-H_2O for all times.

2.4.2 Colloid Release and Transport

We describe *in situ* colloid mobilization in unsaturated Hanford sediments by the advection-dispersion equation (ADE) coupled with a first-order kinetic colloid release:

$$\frac{\partial C}{\partial t} + \frac{\rho}{\theta}\frac{\partial S}{\partial t} = D\frac{\partial^2 C}{\partial x^2} - \frac{J_w}{\theta}\frac{\partial C}{\partial x} \tag{2.2}$$

$$\frac{\partial S}{\partial t} = -\beta S \tag{2.3}$$

where C is the colloid concentration in the aqueous phase (mg/cm^3), S is the colloid concentration on the sediments (mg/g), t is time (min), ρ is the bulk density (g/cm^3), D is the dispersion coefficient (cm^2/min), x is the coordinate parallel to the flow (cm), and β is the first-order colloid release rate coefficient (min^{-1}). For the upper boundary, a constant flux was used, i.e., $J_w C(0,t) = 0$, and for the lower boundary, a zero gradient was assumed $\theta D \partial C/\partial x = 0$. The initial conditions were $C(x,0) = 0$ and $S(x,0) = S_0$.

For colloid transport simulations, the initial colloid source S_0 for each breakthrough curve was obtained by integrating the experimental breakthrough curves to obtain the total amount of colloids eluted. We fitted each breakthrough curves separately, because the release rate coefficient likely depends on the flow rate or water content. Accordingly, the initial colloid source was obtained for each breakthrough curve separately. The governing equations were solved with the Hydrus-1D code [*Simunek et al.,* 1998]. The ADE was fitted to the colloid breakthrough data by adjusting the dispersion coefficient D and the colloid release coefficient β.

2.4.3 DLVO, Capillary, and Hydrodynamic Forces

To calculate the different forces acting on colloidal particles, we assume that the colloids are spherical. Although our natural colloids are not spherical, the equations presented in the following provide an approximation of the forces to be expected in unsaturated subsurface systems.

We used DLVO theory for a sphere-plate system to calculate colloid-sediment interaction energies. The electrostatic interaction energies were calculated as [*Gregory*, 1975]:

$$\Delta G_{\mathrm{el}} = 64\pi\epsilon R \left(\frac{kT}{ze}\right)^2 \Upsilon_1 \Upsilon_2 \exp(-\kappa h) \tag{2.4}$$

and the van der Waals interaction energies as [*Gregory*, 1981]:

$$\Delta G_{\mathrm{vdw}} = -\frac{AR}{6h}\left[1 - \frac{5.32h}{\lambda_0}\ln\left(1 + \frac{\lambda_0}{5.32h}\right)\right] \tag{2.5}$$

where ϵ is the permittivity of the liquid; R is the radius of the colloid; kT is the thermal energy; z is the ion valence; e is the electron charge; $\Upsilon_i = \tanh(ze\psi_{0,i}/(4kt))$ with $\psi_{0,i}$ being the surface potential of the colloids and the sediments, respectively; κ is the Debye-Hückel reciprocal length; h is the separation distance; A is the Hamaker constant, taken as 4.67×10^{-21} J (calculated according to *Hiemenz and Rajagopalan* [1997]); and λ_0 is a characteristic length of 100 nm. For our calculations, we used a colloid radius of 250 nm, which was the average of our experimental measurements. Because the colloids and the sediments had similar mineralogical composition, we assumed that the colloids and the sediments had the same ζ potentials. We set the surface potential equal the ζ potential. The ζ potential was obtained from the electrophoretic mobility using the von Smoluchowski equation. The Debye-Hückel length was estimated from effluent electric conductivity EC (dS/m), which we converted to ionic concentration c (mmol/L) by [*Marion and Babcock*, 1976]:

$$\log_{10} c = 0.955 + 1.039 \log_{10} EC \tag{2.6}$$

The DLVO forces were then obtained by the derivatives $F_{\mathrm{el}} = \mathrm{d}(\Delta G_{\mathrm{el}})/\mathrm{d}h$ and $F_{\mathrm{vdw}} = \mathrm{d}(\Delta G_{\mathrm{vdw}})/\mathrm{d}h$.

At small water contents, colloids are pinned to the sediment surface by capillary forces. A water bridge forms between colloids and the flat sediment surface (Figure 2.2a). As the water content increases, the water bridge expands, and will ultimately form a free water surface on the sediment (Figure 2.2b). Capillary forces will pin the colloid to the sediment until the water level increases above a certain level where the air-water curvature changes from concave to convex, at which point the capillary force pulls the colloid from the sediment surface (Figure 2.2c).

Before a free water level forms, the capillary force, F_{cap}, between a spherical colloid and a flat plane in contact with water forming a meniscus can be calculated by [*Chateau et al.*, 2002]:

$$F_{\mathrm{cap}} = 2\pi R\gamma \sin\phi \sin(\theta + \phi) + \Delta p \pi R^2 \sin^2\phi \tag{2.7}$$

where R is the radius of the colloid (m); γ is the water surface tension (N/m); ϕ is the filling angle (degree) between the center of the colloidal sphere and the water-colloid contact line; θ is the colloid water contact angle (degree) and was determined for our experimental system to be 25.9^o [*Chen and Flury*, 2005]; and Δp is the capillary pressure defined as the pressure jump across the air-water interface (see Figure 2.2a for an illustration of the symbols).

Applying the Young-Laplace equation (considering that there are two radii of cur-

vature) for the pressure jump in Equation 2.7, we obtain

$$F_{\text{cap}} = \pi R\gamma \left[2\sin\phi\sin(\theta+\phi) + \cos\theta(1+\cos\phi)^2 - \sin\phi\right] \tag{2.8}$$

At low water contents, where a capillary bridge pins the colloid to the solid surface, the solid surface itself is covered with a thin water film, whose thickness H is given as [*Hough and White,* 1980]:

$$H = \sqrt[3]{\frac{A}{6\pi\rho\Delta p}} \tag{2.9}$$

where ρ is the density of water. As the water content becomes larger, or the capillary pressure decreases, the filling angle ϕ increases. At a certain filling angle, a free water film forms on the sediment surface.

When a free water film on the sediment surfaces has been formed, Equation 2.8 cannot be used to calculate the capillary forces, because the boundary conditions for the Young-Laplace equation have changed. Equation 2.8 has boundary conditions given by two air-water-solid contact angles, one at the colloid and one at the sediment surface (Figure 2.2a). After a free water film forms, the boundary condition at the sediment surface changes to a free water surface and the contact angle becomes 0^o at infinity (Figure 2.2b). Then, the capillary force can be calculated as [*Zhang et al.,* 1996]:

$$F_{\text{cap}} = \pi R^3\rho g\left\{\frac{Hc + Rc[1+\cos(\pi-\phi)]}{Rc}\sin^2\phi + \frac{2}{(Rc)^2}\sin(\phi+\theta)\sin\phi\right\} \tag{2.10}$$

where H is the height of the water film, $c = \sqrt{(\Delta\rho g)/\gamma}$ is the capillary constant, $\Delta\rho$ is the difference between density of water and air, g is acceleration due to gravity. For

the calculation of Equation 2.10, we need to know the height of the water film H as related to the filling angle ϕ. This relationship was obtained by a numerical solution of the Young-Laplace equation as outlined in *Zhang et al.* [1996]. For the numerical integrations, we used the 4th-order Runge-Kutta method. Because the integration starts at infinity, an appropriate starting point has to be found. We followed the approach described in *Zhang et al.* [1996], which used modified Bessel functions to find the starting point.

The critical filling angle ϕ, at which a free water forms on the sediment surface was obtained by using the numerical solution of the Young-Laplace equation to determine the shape of the air-water interface. When the height H of the air-water interface exceeds the water film thickness given by Equation 2.9, we assumed that a free water film had formed.

The shear force, F_{s}, was calculated as [*Sharma et al.,* 1992]:

$$F_{\mathrm{s}} = 1.7(6\pi)\mu\frac{H}{2}V \tag{2.11}$$

where μ is water dynamic viscosity ($\mathrm{Ns/m^2}$), and V is the fluid velocity measured at the distance $H/2$ from the surface of the pore wall. If the colloid is completely covered with water, then $H/2 = R$. We approximated the fluid velocity V as the pore water velocity v. If the hydrodynamic release mechanism is rolling, the detachment criterion under water saturated conditions is given by the torque balance [*Sharma et al.,* 1992]:

$$1.399F_s\frac{H}{2} = (F_{\mathrm{vdw}} - F_{\mathrm{el}})\lambda \tag{2.12}$$

where $F_{\text{vdw}} - F_{\text{el}}$ is the attachment force and λ is the radius of the contact area between colloids and sediments, which can be taken as 0.6 nm according to *van Oss* [1994]. Both, the assumption of fluid velocity calculations and rolling detachment mechanism, are conservative in the sense that they lead to an overestimation of the shear force.

In the presence of a capillary force, we write the torque balance (Equation 2.12) as:

$$1.399 F_s \frac{H}{2} = (F_{\text{vdw}} - F_{\text{el}})\lambda + F_{\text{cap}} R \sin\phi \tag{2.13}$$

where $R \sin\phi$ is the radius of the contact area on which the capillary force acts. If the left-hand-side of Equation 2.13 is larger than the right-hand-side, the colloid will be removed from the solid surface.

2.5 Results and Discussion

2.5.1 Water Content and Matric Potential

The water characteristic and the unsaturated hydraulic conductivity functions are shown in Figure 2.3. The model parameters of the hydraulic functions are listed in Table 2.1. The predicted unsaturated hydraulic conductivity function agreed well with the experimentally measured flow rates (Figure 2.3). Each infiltration event was followed by a steady-state flow phase, where water contents and matric potentials remained constant and uniform along the column. The water contents reached similar

values for the same flow rate at steady state among the 5 series of column experiments (Table 2.2).

2.5.2 Colloid Mobilization

The colloid breakthrough curves were characterized by a steep breakthrough and a long eluation tail (Figure 2.4). The colloid breakthrough coincided with the arrival of the infiltration front at the bottom of the column. The long-lasting tails of the breakthrough curves indicate kinetic-controlled colloid release.

By integrating colloid breakthrough curves, we calculated the amounts of colloids released for each flushing step of the 5 series of column experiments (Table 2.2). The impact of flow rates on colloid release can only be compared for the cases for which the amounts of source colloids were similar. A larger initial flow rate led to greater peak colloid concentration; i.e., more colloids were mobilized at larger than at smaller flow rates (Figure 2.4, Table 2.2; comparing the initial amounts of colloids released among each series). This is consistent with findings of *Zhuang et al.* [2007]. When the flow rates were subsequently increased after an initial colloid mobilization (comparing the breakthrough curves within each series), an additional mobilization of colloids was observed. Interestingly, the amount of colloids mobilized increased with each subsequent flow rate increase, although the potential amount of source colloids decreases with each sequential infiltration event (Table 2.2), an observation corroborated by other investigators [*Saiers and Lenhart,* 2003*; Gao et al.,* 2004]. This increased colloid

mobilization is caused by the increased flow rate and/or water content. The diameters of released colloids were in the range from about 100 to 2000 nm, with an average of about 500 nm, without any clear trend as a function of flow rate.

The cumulative amount of colloids released for each of the 5 series of experiments was similar for Series 1, 2, 4, and 5, except for Series 3 (Table 2.2). This suggests that the cumulative amount of colloids mobilized was independent of the individual flow rates, but controlled by the largest flow rate used. Increased flow rates corresponded to greater water contents inside the column. We compared the cumulative amount of colloids released from each of the 5 series to the largest averaged column water content, and found a positive relationship between the amounts of colloids released and the water content (Figure 2.5). In general, the greater the water content, the more colloids were released.

The ADE could capture the front part of the breakthrough curves well; however, the tail part did not fit well (Figure 2.4). The model often predicted a less steep decline of the tail than was experimentally observed. The fitted colloid release rate coefficients generally increased with increasing water content or flow rate, but were fairly consistent among experimental series for a given flow rate (Table 2.2). This suggests that the release coefficient was independent of the amount of source colloids. As we will discuss below, we expect the release rate coefficient to increase with water content, because more colloids are being released when the water content increases due to repulsive capillary forces.

2.5.3 Elution Chemistry

In our experiments, elution chemistry varied due to the displacement of ions on sediment surfaces when deionized water infiltrated the column. For all 5 series of experiments, the electrical conductivity showed an initial peak when the infiltration front reached the column outlet, but then decreased with elapsed time (Figure 2.4). Hanford sediments are rich in Ca^{2+} and Mg^{2+}, and when water infiltrated Hanford sediments, Ca^{2+} and Mg^{2+} salts where dissolved and flushed out, resulting in initially increased electrical conductivity. The concentrations of dissolved organic carbon were highest for the first outflow peak, and the concentrations decreased thereafter. For Series 1, the concentration of dissolved organic carbon was 13.8 mg/L for the 0.018 cm/min flow rate, and the concentration dropped thereafter below the analytical quantification limit of our instrument. No dissolved organic carbon could be quantified for the successive peaks at the 0.036, 0.072, 0.144, and 0.288 cm/min flow rates. This suggests that the dissolved organic carbon was flushed out with the first elution peak, similar to what was observed by others [*Kaiser and Zech,* 1998*; Laegdsmand et al.,* 2005]. Colloid outflow concentrations, however, steadily increased with successive flow rate increases, even in absence of dissolved organic matter, suggesting that dissolved organic matter did not play a major role in colloid mobilization in these successive release events.

We used the extremes of the measured electrical conductivities and the electrophoretic mobilities to calculate the DLVO interaction energies between colloids and sediments.

The results showed that there were differences in the interaction energies among the different chemical compositions of the effluent (repulsive energy barriers changed from 210 to 430 kT) . However, these energies were all higher than thermal energies, and no secondary minimum was present in any case. It is therefore unlikely that differences in effluent chemistry significantly affected colloid mobilization. Furthermore, the electrophoretic mobility of the eluted colloids showed no obvious trend as a function of elution volume (Figure 2.4), suggesting that there was no ζ-potential related fractionation of colloids during the infiltration events.

Figure 2.6 shows a comparison between colloid outflow curves for deionized water and a 0.5 M $CaCl_2$ solution. The outflow was normalized by the column pore volume after steady-state flow had been achieved, so that the different flow rates can be compared. At high ionic strength (0.5 M $CaCl_2$), electrostatic repulsion of colloids from the sediment surfaces was suppressed, and the DLVO calculations (no matter whether we assumed a 1:1 or 2:2 electrolyte solution) show that the colloid-sediment interaction energies were attractive; no repulsive energy barrier existed. We therefore expected that no colloids should be mobilized when we infiltrated a 0.5 M $CaCl_2$ solution. However, we observed colloid release and mobilization, even at the smallest flow rate used in our experiments, although the amount of colloids mobilized was considerably less than in the case of deionized water (Figure 2.6). Compared to deionized water, the $CaCl_2$ solution also resulted in a steeper elution tail of the colloid release curves.

2.5.4 DLVO, Capillary, and Hydrodynamic Forces

Figure 2.7 shows the different forces acting on a spherical colloid as a function of filling angle ϕ as calculated by Equations 5.29, 2.5, 2.8, 2.10, and 2.11. For these calculations, we used a colloid diameter of 500 nm and an air-water-colloid contact angle of 25.9^o, according to the measured properties of the collloids in our experimental system. The conclusions drawn from our calculations, however, are valid for a large range of colloid radii and contact angles. The figure also shows the water film thickness as calculated by Equation 2.9 and by the numerical solution of the Young-Laplace equation. We use negative values to denote attractive forces between colloids and sediments, and positive values to denote repulsive forces. The different forces are discussed in the following.

The DLVO calculations showed that during infiltration of deionized water (we estimated the ionic strength from Equation 2.6), the colloid-sediment interactions were unfavorable for attachment, i.e., there was a large energy barrier ($>$200 kT) for attachment. There was no secondary minimum in the DLVO interaction profile. The repulsive electrostatic forces between colloids and sediments dominated the attractive van der Waals forces at separation distances $>$ 1 nm. The maximum repulsive DLVO force ($F_{\rm el} - F_{\rm vdw}$) was in the order of 10^{-9} N, which occurred at a separation distance of 2 nm. When the colloid was in contact with the sediment surface, i.e., at a separation distance of 0.3 nm, the DLVO force ($F_{\rm el} - F_{\rm vdw}$) was attractive with a value of -1.7×10^{-9} N. This attractive DLVO force is shown in Figure 2.7 as horizontal line, because

the DLVO force does not depend on the filling angle. If the separation distances are larger than 0.3 nm, then the attractive DLVO force would decrease considerably.

The attractive capillary force had a maximum at zero degree filling angle of about -2×10^{-7} N (Figure 2.7). As the filling angle increased, the capillary force initially decreased according to Equation 2.8. When a free water film formed (at a filling angle of $\phi = 83^o$), the capillary forces were calculated with Equation 2.10. As the water film thickness increased, the capillary force continuously decreased until the water film showed no curvature anymore around the colloid, and the capillary force vanished. For our system that occurred at a filling angle of $\phi = 154.1^o$, corresponding to a water film thickness of 475 nm (Figure 2.7, insert). When the water film increased beyond that filling angle, the capillary force became positive, i.e., repulsive, and pulled the colloid from the sediment surface (Figures 2.2c and 2.7). The repulsive force passed through a maximum ($F_{\text{cap,max}} = 5.69 \times 10^{-9}$ N) and decreased again until it vanished. However, if the water film thickness continuously increases, the colloid will either start to float (if repulsive forces are larger than attractive forces) or the water film will detach from the colloid (if repulsive forces are smaller than attractive forces). In our specific case, shown in Figure 2.7, the repulsive capillary force equaled the attractive DLVO force when the filling angle of $\phi = 156^o$, corresponding to a water film thickness of 484 nm. If the water film expanded beyond 484 nm, the colloid would be lifted off the sediment surface.

The maximum repulsive capillary force shown in Figure 2.7 can also be obtained

by a closed-form formula used to calculate the detachment force of a particle from the air-water interface [*Scheludko et al.,* 1976*; Preuss and Butt,* 1998a*; Pitois and Chateau,* 2002]:

$$F_{\text{det}} = 2\pi R\gamma \sin^2\left(\frac{\theta}{2}\right) \tag{2.14}$$

Applying Equation 2.14 to our system yields $F_{\text{det}} = 5.74 \times 10^{-9}$ N, which is similar to $F_{\text{cap,max}} = 5.69 \times 10^{-9}$ N obtained by the numerical solution of Equation 2.10 (Figure 2.7, insert).

The shear forces were in the order of 10^{-13} to 10^{-12} N. The shear force calculations using Equation 2.11 may be subject to errors because our particles are not spherical, nor do we know the fluid velocities at the colloid surfaces accurately. But it is expected that our calculations overestimate the shear forces, so that our estimations are conservative. Compared to the DLVO and capillary forces, the shear forces were negligible (Figure 2.7). Indeed, for laminar flow, it is often found that hydrodynamic shear forces are negligible compared to electrostatic forces [*Ryan and Gschwend,* 1994].

These considerations show that, depending on the water content, the attractive as well as repulsive capillary forces were larger than the DLVO and shear forces. Indeed the torque balance (Equation 2.13) confirms that the shear force had a negligible effect on colloid detachment, and that the major detachment force was due to the capillary force. The dominance of capillary forces on colloid attachment has also been pointed out for colloids subject to film flow [*Veerapaneni et al.,* 2000]. Here we also show that there is a repulsive capillary force that can detach colloids from sediment surfaces.

Colloid release occurred in regions where the water films exceeded a critical thickness, i.e., in regions where capillary forces between colloids and sediment surfaces became repulsive.

For the high ionic strength electrolyte solutions, the DLVO calculations indicate attractive forces at all separation distances. The maximal attractive force at the contact distance of 0.3 nm was $F_{\mathrm{el}} - F_{\mathrm{vdw}} = -2.1 \times 10^{-9}$ N. This force is considerably smaller than the repulsive capillary force, so that, like in the case of deionized water, colloids can be lifted off the sediment surface by a raising water film. The strong capillary forces and colloid attachment to the air-water interface also explain the observation from *Zhuang et al.* [2007] that a drainage front can cause a colloid peak at a column outflow.

2.5.5 Conceptual Model of Colloid Release

Our force considerations, and the associated colloid release mechanism, can be combined with the conceptual model of unsaturated water flow as described by Kung and coworkers [*Gish et al.,* 2004*; Kung et al.,* 2005] to develop a conceptual model for colloid release under unsaturated flow. Kung and co-workers suggested that, as the flow rate in a porous medium increases, more and more pores become filled with water and contribute to flow; a larger and larger fraction of the porous medium contributes to water flow. This concept can be well applied to colloid release. Under initially dry conditions, colloids are pinned to the sediment surfaces by strong attractive capillary

forces. When the flow rates, and consequently the water contents, increase, water film thicknesses increase and more and more pores become water filled. Consequently, capillary forces become less dominant, until at a critical water content, the capillary forces vanish and even become repulsive, leading to colloid release. This successive pore filling will therefore also lead to successive release of colloids. This interpretation is corroborated by a recent report by *Levin et al.* [2006], who also suggested that colloid mobilization from an undisturbed soil core was dominated by the number of pores contributing to flow rather than by shear forces.

Although in the previous calculations we only considered a single particle size and contact, the major conclusion about the dominance of the repulsive capillary forces are valid for a range of particle sizes and contact angles. The theory presented can be used to calculate the forces as a function of colloid radius and contact angle, and it can be shown, for instance, that particle with contact angle larger than 15^o (for a colloid diameter of 500 nm) can be lifted off by capillary forces.

2.6 Tables and Figures

Table 2.1: Hydraulic properties of Hanford sediment.

Series	Saturated hydraulic conductivity K_s (cm/min)	α (cm^{-1})	n (−)	l (−)
Series 1	1.5 ± 0.1	0.086 ± 0.001	4.5 ± 0.3	2.5 ± 0.2
Series 2	1.9 ± 0.2	0.084 ± 0.001	5.7 ± 0.3	2.7 ± 0.2
Series 3	1.3 ± 0.3	0.082 ± 0.002	5.8 ± 0.4	2.1 ±0.2
Series 4	1.8 ± 0.3	0.086 ± 0.001	5.2 ± 0.5	3.0 ± 0.4
Series 5	1.9 ± 0.5	0.087 ± 0.002	5.9 ± 0.8	2.8 ± 0.3

α: inverse air-entry or bubbling pressure; n: pore size distribution parameter; l: conductivity parameter;

Saturated water content (θ_s =0.393 ± 0.003 cm^3/cm^3) and residual water content (θ_r=0.092 ± 0.003 cm^3/cm^3) were obtained from hanging water column experiments;

Errors denote standard deviations.

Table 2.2: Flow rate, water content, amounts of colloids released, and colloid release rate coefficient.

Flow rate[†] (cm/min)	Volumetric Water content[†,‡] (cm^3/cm^3)	Pore water velocity (cm/min)	Amount of colloids released[†] (mg)	Cumulative amount of colloids released[†] (mg)	Colloid release rate coefficient[§] β (min^{-1})
			Series 1		
0.018	0.21 ± 0.01	0.086	2.33 ± 1.0	2.33 ± 1.0	0.009 ± 0.007
0.036	0.24 ± 0.01	0.150	4.70 ± 0.6	7.00 ± 0.4	0.007 ± 0.010
0.072	0.27 ± 0.01	0.267	4.40 ± 1.3	11.4 ± 1.0	0.012 ± 0.007
0.144	0.28 ± 0.01	0.514	6.97 ± 2.3	18.4 ± 3.2	0.029 ± 0.002
0.288	0.32 ± 0.02	0.900	14.3 ± 3.4	32.7 ± 6.7	0.083 ± 0.010
			Series 2		
0.036	0.21 ± 0.01	0.171	4.24 ± 1.0	4.24 ± 1.0	0.009 ± 0.001
0.072	0.23 ± 0.02	0.313	6.19 ± 1.7	10.4 ± 2.7	0.015 ± 0.001
0.144	0.27 ± 0.01	0.533	11.1 ± 0.5	21.6 ± 3.2	0.023 ± 0.001
0.288	0.29 ± 0.03	0.993	15.1 ± 1.5	36.7 ± 4.7	0.072 ± 0.001
			Series 3		
0.072	0.27 ± 0.01	0.267	8.64 ± 0.1	8.64 ± 0.1	0.015 ± 0.006
0.144	0.29 ± 0.01	0.497	16.6 ± 0.3	25.2 ± 0.3	0.026 ± 0.001
0.288	0.32 ± 0.01	0.900	20.1 ± 0.4	45.3 ± 0.7	0.076 ± 0.003
			Series 4		
0.144	0.27 ± 0.01	0.533	14.9 ± 0.8	14.9 ± 0.8	0.039 ± 0.010
0.288	0.30 ± 0.01	0.960	18.5 ± 0.8	33.5 ± 1.6	0.088 ± 0.011
			Series 5		
0.288	0.30 ± 0.01	0.960	33.1 ± 2.7	33.1 ± 2.7	0.074 ± 0.014

[†] Measured experimentally.

[‡] Converted from overall gravimetric water content measured with the load-cell.

[§] Fitted with advection-dispersion model.

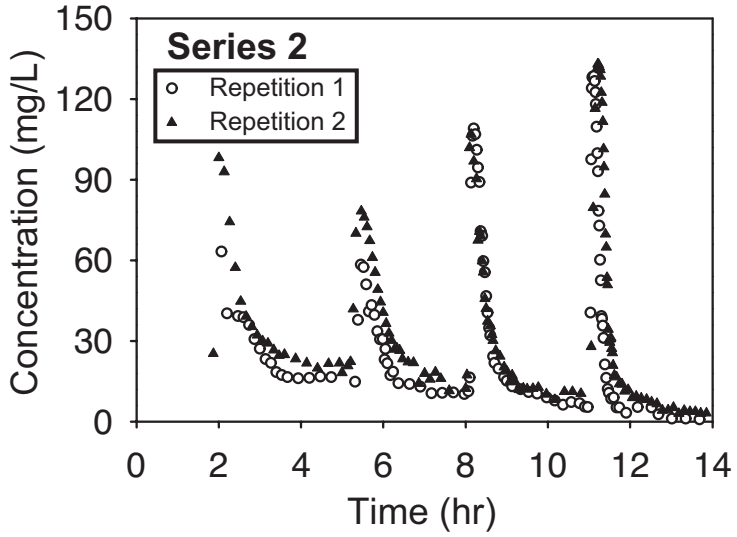

Figure 2.1: Reproducibility of colloid release breakthrough curves for the series 2 experiments with an initial flow rate of 0.036 cm/min.

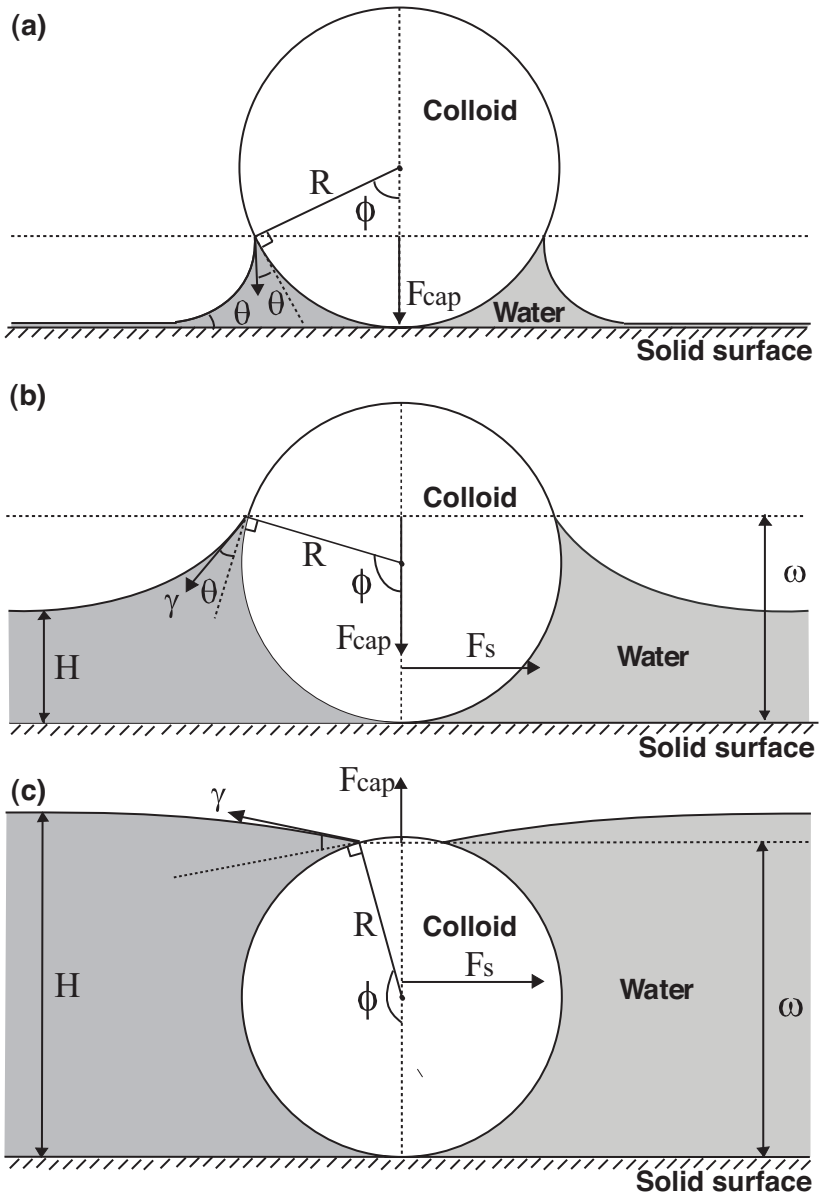

Figure 2.2: Schematic of a spherical colloid in contact with a flat sediment surface. (a) Small water content, (b) intermediate water content, and (c) large water content. R: radius of colloid, θ: contact angle, ϕ: filling angle, γ: surface tension of water, F_{cap}: capillary force, F_s: shear force, H: height of water film, ω: height of water-colloid contact line.

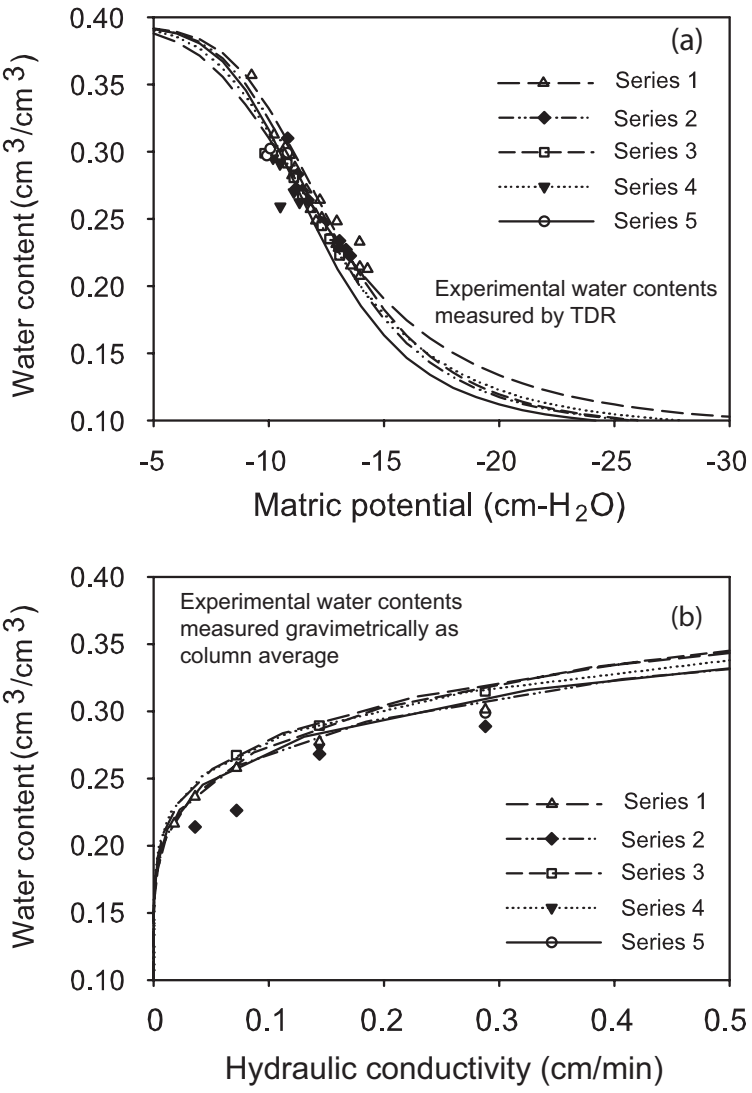

Figure 2.3: Moisture characteristic (a) and hydraulic conductivity (b) functions. Symbols are measured values from steady-state flow phases and lines are Mualem-van Genuchten functions (with parameters given in Table 2.1).

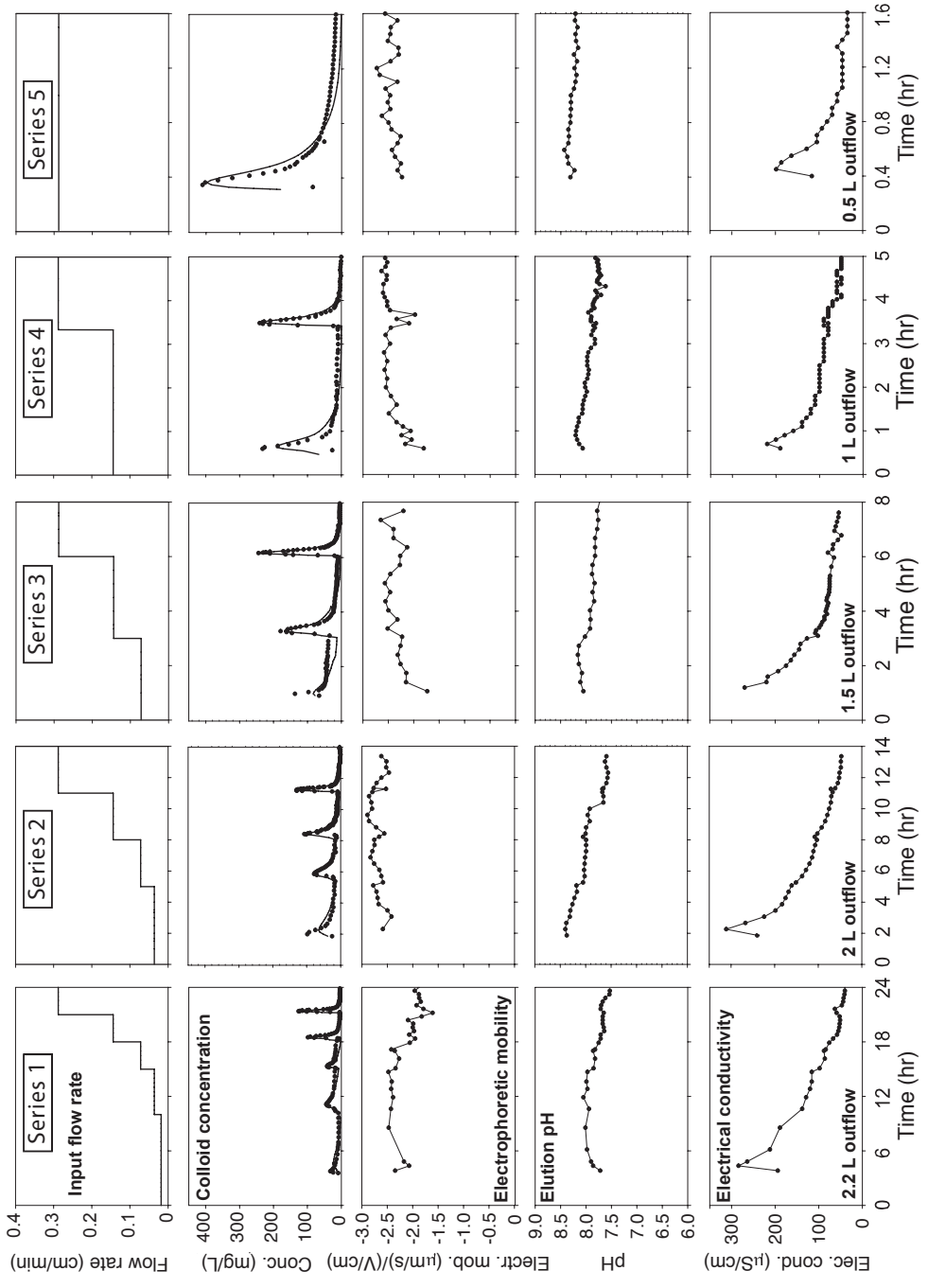

Figure 2.4: Colloid release breakthrough curves for the 5 series of experiments with initial flow rates of 0.018, 0.036, 0.072, 0.144 and 0.288 cm/min, respectively. For the colloid breakthrough curves, symbols are measured colloid concentrations and lines are model simulations.

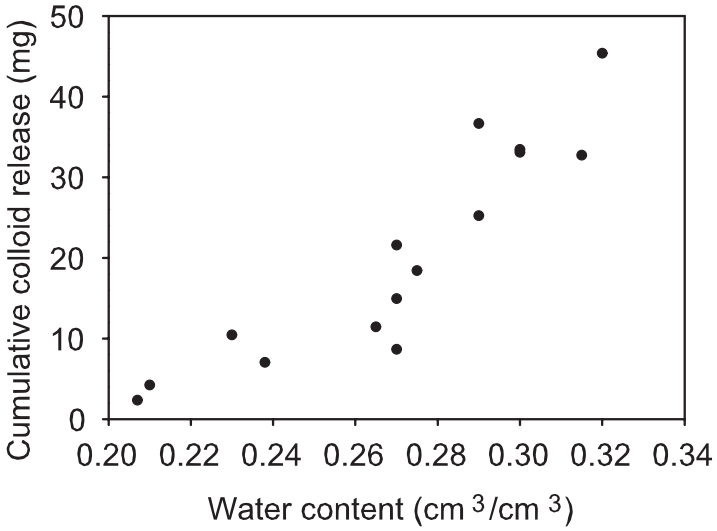

Figure 2.5: Cumulative amounts of colloids released as a function of column water content.

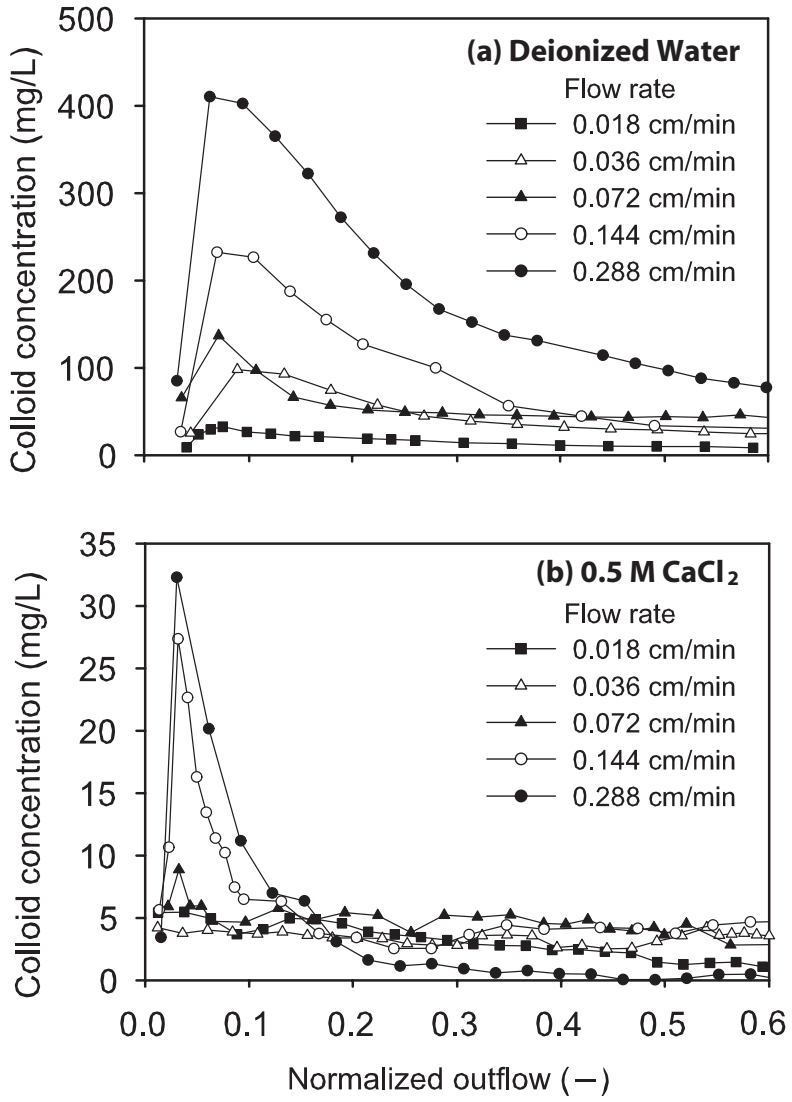

Figure 2.6: Colloid release breakthrough curves for infiltration of (a) deionized water and (b) 0.5 M $CaCl_2$ solution. Normalized outflow is defined as outflow volume divided by the volume of water inside the column after steady-state flow was achieved.

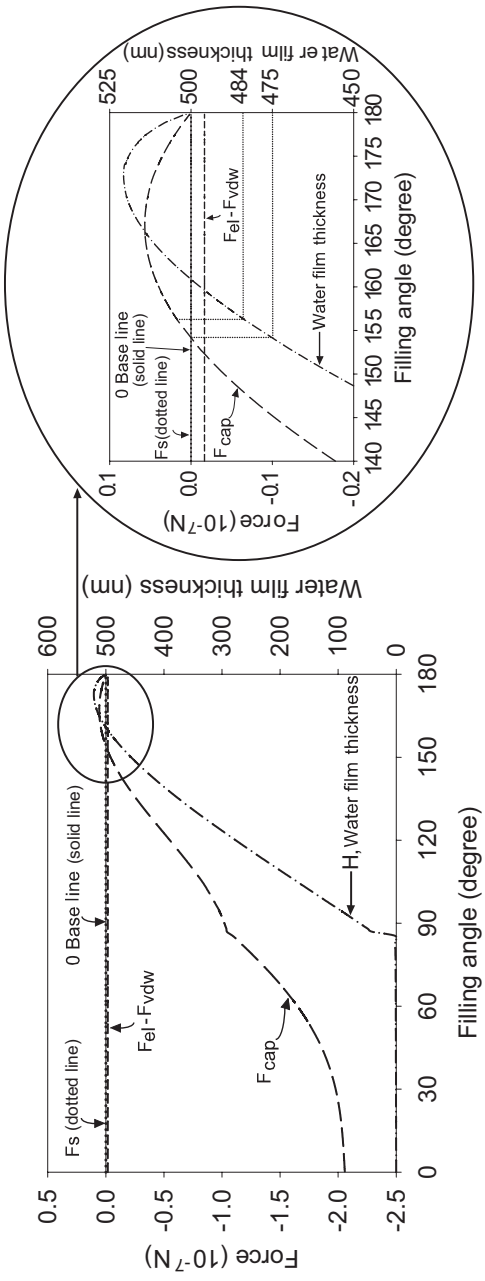

Figure 2.7: Forces acting on a spherical colloid (500-nm diameter, 25.9^o contact angle) in contact with a sediment surface and water film thickness H as a function of filling angle ϕ: F_{cap}: capillary force, F_{vdw}: van der Waals force, F_{el}: electrostatic force, F_{s}: shear force. DLVO forces are for an ionic concentration of 2.8 mM of a 1:1 electrolyte solution.

Chapter 3

Comparison of Different Methods to Measure Contact Angles of Subsurface Colloids

3.1 Abstract

We compared five different methods, static sessile drop, dynamic sessile drop, Wilhelmy plate, thin-layer wicking, and column wicking, to determine the contact angle of colloids typical subsurface environments. The colloids (smectite, kaolinite, illite, goethite, hematite) were chosen to represent 1:1 and 2:1 layered aluminosilicate clays and sesquioxides, and were either obtained in pure form from commercial suppliers or synthesized in our laboratory. Colloids were deposited as thin films on glass slides,

A modified version of this chapter has been submitted for publication: Shang, J., M. Flury, J. B. Harsh, and R. L. Zollars, Comparison of Different Methods to Measure Contact Angles, the Journal of Colloid and Interface Science.

and then used for contact angle measurements using three different test liquids (water, formamide, diiodomethane). We then determined surface thermodynamic properties from contact angles according to the van Oss-Chaudhury-Good thermodynamic approach. The colloidal films could be categorized into three types: (1) films without pores and with polar-liquid interactions (smectite), (2) films with pores and with polar-liquid interactions (kaolinite, illite, goethite), and (3) films without pores and no polar-liquid interactions (hematite). The static and dynamic sessile drop methods yielded the most consistent contact angles. For porous films, the contact angles decreased with time, and we consider the initial contact angle to be the most accurate. The differences in contact angles among the different methods were large and varied considerably: the most consistent contact angles were obtained for kaolinite with water, and illite with diiodomethane (contact angles were within 3^o); but mostly the differences ranged from 10^o to 40^o among the different methods. The thin-layer and column wicking methods were the least consistent methods.

3.2 Introduction

The most common methods to determine contact angles are the sessile or pendant drop and the Wilhelmy plate methods. These methods are based on angle measurements using a goniometer or based on force measurements using a tensiometer. For porous materials, the wicking or capillary rise method is often used [*Chibowski and Perea-Carpio,* 2002]. For spherical particles, methods have been developed to determine con-

tact angles based on force measurements [*Zhang et al.,* 1996*; Preuss and Butt,* 1998c], confocal microscopy [*Mohammadi and Amirfazli,* 2004], and film trapping [*Hadjiiski et al.,* 1996]. The contact angle of colloidal particles, however, is difficult to measure because the small particle size (<2 μm in diameter) poses considerable challenges with existing contact angle measurement methods.

Different methods have been described in the literature to determine contact angles of colloids. The sessile drop method can be used to measure static and dynamic contact angles of colloids. As the sessile drop method requires a flat surface upon which a liquid drop can be placed, colloids are often deposited as a flat film onto a microscope slide or filter paper [*van Oss and Gillman,* 1972a*; van Oss and Gillman,* 1972b*; van Oss,* 2006*; Wu,* 2001*; Giese and van Oss,* 2002]. The smoother the film surface, the better and more accurate is the contact angle measurement. Smooth films have been made with synthetic colloids, such as Latex microspheres [*Wan and Wilson,* 1994], mineral colloids, such as smectites and hematite [*Wu,* 2001*; Costanzo et al.,* 1995], bacteria, such as *Pseudomonas cepacia 3N3A*, *Arthrobacter sp.*, *Eschericia coli* [*Wan et al.,* 1994*; Abu-Lail and Camesano,* 2006], and viruses, such as hepatitis A [*Kukavica-Ibrulj et al.,* 2004]. Spherical, monodisperse particles, like microspheres are well suited for the sessile drop method, because uniform films can be produced [*Wan and Wilson,* 1994]. Among subsurface colloids, smectites are particularly suitable for the sessile drop method, because these clays are swelling, and form a water impermeable surface [*Wu,* 2001]. If the colloidal film is porous, then the liquid drop will penetrate into

the film, and as a consequence the contact angle changes with time [*Wu,* 2001*; van Oss et al.,* 1992]. Kaolinite, for instance, forms a porous film, in which water readily infiltrates [*Wu,* 2001].

The sessile drop method has also been used to determine contact angles for soil material. Bachmann and coworkers [*Bachmann et al.,* 2000b*; Bachmann et al.,* 2000a*; Bachmann et al.,* 2003] used double-sided adhesive tape to mount a thin, one-grain layer of powdered or sieved soil materials on a glass microscope slide. They determined static contact angles for different soil types, varying in texture, mineral and organic matter composition, and geopraphic origin [*Bachmann et al.,* 2003].

The Wilhelmy plate method is commonly used for materials with a well-defined wetting length, so that the contact angle can be calculated from the measured capillary force. The Wilhelmy plate method has been used to determine contact angles of gold colloids [*Abe et al.,* 2000] and soil material [*Bachmann et al.,* 2003*; Woche et al.,* 2005], where the particles were deposited or glued to a flat plate, which was then used as the Wilhelmy plate.

For powdered or porous materials, contact angles are often determined with the Washburn method [*van Oss,* 2006*; Washburn,* 1921]. In this method, the speed of the capillary rise into the porous medium is measured, from which the contact angle can be determined. For successful use of the Washburn method, the geometry of the porous material should remain constant during the capillary rise. However, subsurface colloids, such as clay minerals, tend to cluster or shrink and swell, causing the pore

structure to change [*Costanzo et al.,* 1995].

To prevent this problem, colloidal particles can be deposited on a flat surface, forming a rigid thin layer of porous material, which is then used for the Washburn method [*van Oss et al.,* 1992*; Giese et al.,* 1991]. This method is known as thin-layer wicking [*van Oss et al.,* 1992]. It has been used for a variety of particles, such as illite [*van Oss et al.,* 1992], kaolinite [*Wu,* 2001], attapulgite [*Wu,* 2001], talc [*van Oss et al.,* 1992*; Wu et al.,* 1996], hydrotalcite [*Li et al.,* 1994], hematite [*Costanzo et al.,* 1995], dolomite [*Wu et al.,* 1996], calcite [*Wu et al.,* 1996], basalt [*Teixeira et al.,* 1998], limestone [*Teixeira et al.,* 1998], silica [*Chibowski and Holysz,* 1992*; Chibowski and González-Caballero,* 1993], and feldspar [*Karagúzel et al.,* 2005].

More recently, contact angle methods based on film and gel trapping [*Hadjiiski et al.,* 1996*; Paunov,* 2003], atomic force microscopy [*Preuss and Butt,* 1998c*; Preuss and Butt,* 1998b*; Preuss and Butt,* 1999], and scanning confocal microscopy [*Mohammadi and Amirfazli,* 2004] have been developed. These methods are particularly useful for spherical particles in the micrometer size range, but less suitable for subsurface colloids, which have irregular shapes, i.e., flaky, platy, or polyhedrical.

The determination of contact angles for subsurface colloids remains challenging, and no ideal method has yet been described. It is likely that different methods are optimal for different types of colloids. The objective of this paper was, therefore, to compare different methods to determine contact angles of subsurface colloids. We used the sessile drop, Wilhelmy plate, capillary rise (column wicking), and thin-layer wicking

methods to determine contact angles of five major types of subsurface colloids (swelling and non-swelling aluminosilicate clays, and (hydr)oxides). We discuss advantages and disadvantages of the different methods, and make recommendations on the optimal methods for specific subsurface colloids.

3.3 Materials and Methods

3.3.1 Subsurface Colloids

We used five typical subsurface colloids: three aluminosilicate clays and two (hydr)oxides (Table 3.1). Arizona smectite (SAz1) and Georgia kaolinite (KGa1b) were obtained from the Clay Minerals Repository (University of Missouri), and illite (No. 36, Morris, Illinois) was obtained from Ward's Natural Science (Rochester, NY). All the clays (smectite, kaolinite, illite), as received from the suppliers, were fractionated by gravity sedimentation to obtain particles smaller than 2 μm in diameter. Hematite and goethite were synthesized in our laboratory following Schwertmann and Cornell [*Schwertmann and Cornell,* 1991].

The fractionated clay minerals were treated with H_2O_2 to remove organic matter and the citrate-dithionite method was used to remove iron oxides. Then, to prevent Al^{3+} precipitation on the clay surfaces, the pH of the clay suspensions was lowered to about 4 by titration with 0.1 M HCl. The suspensions were shaken for three hours, and the supernatant was decanted after centrifugation. This procedure was repeated three

times. Finally, the clay suspensions were washed with deionized water. Deionized water was added, equilibrated for three hours, and decanted after centrifugation. This washing procedure was repeated until the suspensions reached pH 6. Finally, the clay minerals were made homoionic and Ca-saturated by washing with 0.5 M $CaCl_2$, and dialyzed with deionized water until free from chloride [*Chorom and Rengasamy,* 1995*; Jerez et al.,* 2006]. All colloids were stored in concentrated suspensions at room temperature until use.

Average hydrodynamic particle size and electrophoretic mobility were measured by dynamic light scattering using a Zetasizer 3000HAS (Malvern Instruments Ltd., Malvern, UK). The particle shapes were determined by scanning and transmission electron microscopy (Hitachi S520 SEM, JEOL 1200EX TEM). Selected properties of the colloids are shown in Table 3.1.

3.3.2 Test Liquids

Polar and apolar liquids were used for the contact angle measurements (Table 3.2): double deionized water (electrical conductivity 0.58 μS/cm, E-pure, Barnstead), formamide (99.5% purity, from Acros Organics, Morris Plains, NJ), diiodomethane (99+% purity, from Acros Organics, Morris Plains, NJ), and hexane (100% purity, J.T. Baker, Phillipsburg, NJ). Hexane was used as the low energy liquid with contact angle of 0 degree, and was used to obtain the capillary constant for the wicking methods. The other liquids were used to calculate surface energies based on the van Oss-Chaudhury-

Good thermodynamic approach, for which at least two polar and one apolar liquids are recommended [*van Oss,* 2006].

3.3.3 Sessile Drop Method (Static and Dynamic)

For the sessile drop method, a microscope cover glass slide (2.2 cm×2.2 cm), cleaned with acetone and deionized water, was coated with colloids following the procedure described by Wu [*Wu,* 2001]. For the coating, concentrated colloid stock suspensions were first diluted with deionized water to a concentration of about 1–2% wt/vol, and stirred with a magnetic stir bar for several hours. Then, 1.5 mL suspension was placed on the microscope slide, evaporated for two days under laminar air flow, and finally dried in an oven at 105° for 12 hours. Glass slides were kept horizontal during the drying process.

The contact angles were determined using a goniometer (Drop Shape Analysis System, DSA100, Krüss GmbH, Hamburg, Germany), equipped with an environmental chamber and a micro-syringe steel needle of 0.5-mm diameter. The environmental chamber helped to minimize evaporation. For static contact angle measurements, the syringe needle was positioned 0.2 mm from the surface of the colloidal film, and a drop of the test liquid (2 μL) was dispensed at a rate 1.75 μL/s. After dispensing, the drop shape was monitored with a digital camera for 20 s, and contact angle, drop diameter, and volume were recorded. For dynamic contact angle measurements, the drop volume was continuously increased and then decreased as contact angles were

recorded. We used a liquid dispensation rate of 5 μL/min to increase the drop volume from 0 to 5 μL (advancing contact angle), and then reversed the flow at the same rate to decrease the drop volume again (receding contact angle).

3.3.4 Wilhelmy Plate Method

For the Wilhelmy plate method, we coated a cleaned microscope cover glass on both sides with colloids. A 1.5-mL drop of 3% wt/vol colloid suspension was placed on the glass slides and evaporated for 12 hours under laminar air flow. Then, the slide was turned over and the other side was coated with the same procedure. The slide was dried for two days under laminar flow and then heated in an oven at 105° for 12 hours. With this procedure, the slide was completely covered with a thin film of colloids.

The contact angles were determined using a tensiometer (K100, Krüss GmbH, Hamburg, Germany). The wetted length of the coated slides was measured by a digital micrometer caliper. The slide was suspended from the electronic tensiometer balance and moved in and out of the test liquids at a speed of 1 mm/min. The force acting on the balance was continuously measured. Advancing and receding contact angles were obtained from immersion and emersion, respectively. The contact angle was calculated according to $\cos\theta = (F - F_{\mathrm{b}})/(P\gamma_{\mathrm{L}})$, where F is the measured vertical force (N), F_{b} is the buoyancy force (N), P is the wetted length (m), and γ_{L} is the surface tension of the test liquid (J/m^2).

3.3.5 Thin-Layer Wicking Method

For the thin-layer wicking method, we prepared thin films of colloids on a glass slide (2.4 cm × 4 cm), using the same procedure as described for the Wilhelmy plate method. Because the slide was larger than the ones used for the Wilhelmy plate method, we used a 3 mL drop of colloid suspension.

The capillary constant was determined with hexane as test fluid. Before the hexane measurements, the coated slides were equilibrated in a glass container with saturated hexane vapor for one hour to equalize the spreading pressure [*Wu,* 2001]. For the wicking, the slides were vertically dipped to a depth of 5 mm into the test liquids contained in a sealed cylindrical glass container to prevent evaporation. As soon as the slide was immersed into the liquid, the wicking height was recorded with a video camera (iSight, Apple, Inc.). Recording was stopped when the wicking height was 2 cm. The Washburn equation was used to calculate contact angles [*Washburn,* 1921]:

$$x^2 = \frac{R_{\text{eff}}\gamma_{\text{L}}\cos\theta}{2\eta}t \tag{3.1}$$

where x is the wicking distance (m) in the porous layer, t is time (s), R_{eff} is the effective pore radius (m) of the interparticle capillaries in the porous layer, γ_{L} is the surface tension of test liquid (J/m^2), and η is the liquid viscosity (N s m^{-2}).

3.3.6 Column Wicking Method

For the column wicking method, colloid suspensions were dried, ground into powders, and passed through sieves to obtain aggregates between 106 and 250 μm in diameter.

Spherical glass beads (diameter of 120 μm) were used as standards. The sample holder was an aluminum tube with an inner diameter of 12 mm (Krüss GmbH, Hamburg, Germany). The bottom of the sample holder was punctured to allow liquid to enter. A 30-μm mesh membrane was placed into the sample holder to prevent the sample powder from falling out. Two grams of dry powder were placed into the sample holder with manual tapping (several times) to obtain uniform packing of the aggregates. After packing, the holder was placed onto the electronic balance of the tensiometer. The weight gain of the sample holder after contact with test liquids was recorded. The modified Washburn equation was used to calculate contact angles [*Siebold et al.,* 1997]: $w^2 = ct\rho^2\gamma_{\mathrm{L}}\cos\theta/\eta$, where w is the weight increase of the column (kg), ρ is the liquid density (kg m^{-3}), and c is the capillary constant (m^5). The capillary constant c was determined using hexane as the test fluid.

3.3.7 Surface Tension Calculations

The measured contact angles were used to calculate surface tension components of the colloids. The surface tension γ_{i} of a material i can be divided into a Lifshitz-van der Waals and a Lewis acid-base component [*van Oss,* 2006*; van Oss et al.,* 1988]:

$$\gamma_i = \gamma_i^{\mathrm{LW}} + \gamma_i^{\mathrm{AB}} \tag{3.2}$$

$$\gamma_i^{\mathrm{AB}} = 2\sqrt{\gamma_i^+\gamma_i^-} \tag{3.3}$$

where γ_i^{LW} is the Lifshitz-van der Waals (apolar) component (J/m^2) and γ_i^{AB} is the Lewis acid-base (polar) component (J/m^2), which includes γ_i^+, the electron-acceptor

parameter (J/m^2) and γ_i^-, the electron-donor parameter (J/m^2). The relationship between the liquid-solid contact angle and the surface tension components is given by the van Oss-Chaudhury-Good approach [*van Oss*, 2006*; van Oss et al.*, 1988]:

$$\gamma_L (1 + \cos\theta) = 2\left(\sqrt{\gamma_S^{LW}\gamma_L^{LW}} + \sqrt{\gamma_S^+\gamma_L^-} + \sqrt{\gamma_S^-\gamma_L^+}\right) \tag{3.4}$$

where subscript "S" denotes the solid and "L" denotes the test liquid. The known surface-tensions of the liquids provide the values of γ_L^{LW}, γ_L^+ and γ_L^-. The unknown values of γ_S^{LW}, γ_S^+ and γ_S^- are determined by contact angle measurement with three or more different liquids, of which at least two are polar.

3.4 Results and Discussion

3.4.1 Colloid Films

The thin colloid films prepared by deposition of colloids on the glass slides are shown in Figure 3.1. The electron micrographs show that the different colloid films had different surface roughness. Smectite, kaolinite, illite, and goethite films all had considerable roughness, whereas the hematite surface appeared smooth at the scale of the micrographs. The smooth surface obtained for hematite was because of the small and spherical particle size of the hematite colloids (Table 3.1). Kaolinite, illite, and goethite surfaces show also the presence of pores.

3.4.2 Sessile Drop Method (Static)

Figure 3.2 shows the contact angles, drop diameters, and drop volumes determined as a function of time after the liquid drop was placed onto the colloid film. Only the data for smectite, kaolinite, and hematite are shown; illite and goethite patterns were similar to kaolinite, and are therefore not shown. Table 3.3 shows contact angles at three time intervals and the corresponding surface tension components as calculated with Equation 3.4 for all colloids.

For smectite, contact angles of water and formamide decreased and drop diameters increased with time, whereas the drop volumes remained constant (Figure 3.2). Contact angles, drop diameters, and drop volumes of diiodomethane remained constant. The constant drop volume indicates that there was no penetration of liquid into the colloid film. Smectite swells in contact with water and in the process seals the film surface [*Wu,* 2001]. The decreasing contact angles of the polar liquids, water and formamide, may be explained by hydration [*McBride,* 1989] and polar (acid-base) interactions [*van Oss,* 1994]. Indeed, the acid-base surface tension component γ_S^{AB} and electron-donor parameter γ_S^- increased with time (Table 3.3). Our values of γ_S^- were smaller than the value of 45.9 mJ/m^2 reported by Wu [*Wu,* 2001]. This difference is likely caused by the different pretreatment and dryness of the smectite; Wu [*Wu,* 2001] did not saturate the clays with one specific cation and air-dried the clay. For the apolar diiodomethane, there were no strong surface interactions between the apolar liquid and the solid, therefore contact angles, drop diameters, and volumes were stable.

The value of the apolar surface tension component γ_S^{LW} was stable, and agreed with the values of 42.2 mJ/m^2 and 39.9 mJ/m^2 reported by Wu [*Wu,* 2001] and Giese et al. [*Giese et al.,* 1991], respectively.

For kaolinite the liquid drops infiltrated into the pores of the colloid film, as indicated by the decrease in drop volume (Figure 3.2). As the drop volume decreased, the drop diameter for water and formamide increased, and the contact angle decreased. The increase in drop diameter was caused by two processes: (1) polar (acid-base) interactions between the solid and the polar liquids, and (2) drop imbibition into the pores of the colloid film. The former process is similar to what was observed for smectite. The latter process, however, causes false contact angle readings, and correct contact angle readings should be done at 0 s. For diiodomethane, the drop volume also decreased, but at a much lower rate than compared to water and formamide. The colloid film imbibed the diodomethane, but the imbibition was slow because of its high viscosity. Illite and goethite showed very similar behavior as compared to kaolinite (Table 3.3).

Our data for kaolinite and illite agree with literature data when appropriate measurement times are compared. According to Breiner et al. [*Breiner et al.,* 2006], γ_S^{LW}, γ_S^+, γ_S^- are 40, 1.08, and 44 mJ/m^2, which are similar to the values at 0 s in Table 3.3. According to Giese and van Oss [*Giese and van Oss,* 2002], γ_S^{LW}, γ_S^+, γ_S^- of illite are 40.2, 1.3, and 42.6 mJ/m^2, which are similar to the values at 20 s in Table 3.3. The time dependence of the contact angle shows the importance of accurate time recording

for contact angle measurements for porous colloid films.

For hematite, contact angles, drop diameters, and drop volumes remained constant during the 20-s measurement period (Figure 3.2). This indicates that there were no interactions and imbibition of liquid into the colloid film. We believe that this was because of the spherical shape of the hematite particle, which formed a non-porous film with a periodical surface roughness. In the literature, there is a great variation of contact angles reported for hematite. This is likely due to different types of hematite used in different studies. According to Giese and van Oss [*Giese and van Oss,* 2002], γ_S^{LW}, γ_S^+, γ_S^- of synthetic hematite are 45.6, 0.3, and 50.4 mJ/m^2, and for natural hematite are 36.5, 0.0, and 17.8 mJ/m^2.

Based on the experimental results, we can distinguish three types of mechanisms during contact angle measurements with subsurface colloids (Figure 3.3). For swelling films, like smectite, the colloid film seals itself when in contact with a polar liquid, but acid-base interactions can cause the drop shape to change with time. The contact angle change with time reflects the modification of the surface with time. For non-swelling, porous films, such as kaolinite, illite, and goethite, the drop shape changes because of both acid-base interactions and imbibition, thereby causing false contact angle readings after the initial drop has been put on the colloid film surface. Because of interactions and imbibition, the most accurate contact angle should be the initial contact angle. For a non-swelling, non-porous films, such as hematite, the drop shape remains stable over time.

3.4.3 Sessile Drop Method (Dynamic)

The dynamic sessile drop method can provide advancing and receding contact angles as a function of time. We again only show the data for smectite, kaolinite, and hematite, as illite and goethite showed similar behavior as kaolinite (Figure 3.4). The dashed lines in the figure separate increasing from decreasing drop volume, as controlled by the liquid supply syringe.

For smectite, as the drop volume of water and formamide increased, the contact angles initially decreased and reached a plateau (Figure 3.4a). This plateau represents the mean advancing contact angle [*Lam et al.,* 2001]. For diiodomethane, the contact angle was constant because there were no interactions with the solid surface. When the drop volume was decreased after 60 s, the drop diameters for both water and formamide still increased, and then decreased. Receding contact angles decreased for all three liquids, and did not reach a constant value. For diiodomethane, the drop diameter remained constant, indicating a non-slip boundary at the air-liquid-solid interface [*Lam et al.,* 2002].

For kaolinite, the advancing contact angles were fairly constant for the three liquids (Figure 3.4b). The diameters of the liquid drop increased when the drop volume increased, and remained constant for a few seconds after flow was reversed, and then decreased quickly. The colloid film imbibed all three liquids, but the rate of imbibition was much smaller than the rate of drop volume increase, therefore, the imbibition had negligible effect, and the advancing contact angles remained constant.

For hematite, the drop diameters for water and formamide remained initially constant when the drop volume was increased, but the contact angles increased at a high rate (Figure 3.4c). When the drop size exceeded a critical limit, the drop diameter jumped to a new position, and remained constant again. This led to a typical slip/stick pattern of the advancing contact angle [*Lam et al.,* 2002*; Kwok et al.,* 1996*; Kwok et al.,* 1998]. The slip/stick pattern was bounded by a lower and upper critical contact angle, and the range was larger for water than for formamide. No distinct slip/stick pattern was observed for diiodomethane. The different behavior among the three liquid drops can be explained by their different Bond numbers: the water drop had the smallest Bond number (Bo = 37), and could keep its shape better than the formamide drop (Bo = 46), and the diiodomethane drop (Bo = 184).

The dynamic sessile drop method was useful in determining the advancing contact angles for smectite and kaolinite. The slip/stick pattern observed for hematite did not allow us to exactly determine the contact angles in this case, and the contact angles cannot be used to calculate surface tensions [*Kwok et al.,* 1998]. Receding contact angles could not be obtained from our experiments, because the receding contact angles were not stable.

3.4.4 Wilhelmy Plate Method

From the Wilhelmy plate method, both advancing and receding contact angles can be obtained by immersion and emersion of the coated colloid films. Figure 3.5 shows the

forces measured as a function of immersion depth for complete immersion-emersion loops. Only the linear portions of the force curves were used to calculate the contact angles. The force curves show a distinct contact angle hysteresis, with the advancing contact angles always larger than the receding ones (Table 3.4). The largest hysteresis was observed for smectite and hematite with water. We attribute this pronounced contact angle hysteresis to swelling behavior (smectite) and surface roughness (hematite).

For kaolinite, illite, and goethite, the receding contact angles were zero for all liquids (Table 3.4). Zero-degree receding contact angles were also reported by Bachmann et al. [*Bachmann et al.,* 2003], who measured contact angles of soil aggregates with the Wilhelmy plate method. The zero-degree contact angles are likely caused by imbibition of liquid into the porous films or aggregates during plate immersion. The Wilhelmy plate method has successfully been used to determine contact angles for other types of colloidal and porous materials, such as gold colloids [*Abe et al.,* 2000] and soil aggregates [*Bachmann et al.,* 2003*; Woche et al.,* 2005].

3.4.5 Thin-layer Wicking Method

We chose kaolinite, illite, and goethite as the samples for the thin-layer wicking clay, because the films formed by these colloids have microporous characteristics (Figure 3.1). Smectite and hematite films, which swell and have no microporosity, respectively, cannot be used for the thin-layer wicking. Results for kaolinite, illite, and goethite are shown in Figure 3.6 and Table 3.4.

The experimental data follow the theoretical trend given by Equation 3.1 closely (Figure 3.6), indicating that the thin-layer wicking method was well suited to calculate the contact angles. The effective pore sizes R_{eff} of kaolinite, illite, and goethite were 233, 173, and 387 nm, which are all smaller than the particle diameters (Table 3.1). This is a consequence of the platy and rodlike particle shape of the colloids, which upon deposition orient themselves in a thin film, causing the pore size to become smaller than the particle size [*Li et al.,* 1994]. For illite, the thin film could be peeled off the glass slide, and wicking results with the film alone were identical to the ones where the illite film was on the glass slide. This confirmed that the glass slide itself did not affect the measurement.

The contact angles obtained from the thin-layer wicking method (Table 3.4) are different than those reported in the literature. For kaolinite and the thin-layer wicking method, Wu [*Wu,* 2001] reported contact angles of 46.1^o for water, 27.2^o for formamide, and 34.5^o for diiodomethane, and Breiner at al. [*Breiner et al.,* 2006] reported contact angles of 34^o for water. For illite and goethite, we did not find literature data. The values reported by Wu [*Wu,* 2001] are larger than ours, likely because Wu [*Wu,* 2001] did not pretreat their kaolinite (no removal of organic matter and iron oxides). Breiner at al. [*Breiner et al.,* 2006] pretreated their kaolinite by removing organic matter and sesquioxides, and their contact angle for water is more similar to ours.

3.4.6 Column Wicking Method

Figure 3.7a shows the results for three replicates of the glass bead measurements with hexane to check the method performance. Three stages can be distinguished in the weight-time curves [*Goebel et al.,* 2004]: in stage 1, at very short times, the bottom boundary of the sample holder affects the measurements; in stage 2, interparticle pores are filled, and a linear increase of the weight-time curve is obtained; in stage 3, the pore space is either completely filled, resulting in a cease of the weight gain, or intraparticle pores begin to fill, resulting in a on-linear weight-time response. For our glass beads, no intraparticle pores were present, and we obtained an ideal weight-time response for hexane (Figure 3.7a) as well as for the other fluids (Figure 3.7b).

For the subsurface colloids, however, most of the time no distinct stage 2 could be identified (Figure 3.7c-f), and therefore, no contact angles could be calculated. The pore structure of the packed subsurface colloids changed as fluids imbibed the materials, thereby, invalidating the assumptions inherent in the Washburn method. Colloids dispersed in water and formamide and, in addition, smectite swelled. No dispersion and swelling was observed for diiodomethane, resulting in nearly linear stage 2 curves.

3.4.7 Comparison of Contact Angles and Surface Tensions

The contact angles obtained from the different methods are summarized in Table 3.4 and Figure 3.8. The data show that there were considerable differences in the contact

angles determined using the different methods. The best agreements among the different methods were obtained with kaolinite (except for diiodomethane). For water, the static and advancing contact angles with kaolinite were within 3^o for the different methods, and no significant differences were observed (Table 3.4). For formamide, the static and advancing contact angles with kaolinite were within 9^o and, except for the thin-layer wicking, the angles were again not statistically different. Larger differences were observed for diiodomethane.

The other colloids generally showed large differences among methods. But the differences among the methods and the colloids were not consistent. For instance, for smectite, the static sessile drop and the Wilhelmy plate method (advancing) gave similar contact angles with water and formamide; but for illite, goethite, and hematite, these two methods gave significantly different contact angles (Table 3.4). For illite, goethite, and hematite, no consistent patterns among different methods were observed. Differences in contact angles among the methods ranged from 20^o to 33^o for water, 20^o to 25^o for formamide, and 4^o to 40^o for diiodomethane (Figure 3.8).

The thin-layer wicking method often produced contact angles that deviated considerably than those determined from other methods (Figure 3.8). Although thin-layer wicking has been frequently used for powders [*Wu,* 2001*; Teixeira et al.,* 1998*; Chibowski and Holysz,* 1992*; Chibowski and González-Caballero,* 1993], it appears that for our subsurface colloids, its suitability is limited. The column-wicking method was also not suited for contact angle measurement; similar observations were reported by

others using powdered liposomes [*Tejas et al.,* 2001], microporous membranes [*Tróger et al.,* 1998], and soil materials [*Bachmann et al.,* 2003*; Goebel et al.,* 2004].

Contact angles determined with a single method usually showed a standard deviation of up to about 3 degrees (Table 3.4), so the precision of the individual methods was good. However, the inter-method variability was often much larger than the intra-method variability. Thus, whereas the precision of a single method was good, the method may not provide accurate results. The optimal (most accurate) method for a given colloid has to be determined on a case by case basis.

The surface tension components and parameters obtained from the different methods are listed in Table 4.3. Using the van Oss-Chaudhury-Good approach, contact angle with 1^o standard deviation may translate into errors for the solid surface tension values of about 2% [*Wu,* 2001]. Compared with the contact angles, there was less variation of the surface tensions among the different methods. The data show that the solid surface tension γ_S was in the range from 46 to 57 mJ/m^2. The Lifshitz-van der Waals component γ_S^{LW} made up the largest part of the surface tension (values ranged from 36 to 50 mJ/m^2). The electron-acceptor parameter γ_S^+ was usually small (0.1 to 3.3 mJ/m^2) and the electron-donor parameter γ_S^+ large (6 to 56 mJ/m^2). These trends corroborate literature data [*Wu,* 2001*; Giese and van Oss,* 2002].

Based on all our measurements, and requiring that at least two methods should give similar contact angles, we can make the following recommendations for water (Table 3.6). For kaolinite, all methods except column wicking were suitable and gave

similar results. For smectite, the static sessile drop and the Wilhelmy plate method are recommended. For illite, all methods gave significantly different results, but dynamic sessile drop and Wilhelmy plate methods gave the most similar contact angles. For goethite and hematite, static and dynamic sessile drop methods are recommended.

3.5 Conclusions

Our results have shown that large differences can exist between contact angles of subsurface colloids measured with different methods. In addition, the pretreatment of colloids is important to consider and affects the contact angle measurement. Contact angles may show a time-dependence, which also needs to be taken into account when interpreting experimental measurements. It is therefore not surprising that a large variation of contact angles for subsurface colloids is reported in the literature. Based on our systematic comparison of different methods, we can recommend specific methods for specific colloids (Table 3.6).

In terms of the contact angles themselves, our data show that subsurface colloids generally have fairly large contact angles (equilibrium and advancing): kaolinite and goethite had a contact angle of about 25^o, smectite 40^o to 50^o, illite 25^o to 45^o, and hematite 45^o. There was a pronounced contact angle hysteresis, receding contact angles were 10^o for smectite, 32^o for hematite, 0^o for kaolinite, illite, and goethite.

3.6 Tables and Figures

Table 3.1: Characteristics of colloids.

Sample	Particle diameter[a] (nm)	Electrophoretic mobility[a] (μm s^{-1})/(V cm^{-1})	ζ potential[b] (mV)	Particle shape[c]
Ca-smectite (SAz1)	1069 ± 198	−1.12 ± 0.01	−14.2 ± 0.1	irregular thin flakes
Ca-kaolinite (KGa1b)	1280 ± 43	−0.24 ± 0.01	−3.0 ± 0.1	hexagonal platy
Ca-illite (No. 36)	915 ± 181	−1.58 ± 0.05	−20.1 ± 0.6	irregular platy
Goethite	1814 ± 38	2.10 ± 0.04	26.6 ± 0.6	acicular
Hematite	146 ± 1	2.77 ± 0.02	35.2 ± 0.3	spherical

± denotes one standard deviation.

[a] measured by dynamic light scattering at pH 6.0 and 0.1 mM $CaCl_2$ electrolyte background.

[b] calculated from the von Smoluchowski equation.

[c] determined by electron microscopy (SEM and TEM).

Table 3.2: Density, viscosity, air-liquid surface tension γ_L, and surface-tension components of test liquids at 20°C. [γ_L^{LW}: Lifshitz-van der Waals component (apolar); γ_L^+: electron-acceptor component (polar); γ_L^-: electron-donor component (polar)].

Liquid	Density	Dyn. Viscosity	γ_L	γ_L^{LW}	γ_L^+	γ_L^-
	(kg m^{-3})	(N s m^{-2})	(mJ m^{-2})	(mJ m^{-2})	(mJ m^{-2})	(mJ m^{-2})
Hexane	663[b]	0.00029[b]	18.4	18.4	0	0
Water	998	0.00100	72.8	21.8	25.5	25.5
Formamide	1130[c]	0.00376[c]	58.0	39.0	2.28	39.6
Diiodomethane	3320[c]	0.00280[c]	50.8	50.8	0	0

Surface tensions and surface tension components are from van Oss[*van Oss*, 2006].

[b,c] from J.T. Baker and Acros Organic.

Table 3.3: Contact angles, surface tension components, and parameters of subsurface colloids determined using static sessile drop method.

		Contact Angle			Surface Tension				
Subsurface colloids	Time	Water	Formamide	Diiodomethane	γ_S	γ_S^{LW}	γ_S^{AB}	γ_S^+	γ_S^-
	(s)	(degree)	(degree)	(degree)	(mJ/m^2)	(mJ/m^2)	(mJ/m^2)	(mJ/m^2)	(mJ/m^2)
Ca-smectite	0	55.7 ± 1.4	31.2 ± 0.6	38.3 ± 1.2	50.8	40.5	10.3	1.6	17.2
	10	44.5 ± 0.9	23.2 ± 0.9	38.3 ± 1.1	53.8	40.5	13.4	1.7	26.9
	20	41.4 ± 0.9	21.2 ± 0.8	38.3 ± 1.2	54.5	40.5	14.0	1.7	29.7
Ca-kaolinite	0	27.8 ± 0.4	13.7 ± 0.9	21.9 ± 1.3	56.4	47.2	9.2	0.5	42.7
	10	20.8 ± 0.8	7.4 ± 1.3	17.1 ± 0.9	57.0	48.6	8.4	0.4	47.6
	20	17.8 ± 0.6	6.5 ± 1.2	15.3 ± 0.5	56.8	49.0	7.7	0.3	49.7
Ca-illite	0	43.3 ± 0.3	21.1 ± 0.7	30.8 ± 1.4	55.2	43.9	11.3	1.2	27.6
	10	31.9 ± 1.1	17.4 ± 1.8	30.0 ± 1.6	55.6	44.2	11.3	0.8	39.4
	20	29.3 ± 1.3	16.8 ± 1.5	29.6 ± 1.6	55.4	44.4	11.0	0.7	42.1
Goethite	0	22.8 ± 1.8	24.1 ± 1.0	19.4 ± 0.4	50.9	48.0	2.9	0.0	52.6
	10	0 ± 0	15.3 ± 3.0	12.8 ± 0.1	53.0	49.5	3.5	0.1	59.0
	20	0 ± 0	0 ± 0	8.1 ± 0.4	56.1	50.3	5.8	0.2	55.9
Hematite	0	46.9 ± 2.3	18.5 ± 1.7	25.0 ± 0.8	56.6	46.2	10.4	1.2	22.6
	10	46.5 ± 2.4	18.5 ± 1.8	25.5 ± 1.0	56.5	46.0	10.5	1.2	23.1
	20	46.4 ± 2.4	18.5 ± 1.8	25.4 ± 1.1	56.5	46.0	10.5	1.2	23.2

± denotes one standard deviation.

Table 3.4: Contact angles (degrees) of test liquids for subsurface colloids using static sessile drop, dynamic sessile drop, Wilhelmy plate, and thin-layer wicking methods.

	Contact Angles (degrees)		
Subsurface Colloids	Water	Formamide	Diiodomethane
Static sessile drop method (equilibrium contact angle)			
Ca-smectite	55.7 ± 1.4 A	31.2 ± 0.6 A	38.3 ± 1.2 A
Ca-kaolinite	27.8 ± 0.4 A	13.7 ± 0.9 A	21.9 ± 1.3 A
Ca-illite	43.3 ± 1.4 A	21.1 ± 0.7 A	30.8 ± 1.4 A
Goethite	22.8 ± 1.9 A	24.1 ± 1.0 A	19.4 ± 0.4 A
Hematite	46.9 ± 2.3 A	18.5 ± 1.7 A	25.0 ± 0.8 A
Dynamic sessile drop method (advancing contact angle)			
Ca-smectite	41.9 ± 2.5 B	17.2 ± 1.4 B	46.9 ± 0.7 B
Ca-kaolinite	26.2 ± 2.0 A	14.9 ± 3.6 A,B	10.8 ± 1.9 B
Ca-illite	24.0 ± 3.2 B	13.8 ± 1.6 B	32.4 ± 3.2 A
Goethite	25.0 ± 2.9 A	41.2 ± 4.8 B	13.8 ± 0.8 B
Hematite	42.5 ± 11.4 A	35.4 ± 8.3 B	26.4 ± 1.6 A
Wilhelmy plate method (advancing contact angle)			
Ca-smectite	57.1 ± 2.5 A	34.7 ± 2.1 A	50.9 ± 0.6 B,D
Ca-kaolinite	27.3 ± 1.3 A	11.1 ± 0.9 A	20.8 ± 1.9 A
Ca-illite	30.0 ± 0.4 C	20.0 ± 1.7 A	30.6 ± 2.0 A
Goethite	14.2 ± 2.4 B	17.8 ± 1.4 C	8.7 ± 2.3 B
Hematite	71.7 ± 2.0 B	42.3 ± 1.0 C	35.5 ± 0.6 B
Wilhelmy plate method (receding contact angle)			
Ca-smectite	9.9 ± 2.3 C	5.3 ± 1.0 C	25.6 ± 1.7 C
Ca-kaolinite	0 B	0 C	0 C
Ca-illite	0 D	0 C	0 B
Goethite	0 C	0 D	0 C
Hematite	32.3 ± 1.1 C	5.8 ± 0.7 D	23.4 ± 0.4 C
Thin-layer wicking method (advancing contact angle)			
Ca-kaolinite	29.3 ± 2.2 A	19.8 ± 0.3 B	52.0 ± 3.1 D
Ca-illite	56.8 ± 3.4 E	39.1 ± 5.5 D	34.2 ± 4.9 A
Goethite	34.1 ± 3.4 D	20.9 ± 1.8 A	46.7 ± 2.9 D

± denotes one standard deviation. Letters (A, B, C, D, E) denote the statistical difference column-wise for identical colloids: if letters are different then there is a significant difference at the 5% confidence level among colloids of the same type measured with different methods (t-test).

Table 3.5: Surface tension components and parameters of subsurface colloids using static sessile drop, dynamic sessile drop, Wilhelmy plate, and thin-layer wicking methods.

	Surface Tension (mJ/m^2)				
Subsurface Colloids	γ_S	γ_S^{LW}	γ_S^{AB}	γ_S^+	γ_S^-
Sessile drop method (equilibrium contact angle)					
Ca-smectite	50.8 ± 1.7	40.5 ± 0.6	10.3 ± 1.1	1.6 ± 0.2	17.2 ± 1.6
Ca-kaolinite	56.4 ± 1.0	47.2 ± 0.4	9.2 ± 0.6	0.5 ± 0.1	42.7 ± 0.5
Ca-illite	55.2 ± 1.6	43.9 ± 0.6	11.3 ± 1.0	1.2 ± 0.1	27.6 ± 1.7
Goethite	50.9 ± 0.9	48.0 ± 0.1	2.9 ± 0.8	0.1 ± 0.1	52.6 ± 1.8
Hematite	56.6 ± 1.8	46.2 ± 0.3	10.4 ± 1.5	1.2 ± 0.2	22.6 ± 2.8
Dynamic sessile drop method (advancing contact angle)					
Ca-smectite	54.8 ± 2.3	36.0 ± 0.3	18.8 ± 1.9	3.3 ± 0.3	27.2 ± 3.0
Ca-kaolinite	55.9 ± 1.9	49.9 ± 0.3	6.0 ± 1.6	0.2 ± 0.1	44.9 ± 2.4
Ca-illite	55.9 ± 3.5	43.2 ± 1.4	12.7 ± 2.1	0.9 ± 0.2	46.0 ± 3.0
Goethite	49.4 ± 0.2	49.4 ± 0.2	0	0.7 ± 0.6	65.3 ± 6.3
Hematite	48.1 ± 8.4	45.6 ± 0.6	2.5 ± 7.8	0.1 ± 0.2	36.9 ± 16.7
Wilhelmy plate method (advancing contact angle)					
Ca-smectite	47.3 ± 2.8	33.8 ± 0.3	13.5 ± 2.5	2.7 ± 0.5	16.9 ± 3.0
Ca-kaolinite	57.0 ± 1.4	47.5 ± 0.6	9.5 ± 0.8	0.5 ± 0.1	42.4 ± 1.3
Ca-illite	54.3 ± 2.1	44.0 ± 0.8	10.3 ± 1.3	0.6 ± 0.1	42.6 ± 0.9
Goethite	52.8 ± 1.1	50.2 ± 0.3	2.6 ± 0.9	0.1 ± 0.1	55.9 ± 1.6
Hematite	46.8 ± 1.5	41.8 ± 0.3	5.0 ± 1.1	1.0 ± 0.2	6.2 ± 1.6
Wilhelmy plate method (receding contact angle)					
Ca-smectite	56.4 ± 1.5	45.9 ± 0.6	10.4 ± 0.8	0.5 ± 0.1	53.7 ± 1.0
Ca-kaolinite	na	na	na	na	na
Ca-illite	na	na	na	na	na
Goethite	na	na	na	na	na
Hematite	54.5 ± 0.9	44.5 ± 0.2	10.1 ± 0.7	1.4 ± 0.1	18.7 ± 1.4
Thin-layer wicking method (advancing contact angle)					
Ca-kaolinite	54.9 ± 4.4	33.2 ± 1.8	21.7 ± 2.7	2.8 ± 0.5	42.3 ± 2.3
Ca-illite	48.2 ± 6.8	42.4 ± 2.2	5.8 ± 4.6	0.4 ± 0.4	20.1 ± 5.4
Goethite	54.2 ± 4.6	36.1 ± 1.6	18.2 ± 3.0	2.2 ± 0.5	37.8 ± 4.0

± denotes one standard deviation.
na denotes data not available.

Table 3.6: Recommended contact angle measurement methods for subsurface colloids with water.

Subsurface	Contact Angle Measurement Method				
Colloid	Static sessile drop	Dynamic sessile drop	Wilhelmy plate	Thin-layer wicking	Column wicking
Ca-smectite	×	◯	×	◯	◯
Ca-kaolinite	×	×	×	×	◯
Ca-illite	×	◯	×	◯	◯
Goethite	◯	×	×	◯	◯
Hematite	×	×	◯	◯	◯

× denotes recommended method.

◯ denotes not recommended method.

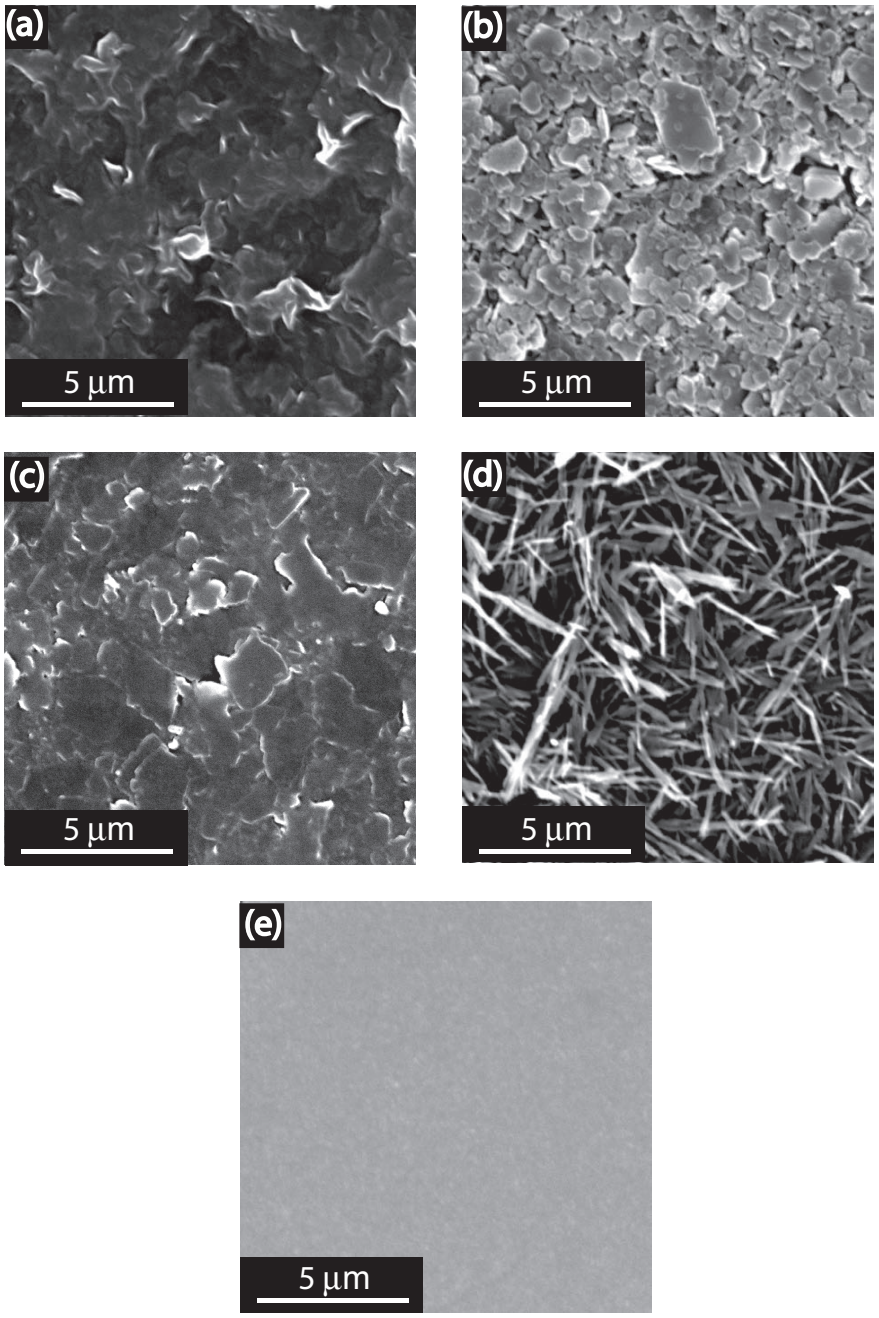

Figure 3.1: Scanning electron micrographs of the film surfaces: (a) smectite, (b) kaolinite, (c) illite, (d) goethite, and (e) hematite.

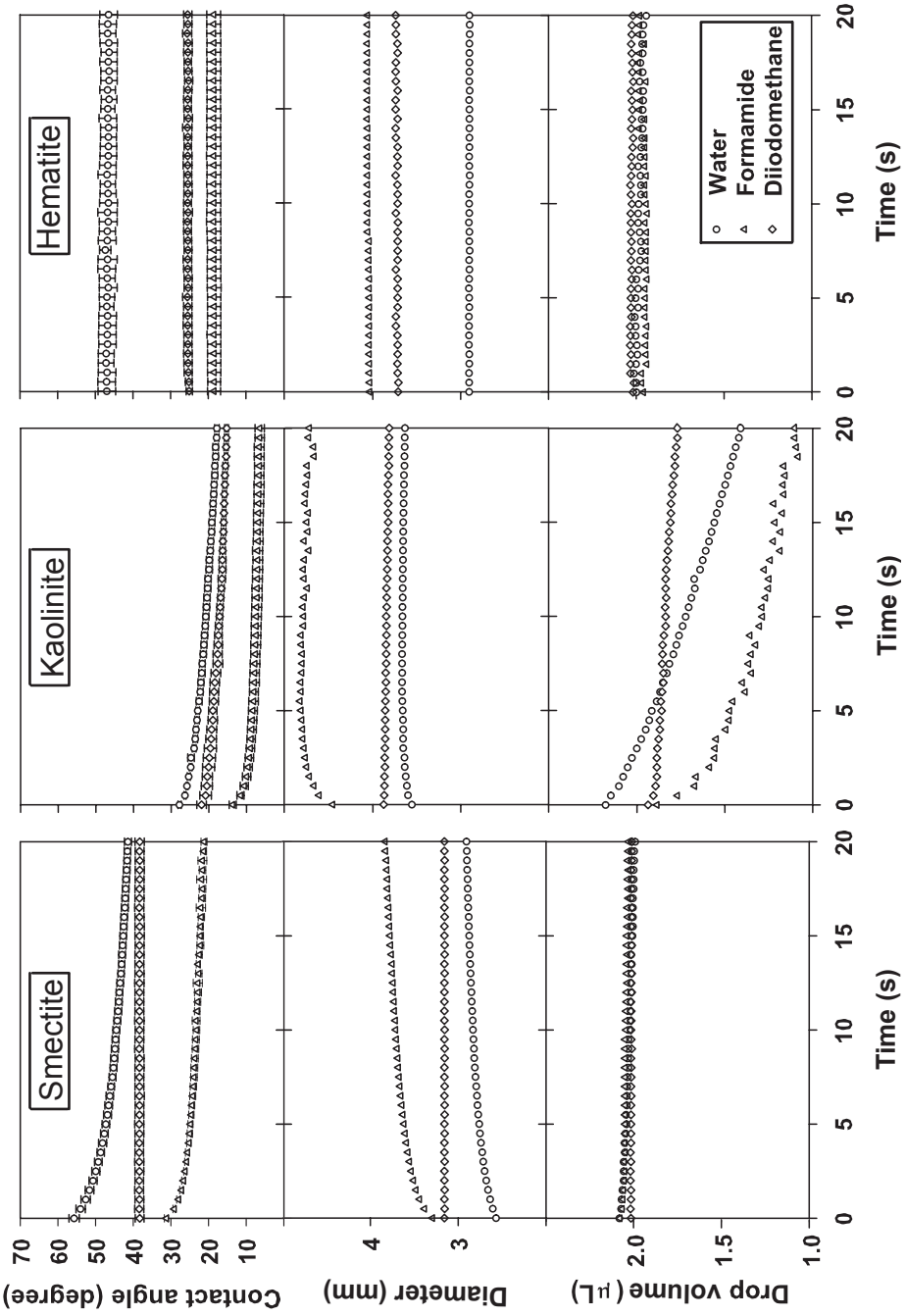

Figure 3.2: Contact angles, drop diameters, and drop volumes as a function of time determined with static sessile drop method. Error bars (only shown for contact angles) indicate standard deviations of five measurements.

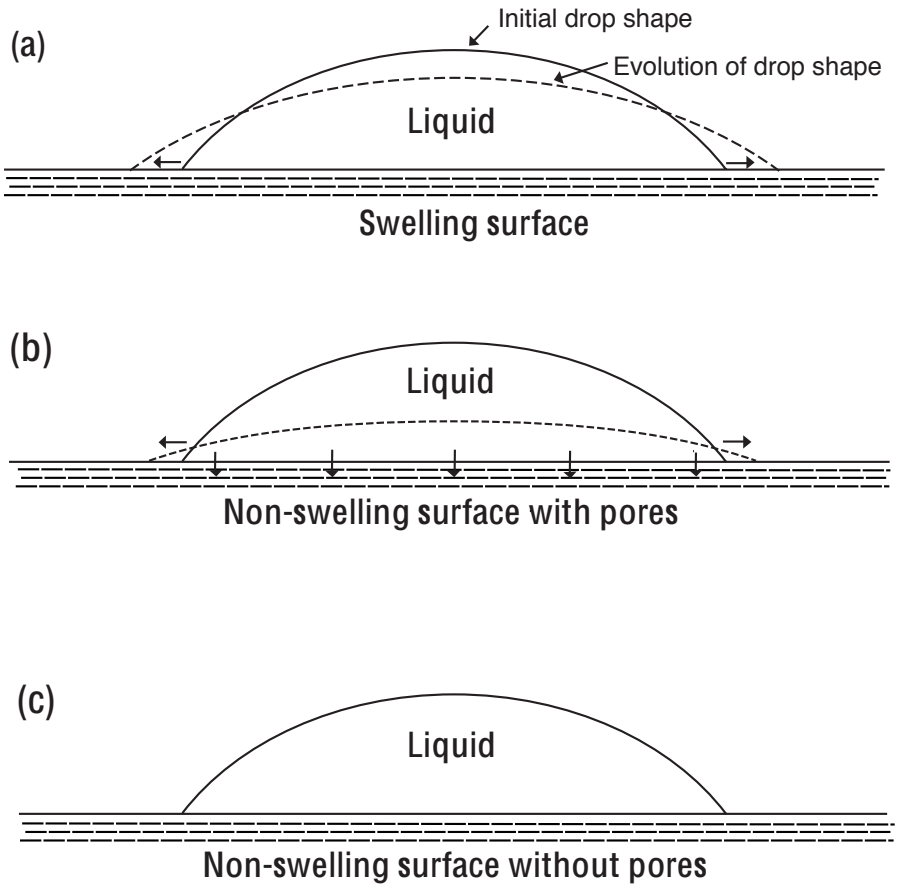

Figure 3.3: Schematic illustration of drop shape behavior with a polar liquid on surfaces of subsurface colloids: (a) smectite, (b) kaolinite, illite, and goethite, (c) hematite.

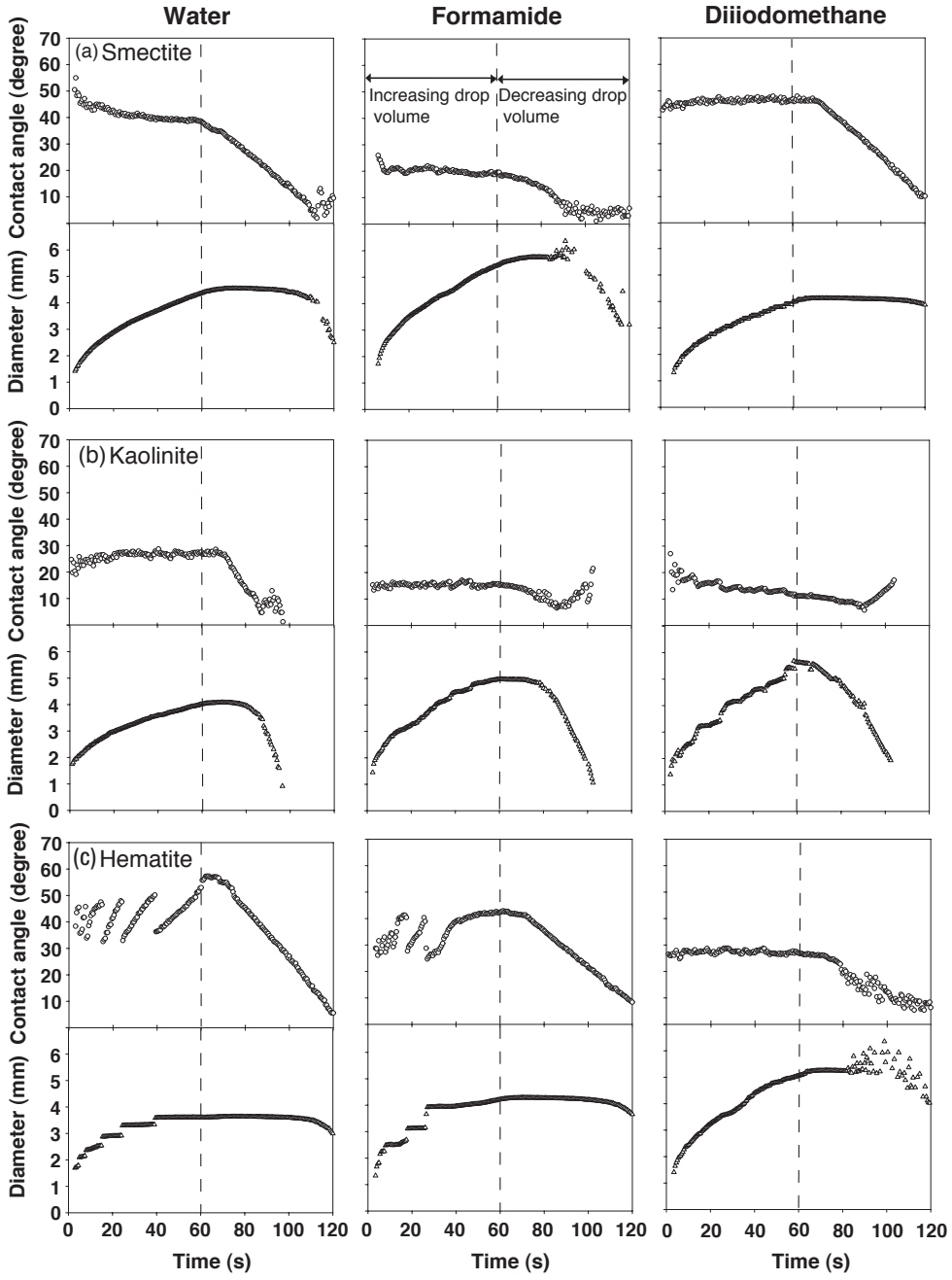

Figure 3.4: Dynamic contact angles and drop diameters of test liquids as a function of time determined by the dynamic sessile drop method: (a) smectite, (b) kaolinite (illite and goethite were similar to kaolinite), (c) hematite. Dashed lines separate increasing from decreasing drop volume.

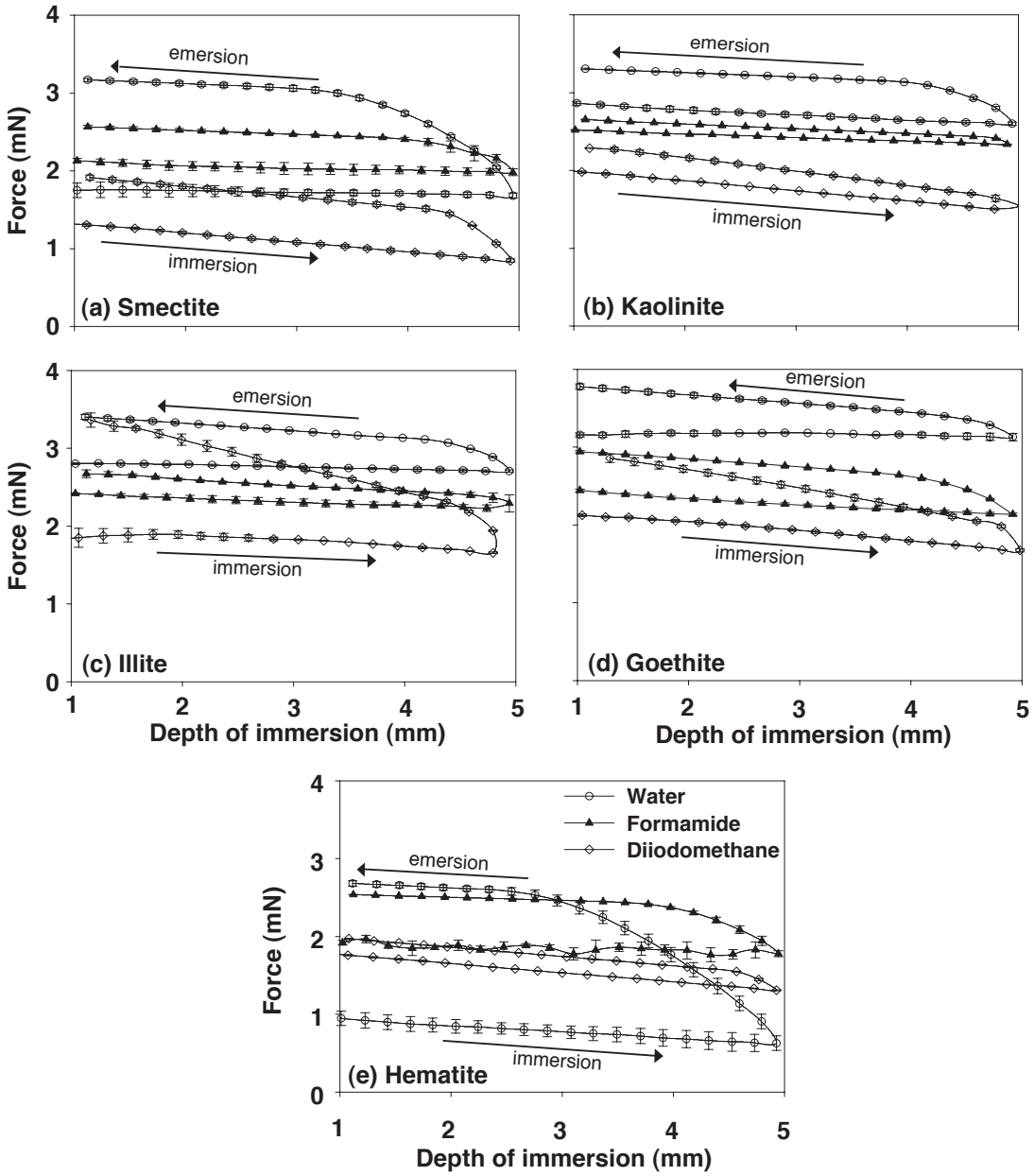

Figure 3.5: Forces measured for different test liquids by the Wilhelmy plate method for an immersion-emersion loop: (a) smectite, (b) kaolinte, (c) illite, (d) goethite, (e) hematite. The arrows show the sequence of immersion and emersion. Error bars indicate standard deviations of five measurements.

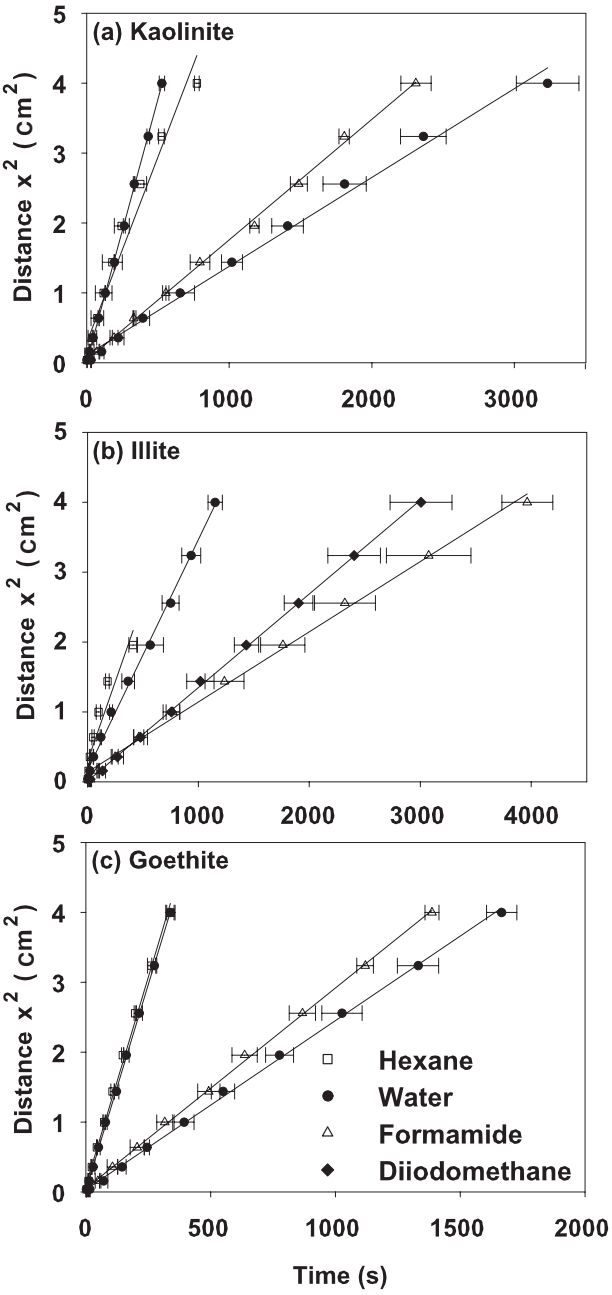

Figure 3.6: Wicking distance squared versus time for different test liquids using thin-layer wicking: (a) kaolinite, (b) illite, (c) goethite. The lines are linear trendlines of the form $x^2 = at$, where a is a fitting parameter given as $a = (R_{\text{eff}}\gamma_{\text{L}}\cos\theta)/(2\eta)$. Error bars indicate standard deviations of three measurements.

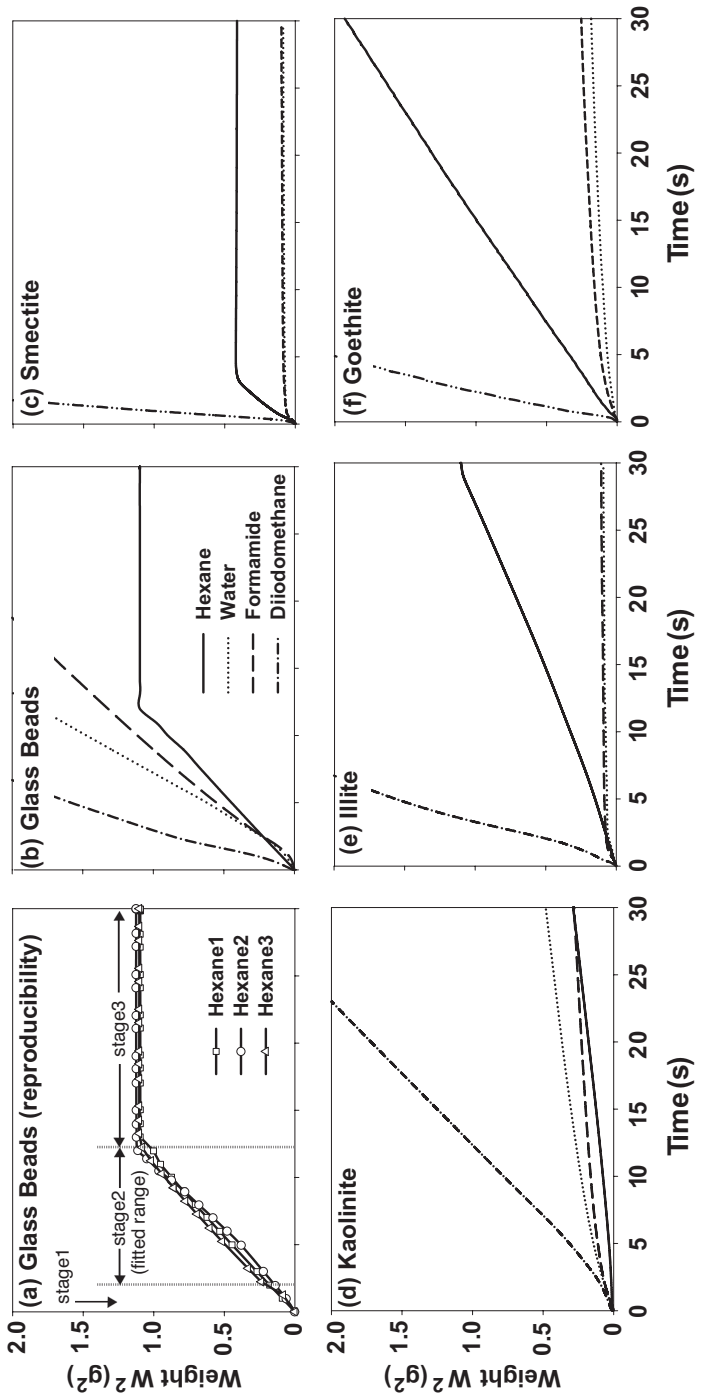

Figure 3.7: Capillary rise curves, wicking weight versus time for different test liquids using the column wicking method: (a) glass beads in hexane (reproducibility), (b) glass beads, (c) smectite, (d) kaolinite (e) illite, and (f) goethite.

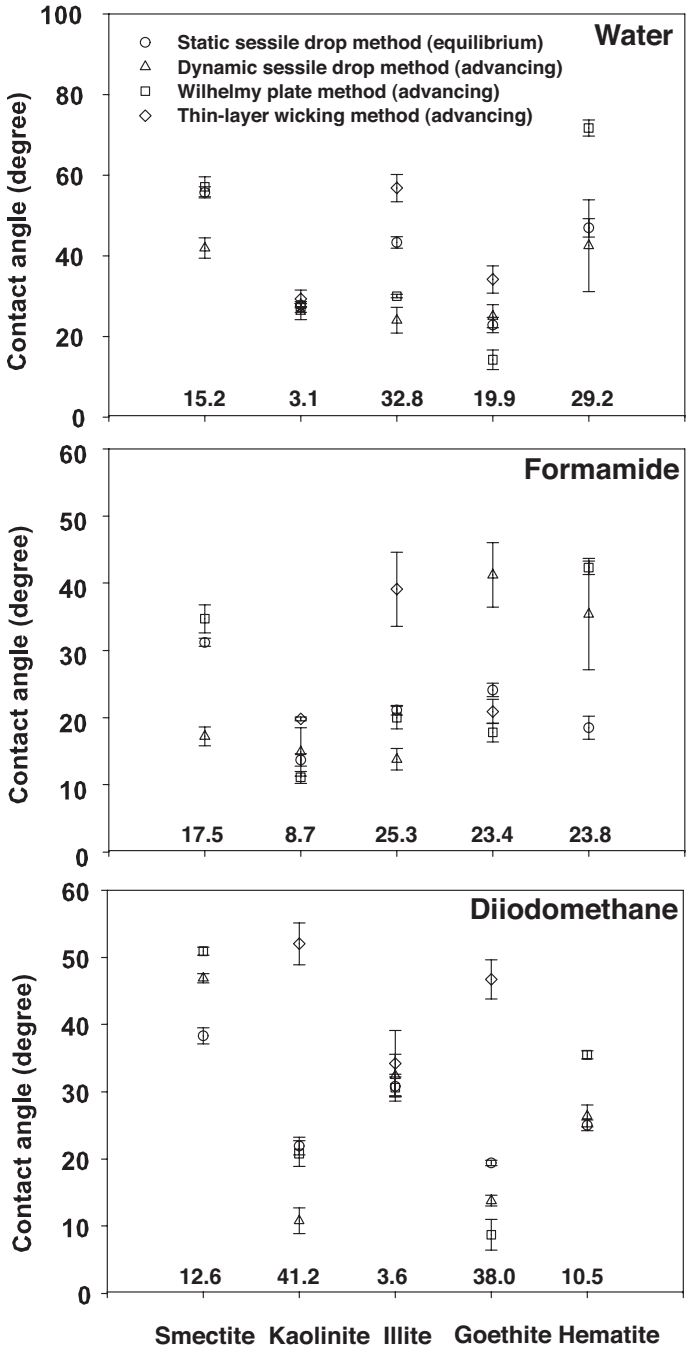

Figure 3.8: Comparison of contact angle measurement with different methods. Bars denote ± one standard deviation. Numbers indicate the range of the different measurements for each colloid.

Chapter 4

Contact Angles and Surface Tensions of Aluminosilicate Clays as Affected by Exchangeable Cations and Relative Humidity

4.1 Introduction

Mineral colloids are the small discrete solid particles indigenously present in subsurface natural porous media, which can be mobilized by means of colloidal, hydrodynamic and other forces [*Sen and Khilar,* 2006]. Colloidal particles generally have dimensions between 1 nm and 2 μm [*Hiemenz and Rajagopalan,* 1997*; Hunter,* 2001]. They possess an electric surface charge, and are typically smaller than inter-granular pores and

---

This chapter will be submitted for publication: Shang, J., M. Flury, J. B. Harsh, and R. L. Zollars, Contact Angles and Surface Tensions of Aluminosilicate Clays as Affected by Exchangeable Cations and Relative Humidity, Colloids and Surfaces A.

fractures in subsurface environments, and they can be transported long distances as mobile solid phases with groundwater movement [*Sen et al.,* 2004]. There exist a variety of inorganic and organic colloidal particles, including aluminosilicate clays, oxides, hydroxides, viruses, bacteria and protozoans, and natural organic matter [*McCarthy and McKay,* 2004].

Inorganic colloids influence containment fate in soils and geological media. Colloids play an important role in facilitating the transport of contaminants [*McCarthy and Zachara,* 1989*; McCarthy and Degueldre,* 1993*; McCarthy,* 1998*; Flury et al.,* 2002*; Zhuang et al.,* 2003]. Whether or not colloids can move through the subsurface, depends on their surface properties. The surface properties of colloids are related to their wettability, flocculation-dispersion, ion exchange, sorption, flotation, and transport [*Breiner et al.,* 2006]. Interfacial interactions are governed, among other factors, by contact angle and solid surface tension.

Determining contact angles is challenging the measurements are affected by many parameters, including temperature [*King,* 1981*; Dekker et al.,* 1998*; She and Sleep,* 1998*; DeJonge et al.,* 1999], water content [*DeJonge et al.,* 1999*; Dekker and Ritsema,* 2000*; deJonge et al.,* 2007*; Bachmann et al.,* 2007], relative humidity [*Chassin et al.,* 1986], organic matter [*Woche et al.,* 2005], particle size [*DeJonge et al.,* 1999], surface roughness [*Eick et al.,* 1975*; Oliver et al.,* 1980*; Drelich et al.,* 1996], surface heterogeneity [*Johnson and Dettre,* 1964*; Dettre and Johnson,* 1965*; Long et al.,* 2005], presence of hydrophobic organic compounds [*Breiner et al.,* 2006], and surface cations [*Giese*

and van Oss, 2002*; Chibowski et al.,* 1993]. For aluminosilicate clays, the pretreatment is also important, as clays often have organic compounds and different cations associated with them [*Shang et al.,* 2008b].

Aluminosilicate clays have a permanent negative charge, which is balanced by exchangeable, surface cations. The type of cations likely changes the contact angle of the clays. *Giese and van Oss* [2002] measured contact angles for smectite clays saturated with various different cations and determined surface surface tension components. They did not report contact angles per se, but listed surface tension components calculated from contact angles. They found that the Lifshitz-van der Waals component γ_{LW} was similar among different types of smectites and different cations on the surface. For SWa-1 and STx-1 smectite, the Li and Na saturated clays had the lowest electron-acceptor parameter γ^+ and the highest electron-donor parameter γ^-, although other smectite clays did not show a consistent trend. Overall, no systematic trends of surface tension components with regard to the type of cation on the surface were observed [*Giese and van Oss,* 2002].

The effects of cations and anions on contact angles and surface tensions of cholesterol have been studied by *Chibowski et al.* [1993]. The presence of cations and anions increased polar acid-base interactions and especially the electron-donor component of the surface tension components, and the contact angle decreased as compared to the absence of the ions. The authors interpreted this as a consequence of a hydration shell around the ions.

Aluminosilicate clays are associated with water molecules, and the amount of water and the thickness of the water films on the clay surfaces is determined by the vapor pressure or relative humidity of the surrounding atmosphere [*Low,* 1981*; Papendick and Campbell,* 1981]. It is expected that the more water is associated with the clays, the lower is the air-water contact angle [*Chassin et al.,* 1986]. *Chassin et al.* [1986] equilibrated smectite at different relative humidities and determined contact angles with sessile drop method. They found that sorbed water molecules on the clay surface modified the free surface energy of the clay and the higher the relative humidity, the lower were the contact angles. Similar results were reported for peat material, where contact angles decreased with increasing relative humidity [*Michel et al.,* 2001].

The effects of cations and relative humidity on contact angle have been studies mainly for smectite clay, and little consideration has been given to the effects of the pretreatment of the clays and the different types of clays. In this study, we therefore focused on investigating the effects of pretreatment, cations, and relative humidity on contact angles and surface tensions of three typical aluminosilicate clays: smectite, kaolinite, and illite. We saturated the clays with Na^+, K^+, Mg^{2+}, or Ca^{2+} and adjusted the relative humidity to 19, 33, 75, or 100%. We measured contact angles as a function of time by using the static sessile drop method.

4.2 Materials and Methods

4.2.1 Clay Minerals

Three aluminosilicate clays were used: Arizona smectite (SAz1), Georgia kaolinite (KGa1b), and illite (Table 4.1). The smectite and kaolinite were obtained from the Clay Minerals Repository (University of Missouri), and illite (No. 36, Morris, Illinois) from Ward's Natural Science (Rochester, NY). The clays, as received from the suppliers, were fractionated by gravity sedimentation in a sodium hexametaphosphate solution (0.5 g/L) to obtain particles smaller than 2 μm in diameter. Selected general properties of the clays used in this study are shown in Table 4.1. The particle shapes were determined by transmission electron microscopy (JEOL 1200EX TEM) (Figure 4.1).

4.2.2 Pre-Treatment of Clays and Saturation with Different Cations

Aliquots of the size-fractionated clays were then treated to remove organic matter with H_2O_2 and to remove iron oxides using the citrate-dithionite method. After these pretreatments, we lowered the pH of the clay suspensions to 4 by titration with 0.1 M HCl to prevent Al^{3+} precipitation on the clay surfaces. The pH 4 suspensions were shaken for three hours, and the supernatant decanted after centrifugation. This procedure was repeated three times. Finally, the clay suspensions were washed with deionized water

by shaking the suspensions for three hours followed by centrifugation and decantation. This washing procedure was repeated until the suspensions reached pH 6.

The washed clays were then made homoionic by treating with 1 M NaCl, 1 M KCl, 0.5 M $MgCl_2$, or 0.5 M $CaCl_2$ to obtain the clays saturated with Na, K, Mg, or Ca respectively. The suspensions were shaken for three hours, centrifuged, supernatant decanted, and the clays dialyzed in deionized water until the electrical conductivity of the dialysate was about 1 μS/cm [*Chorom and Rengasamy*, 1995]. With these pre-treatments, we obtained two types of clays: (1) non-treated clays, (2) clays saturated with Na, K, Mg, or Ca, and dialyzed to 1 μS/cm. All clays were stored in concentrated suspensions at room temperature until use.

Treatment-specific characteristics of the clays are shown in Table 4.2. Average hydrodynamic particle size and electrophoretic mobility were measured by dynamic light scattering using a Zetasizer 3000HAS (Malvern Instruments Ltd., Malvern, UK).

4.2.3 Preparation of Clay Films

Diluted stock suspension (with deionized water) were used to cover microscope cover glass slides (2.2 cm$\times$2.2 cm) with clays following the procedure described by Wu [*Wu*, 2001]. The slides were first cleaned with acetone and water, and then covered with a 1.5 mL clay suspension (1–2% wt/v). The suspension was then evaporated for two days under laminar air flow at 20^{o}C. The relative humidity of the laboratory air was about 33%.

After drying, the clay-coated slides were placed into a air-tight plastic boxes (volume 900 mL), in which we controlled the relative humidity to be 19, 33, 75, and 100%. Humidity control was achieved by placing a beaker of silica gel desiccant, saturated $MgCl_2$ solution, saturated NaCl solution, or deionized water into the box. The system was equilibrated for several days. The relative humidity was monitored by a humidity meter (Model 445814, Extech Instruments), which indicated the vapor pressure reached equilibrium after 3 hours.

Aliquots of the equilibrated clay samples were removed and analyzed for their water potential using a WP4 dewpoint potentiameter (Decagon Devices, Pullman, WA). Relative humidities, water potentials, expected water film thicknesses, and water contents of clays are shown in Table 4.3. Figure 4.2 shows the clay films on the glass slides.

4.2.4 Contact Angle Measurements

Static contact angles were determined with the static sessile drop method using a goniometer (Drop Shape Analysis System, DSA100, Krüss GmbH, Hamburg, Germany). In a comparative study, we have found that the sessile drop method is the preferred method for determining contact angles of smectite, kaolinite, and illite. Our goniometer was equipped with an environmental chamber and a micro-syringe steel needle of 0.5-mm diameter. The environmental chamber helped to minimize evaporation and maintain relative humidity. For contact angle measurements, the syringe needle was

positioned 0.2 mm from the surface of the clay film, and a drop of the test liquid (2 μL) was dispensed at a constant rate of 105 μL/min. The drop shape was monitored with a digital camera for 20 s, and contact angle, drop diameter, and volume were recorded. The contact angle was calculated by the Young-Laplace method (fitting of Young-Laplace equation to the drop shape). The measurements were repeated 5 times for every sample.

4.2.5 Test Liquids

We used polar and apolar liquids for the contact angle measurements: double deionized water (E-pure, Barnstead, electric conductivity $\sim$ 0.5 μS/cm), formamide (99.5% purity, from Acros Organics), and diiodomethane (>99% purity, from Acros Organics) [*Shang et al.,* 2008b]. The liquids were used to calculate surface tension components based on the van Oss-Chaudhury-Good thermodynamic approach [*van Oss,* 2006].

4.2.6 Surface Thermodynamics

Surface tension components of the clays can be calculated from measured contact angles. The surface tension γ_{i} of a material i can be divided into a Lifshitz-van der Waals and a Lewis acid-base component [*van Oss,* 2006*; van Oss et al.,* 1988]:

$$\gamma_i = \gamma_i^{\mathrm{LW}} + \gamma_i^{\mathrm{AB}} \tag{4.1}$$

$$\gamma_i^{\mathrm{AB}} = 2\sqrt{\gamma_i^+ \gamma_i^-} \tag{4.2}$$

where γ_i^{LW} is the Lifshitz-van der Waals (apolar) component ($\mathrm{J/m^2}$) and γ_i^{AB} is the Lewis acid-base (polar) component ($\mathrm{J/m^2}$), which includes γ_i^+, the electron-acceptor parameter ($\mathrm{J/m^2}$) and γ_i^-, the electron-donor parameter ($\mathrm{J/m^2}$). The relationship between the liquid-solid contact angle and the surface tension components is given by the van Oss-Chaudhury-Good approach [*van Oss*, 2006*; van Oss et al.*, 1988]:

$$\gamma_{\mathrm{L}}\left(1+\cos\theta\right) = 2\left(\sqrt{\gamma_{\mathrm{S}}^{\mathrm{LW}}\gamma_{\mathrm{L}}^{\mathrm{LW}}} + \sqrt{\gamma_{\mathrm{S}}^{+}\gamma_{\mathrm{L}}^{-}} + \sqrt{\gamma_{\mathrm{S}}^{-}\gamma_{\mathrm{L}}^{+}}\right) \tag{4.3}$$

where subscript "S" denotes the solid and "L" denotes the test liquid. The known surface-tensions of the liquids provide the values of $\gamma_{\mathrm{L}}^{\mathrm{LW}}$, γ_{L}^{+} and γ_{L}^{-}. The unknown values of $\gamma_{\mathrm{S}}^{\mathrm{LW}}$, γ_{S}^{+} and γ_{S}^{-} are determined by contact angle measurements with three or more different liquids, of which at least two are polar.

4.3 Results and Discussion

4.3.1 Effect of Exchangeable Cations

We hypothesize that the two different pre-treatments resulted in different composition of the exchangeable cations on the clay surfaces. Figure 4.3 shows a schematic of the ionic distribution for the non-treated and the Ca-saturated and dialyzed clays illustrated for smectite. The non-treated clays contained trace amounts of organic matter, and different types of cations on the surface (Figure 4.3a). For the Ca-saturated clay dialyzed to 1 μS/cm, all the exchangeable cations were replaced by Ca (Figure 4.3b).

Electrophoretic mobilities and ζ potentials measured for the different treatments

shown in Figure 4.3 show an interesting trend: for all clay minerals, the Na-saturated clay had lower (more negative) ζ potentials than the non-treated clays. By and large, the Na-saturated clays showed lower ζ potentials than other cation saturations; for smectite and illite the Na and K-ζ potentials were similar. Ca and Mg showed generally the least negative ζ potentials. This difference effect of the monovalent and bivalent cations on ζ potential is expected based on their stronger attraction to the mineral surfaces.

The contact measurements showed good reproducibility, as indicated by small standard deviations ranging from 0.5 to 2.5 degrees (Table 4.4). The non-treated smectites had significantly smaller contact angles with water than the dialyzed smectites. On the contrary, non-treated illite had a larger contact angle than the dialyzed illites. No differences among treatments were found for kaolinite. However, generally, little differences in contact angles were observed among the different different treatments after dialysis, suggesting that the specific cation on the surface of the clays did not effect contact angles.

The surface tensions calculated from the measured contact angles are shown in Table 4.4. The Lifshitz-van der Waals components γ_s^{LW} and the electron acceptor parameters γ_s^+ were similar among treatments, and different clays. The electron donor parameter γ_s^-, however, reflected the differences in contact angles as discussed above.

Giese and van Oss [2002] reported surface tension components for several clays and cation saturations. Their values of γ_s^{LW} for SAz-1 smectite are similar to our

treated smectite values, and they observed little differences among different cations types. The electron donor parameters γ_s^- from *Giese and van Oss* [2002] were similar to our non-treated smectite, but larger than our dialyzed smectite values. *Chibowski et al.* [1993] reported effects of cations on contact angles of cholesterol, and they found significant differences among contact angles for different cation treatments. However, for clay minerals the effect of cations seems to be negligible.

The electron donor parameters γ_s^- can be used as an indicator for the degree of hydrophilicity. *van Oss* [2006] proposed that if $\gamma_s^- >\sim 28$ mJ/m^2, the compound is hydrophilic. The cutoff value is somewhat arbitrary, but trends in γ_s^- can be interpreted as changes in hydrophilicity. Figure 4.4 shows the change of γ_s^- with time for smectite. With contact time, γ_s^- increased until a plateau was reached after 5 to 15 s, suggesting that the surface became more hydrophilic with contact time with water. The non-treated surface was the most hydrophilic surface, except for the Na-saturated smectite, whose γ_s^- value surpassed that of the non-treated surface with time.

4.3.2 Relative Humidity Effect

To assess the effects of relative humidity on contact angles, we measured contact angles at four different relative humidities (Table 4.5 and Figure 4.5). Overall, we did not observe clear trends in contact angles as a function of relative humidity. However, contact angles with water tended to be lowest at 100% relative humidity. Correspondingly, the contact angles for the apolar diiodomethane were usually highest at 100% relative

humidity. At 100% relative humidity, the aluminosilicate clay surface were covered with the thickest water layer and possessed the largest swelling, thereby rendering the surfaces the most hydrophilic.

Increasing relative humidity mainly changed the particle sizes. Figure 4.6a shows that the interlayer hydration of clay minerals with different interlayer cations is varied. Figure 4.6b shows that as relative humidity changes from low to high the water molecule layers around the particles can not only increase but also the interlayer spacing between layers of clays can increase. Relative humidity can change the degree of interlayer hydration and increase equilibrium interlayer spacing values of clays [*Raymond and Kerns*, 1967].

For clays, the charge density of the particles also changed with relative humidity because the increased water thickness around the particles changed the particle volume, but the total charge was the same. The charge density decreased with increasing relative humidity. For polar liquids, decreasing the charge density will increase the contact angle on particles because of decreasing polar interaction. Increasing water thickness will decrease the contact angle on particles because of increasing the ability to lose electron. So, the contact angle of polar liquids on colloids changed with relative humidity, depending on two factors (1) charge density, and (2) water thickness. Charge density increased contact angle with increasing humidity, and water thickness decreased contact angle with increasing humidity. Therefore, the trend of contact angle of polar liquids with humidity sometimes increased and sometimes decreased,

which depended on both factors. Whether the increase or decrease of contact angles depends on which factor is the dominant under different relative humidities. For different colloids, the size effect of these two factors are different, so the changes to the contact angles of different colloids varies and depends on the sum effects of these two factors which vary with the surface property of the particles.

The charge density has no effect on apolar liquids. But the increase of water thickness changes the particle size and the inter-surface interaction which is related to van der Waals forces. Van der Waals interaction includes the interactions between two permanent dipoless (orientation forces), a permanent dipole and an induced dipole (induction forces) and a fluctuating dipole and an induced dipole (dispersion forces) [*Giese and van Oss,* 2002]. These three kinds of interaction energies for all three vary as the inverse of the distance raised to the sixth power [*Giese and van Oss,* 2002]:

$$V_{orientation} = -\mu^4/kTl^6 \tag{4.4}$$

$$V_{induction} = -\alpha\mu^2/l^6 \tag{4.5}$$

$$V_{dispersion} = -\frac{3}{4}\alpha^2 h\nu/l^6 \tag{4.6}$$

where μ is the dipole moment, k is the Boltzmann constant, T is the absolute temperature, α is the polarizability, l is the inter-surface distance, ν is the main dispersion frequency and h is the Planck's constant.

Relative humidity increases the size of the particle. The inter-surface distance l increases, then the Van der Waals forces decrease, and γ_s^{LW} decreases according to

Eqs. 4.4, 4.5, and 4.6. As relative humidity increased from 19% to 100%, γ_s^{LW} decreased for the clays. *Michel et al.* [2001] also found that the surface tension parameter γ_s^{LW} increased when water potentials decreased and relative humidity decreased, based on contact angle measurement and surface tension calculations.

4.4 Conclusions

Our results have shown that surface cations had no effects on the Lifshitz-van der Waals component γ_s^{LW}, and cations Na^+, K^+, Mg^{2+}, and Ca^{2+} almost had no or very small effects on γ_s^-. Relative humidity decreased γ_s^{LW}.

4.5 Tables and Figures

Table 4.1: General properties of aluminosilicate clays used in this study.

Clay type	Origin/Designation	Layer charge per half unit-cell $[O_{10}(OH)_{10}]$[a] (elementary charge, e)	CEC[a] ($cmol_c/kg$)	d-spacing[a] (nm)	Mineralogy[b]
Smectite	SAz-1	0.25–0.40	70–110	1.3–1.6	98% smectite [1% quartz, 1% other]
Kaolinite	KGa-1b	0.20–0.50	50–65	0.7	96% kaolinite and trace dickite [3% anatase, 1% crandallite+mica and/or illite]
Illite	Morris No. 36	0.60–0.90	160–230	1	na[c]

[a] *Mermut and Lagaly* [2001].

[b] *Chipera and Bish* [2001].

[c] na: values not available.

Table 4.2: Treatment-specific characteristics of aluminosilicate clays.

Minerals	Particle size[a] (nm)	Electrophoretic mobility[b] (μm s^{-1})/(V cm^{-1})	ζ potential[c] (mV)	Particle shape[d]
non-treated clays				
Non-treated smectite	446 ± 7	−1.21 ± 0.01	−15.4 ± 0.1	irregular thin flakes
Non-treated kaolinite	364 ± 1	−1.70 ± 0.02	−21.7 ± 0.2	hexagonal platy
Non-treated illite	541 ± 3	−1.50 ± 0.01	−19.7 ± 0.2	irregular platy
smectite dialyzed to 1 μS/cm				
Na-smectite	747 ± 57	−2.91 ± 0.03	−37.0 ± 0.2	irregular thin flakes
K-smectite	817 ± 177	−2.97 ± 0.02	−37.9 ± 0.2	irregular thin flakes
Mg-smectite	1031 ± 15	−1.27 ± 0.03	−16.2 ± 0.3	irregular thin flakes
Ca-smectite	1069 ± 198	−1.12 ± 0.01	−14.2 ± 0.1	irregular thin flakes
kaolinite dialyzed to 1 μS/cm				
Na-kaolinite	1019 ± 159	−2.64 ± 0.06	−33.6 ± 0.7	hexagonal platy
K-kaolinite	1145 ± 118	−1.11 ± 0.16	−14.1 ± 2.0	hexagonal platy
Mg-kaolinite	1085 ± 110	−0.88 ± 0.07	−11.2 ± 0.9	hexagonal platy
Ca-kaolinite	1280 ± 43	−0.24 ± 0.01	−3.0 ± 0.1	hexagonal platy
illite dialyzed to 1 μS/cm				
Na-illite	742 ± 58	−3.26 ± 0.04	−41.5 ± 0.5	irregular platy
K-illite	579 ± 68	−3.14 ± 0.05	−40.0 ± 0.7	irregular platy
Mg-illite	858 ± 48	−1.69 ± 0.06	−21.5 ± 0.8	irregular platy
Ca-illite	915 ± 181	−1.58 ± 0.05	−20.1 ± 0.6	irregular platy

± denotes one standard deviation.

[a] measured by dynamic light scattering.

[b] measured at deionized water, 0.1 mM NaCl, KCl, $MgCl_2$ and $CaCl_2$ electrolyte background for the corresponding clays, repectively.

[c] converted from measured electrophoretic mobility using the von Smoluchowski equation.

[d] determined by electron microscopy (TEM).

Table 4.3: Relative humidity and water potentials of clays.

Relative humidity (%)		Water potential (bar)		Water film thickness (μm)		Water adsorption[f]	Humidity control
Measured	Calculated[a]	Measured[b]	Calculated[c]	Calculated[d]	Literature[e]	(g/g)	(at 20^oC)
19	na [h]	<570[g]	−2246	1×10^{-5}	na[h]	0.15	Silica gel desiccant
33	33	<570[g]	−1500	1.2×10^{-5}	na[h]	0.20	Saturated $MgCl_2$ solution [5.9 mol/L]
75	75	−470	−389	1.9×10^{-5}	$< 9 \times 10^{-4}$ ($< 3H_2O$)	0.31	Saturated NaCl solution [6.32 mol/L]
100	100	−0.5	0	1.4×10^{-3} (at −0.001 bar)	4 (at −0.3 bar)	0.56	Double deionized water

[a] calculated results, [b] measured with a WP4 dewpoint meter, [c] calculated with Kelvin equation, [d] *Hough and White* [1980], [e] *Harris* [1981], [f] for smectite from *Chassin et al.* [1986], [g] samples too dry, no measurements could be obtained, [h] data not available.

Table 4.4: Contact angles and surface tension components (0 seconds) of aluminosilicate clays.

Clay colloids	Contact Angle			Surface Tension		
	Water (degree)	Formamide (degree)	Diiodomethane (degree)	γ_s^{LW} (mJ/m^2)	γ_s^+ (mJ/m^2)	γ_s^- (mJ/m^2)
Non-treated smectite	23.8 ± 1.7 A	10.8 ± 1.2 A	42.1 ± 2.5 A	38.5 ± 1.3	1.9 ± 0.3	44.8 ± 1.5
Ca-smectite	42.5 ± 0.4 B	14.4 ± 0.7 B	37.6 ± 0.4 B	40.8 ± 0.2	2.3 ± 0.1	26.1 ± 0.5
Na-smectite	39.2 ± 0.6 B	14.3 ± 0.7 B	37.1 ± 0.2 B	41.0 ± 0.1	2.2 ± 0.1	29.8 ± 0.7
K-smectite	38.5 ± 1.0 B	10.1 ± 0.8 A	37.1 ± 1.0 B	41.0 ± 0.5	2.0 ± 0.1	29.7 ± 1.1
Mg-smectite	40.9 ± 0.9 B	10.7 ± 1.1 A	37.6 ± 0.8 B	40.8 ± 0.4	2.4 ± 0.1	27.0 ± 1.0
Non-treated kaolinite	16.9 ± 0.7 A	13.3 ± 1.4 A	21.8 ± 1.7 A	47.2 ± 0.5	0.3± 0.1	52.0 ± 0.7
Ca-kaolinite	17.0 ± 0.5 A	11.0 ± 0.8 A	18.0 ± 0.4 B	48.3 ± 0.2	0.3 ± 0.1	50.8 ± 0.9
Na-kaolinite	17.1 ± 1.4 A	12.8 ± 0.8 A	22.6 ± 0.8 A	47.0 ± 0.3	0.3 ± 0.1	51.6 ± 1.0
K-kaolinite	17.1 ± 1.9 A	12.2 ± 0.7 A	21.3 ± 1.8 A	47.4 ± 0.6	0.3 ± 0.1	51.5 ± 1.4
Mg-kaolinite	17.5 ± 1.6 A	12.2 ± 0.8 A	19.3 ± 0.9 A,B	48.0 ± 0.3	0.3 ± 0.1	51.3 ± 1.2
Non-treated illite	34.2 ± 0.9 A	11.9 ± 1.5 A	27.6 ± 1.2 A	45.2 ± 0.5	1.1 ± 0.1	35.2 ± 1.0
Ca-illite	26.1 ± 1.4 B	17.2 ± 0.8 B,C	27.3 ± 1.5 A	45.3 ± 0.6	0.5 ± 0.1	45.5 ± 1.4
Na-illite	24.1 ± 1.5 B	15.8 ± 0.6 C	27.3 ± 1.0 A	45.3 ± 0.4	0.5 ± 0.1	46.8 ± 1.4
K-illite	26.0 ± 1.2 B	19.7 ± 0.5 B	28.0 ± 1.1 A	45.0 ± 0.4	0.4 ± 0.1	46.7 ± 1.2
Mg-illite	23.3 ± 0.7 B	16.8 ± 1.0 B,C	26.5 ± 0.6 A	45.6 ± 0.2	0.4 ± 0.1	48.0 ± 0.8

± denotes one standard deviation. Letters (A, B, C) denote statistical differences column-wise at a confidence level of 5% (t-test). If letters are different, then there is a significant difference.

Table 4.5: Contact angles and surface tension components (0 seconds) of aluminosilicate clays with different relative humidities.

Clay colloids	Relative Humidity	Contact Angle			Surface Tension		
		Water	Formamide	Diiodomethane	γ_s^{LW}	γ_s^+	γ_s^-
	(%)	(degree)	(degree)	(degree)	(mJ/m^2)	(mJ/m^2)	(mJ/m^2)
Ca-smectite	19	37.5 ± 0.9	17.2 ± 0.6	35.8 ± 1.2	41.6 ± 0.6	1.5 ± 0.1	32.8 ± 1.0
	33	42.5 ± 0.4	14.4 ± 0.7	37.6 ± 0.4	40.8 ± 0.2	2.3 ± 0.1	26.1 ± 0.5
	75	47.6 ± 0.9	28.1 ± 1.3	49.4 ± 0.8	34.6 ± 0.5	2.7 ± 0.3	24.9 ± 1.3
	100	35.1 ± 0.7	44.7 ± 1.3	56.7 ± 0.6	30.5 ± 0.3	0.4 ± 0.1	54.2 ± 1.8
Ca-kaolinite	19	19.9 ± 0.7	15.9 ± 0.8	18.4 ± 0.6	48.2 ± 0.2	0.2 ± 0.1	50.8 ± 0.7
	33	17.0 ± 0.5	11.0 ± 0.6	18.0 ± 0.8	48.4 ± 0.2	0.3 ± 0.1	51.3 ± 0.4
	75	20.6 ± 1.0	16.9 ± 0.8	23.8 ± 0.9	46.6 ± 0.3	0.3 ± 0.1	50.5 ± 0.9
	100	17.3 ± 1.3	15.4 ± 0.5	53.5 ± 1.4	32.3 ± 0.8	2.9 ± 0.3	50.9 ± 0.9
Ca-illite	19	28.3 ± 0.6	21.3 ± 0.7	27.7 ± 1.1	45.1 ± 0.4	0.4 ± 0.1	45.2 ± 0.7
	33	26.1 ± 1.4	17.2 ± 0.8	27.3 ± 1.5	45.3 ± 0.6	0.5 ± 0.1	45.5 ± 1.4
	75	24.9 ± 1.5	27.4 ± 1.7	34.0 ± 1.3	42.5 ± 0.6	0.3 ± 0.1	52.1 ± 2.0
	100	21.6 ± 1.2	25.6 ± 1.4	51.2 ± 1.4	33.6 ± 0.8	1.6 ± 0.3	53.1 ± 1.4

± denotes one standard deviation.

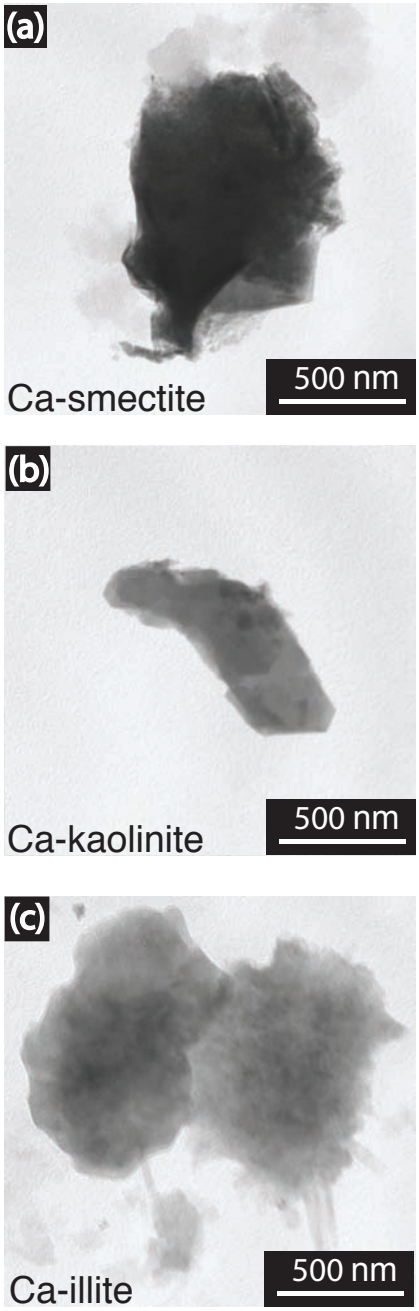

Figure 4.1: Transmission electron micrographs of the aluminosilicate clays: (a) Ca-smectite, (b) Ca-kaolinite, and (c) Ca-illite.

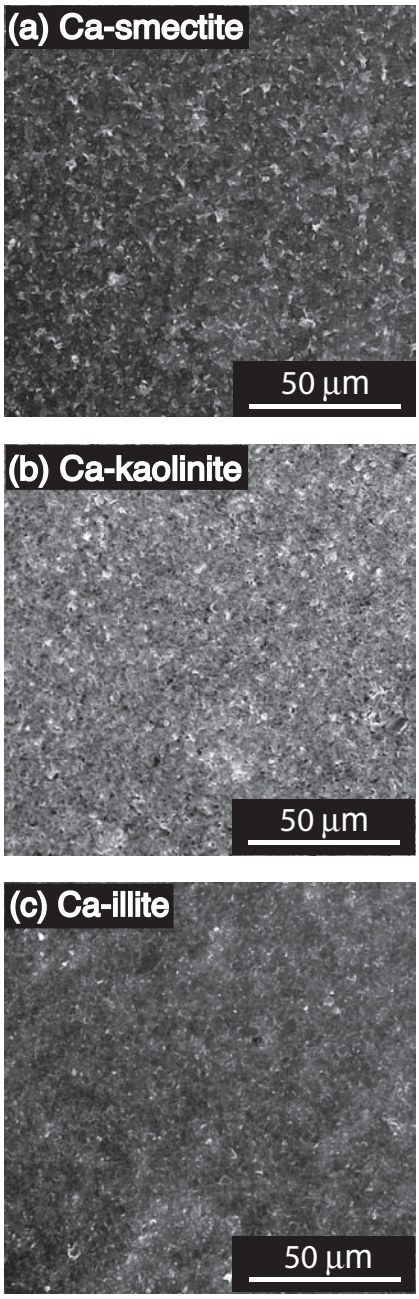

Figure 4.2: Scanning electron micrographs of the film surfaces: (a) Ca-smectite, (b) Ca-kaolinite, and (c) Ca-illite.

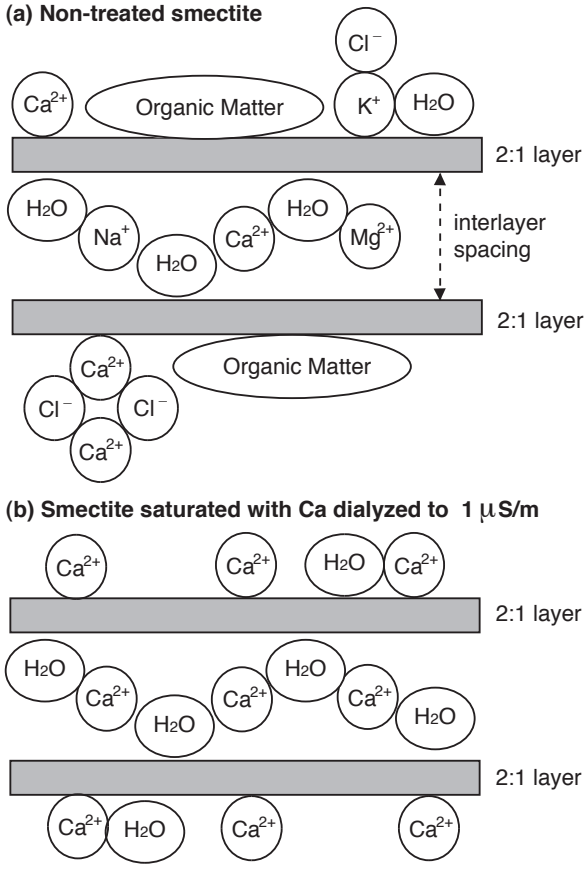

Figure 4.3: Schematic illustration of dried smectite for the two treatments: (a) non-treated smectite, and (b) Ca-saturated smectite dialyzed to 1 μS/cm.

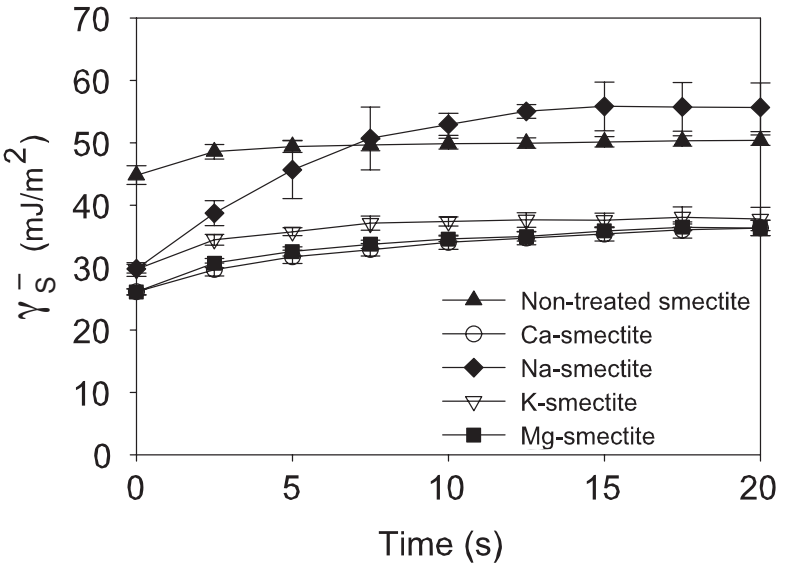

Figure 4.4: The electron-donor parameters, γ_S^-, for smectite as a function of contact time.

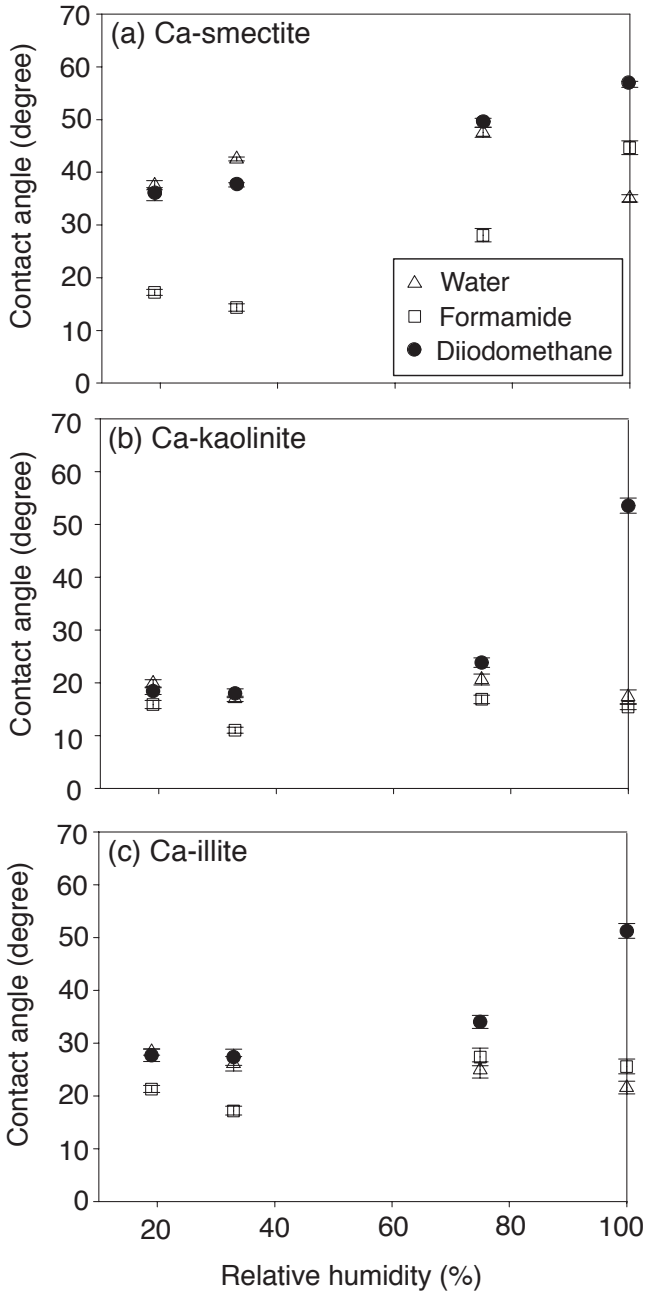

Figure 4.5: Initial contact angles (0 seconds) for aluminosilcate clays at different relative humidities. (a) Ca-smectite, (b) Ca-kaolinite, (c) Ca-illite. Errors bars indicate ± one standard deviation

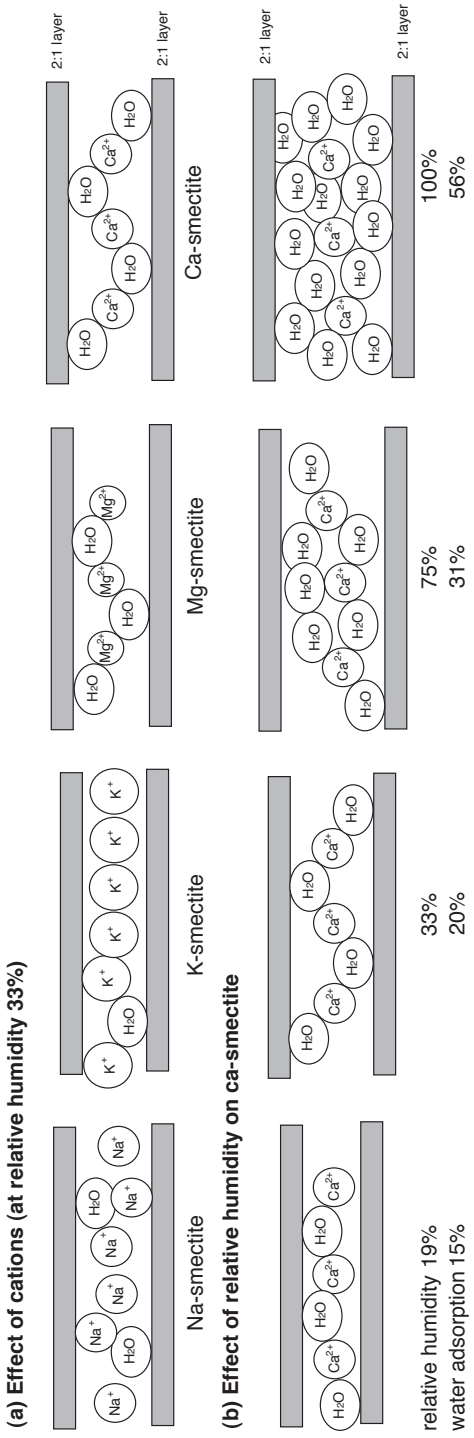

Figure 4.6: Schematic illustration of smectite structures under (a) effects of cations at relative humidity 33%, and (b) effects of relative humidities on ca-smectite.

Chapter 5

Force measurements between particles and the air-water interface: implications for particle mobilization in unsaturated porous media

5.1 Abstract

We measured maximum repulsive capillary forces between different particles (sphere, cylinder, cube, disk, sheet, natural particle) and a moving air-water interface. The particles had different size and contact angles (ranging from 14 to 121^o). Theoretical calculations using the Young-Laplace equation were used to support the experimental data. When the air-water interface moved over the particles, there were strong

---

This chapter will be submitted for publication: Shang, J., M. Flury, and Y. Deng, Force measurements between particles and the air-water interface: Implications for particle mobilization in unsaturated porous media, Water Resources Research.

capillary forces acting on the particles in direction of the moving interface. The measured maximum capillary forces were similar to those calculated by the Young-Laplace equation. The larger the contact angles and the larger the particle size, the stronger were the capillary forces. Particles with irregular shape and sharp edges experienced greater forces than smooth particles. Generalization of the results indicates that capillary forces exerted by a moving air-water interface can readily exceed attractive DLVO and gravity forces for typical subsurface particles; and a moving air-water interface is an effective process for mobilization of particles in porous media. Particles in the colloidal size range are particularly susceptible for mobilization by a moving air-water interface.

5.2 Introduction

Capillary forces act at the interface between solid, liquid, and gas phases. These forces can cause solid particles to be attracted to or repelled from each other, depending on the contact angle forming at the solid-liquid-gas interface or depending on the movement of the liquid-gas interface relative to the solids. Liquid bridges can cause strong attraction between particles [*Sur and Pak,* 2001*; Steenhuis et al.,* 2006*; Gao et al.,* 2008]; however, when the liquid bridges expand, particles may be repelled from each other. When there is a liquid film on a flat surface, strong capillary forces will pin the particles to the surface, but when the liquid film expands, the particles may be lifted off the flat surface because they are being strongly attached to the liquid-gas

interface. Whether this happens, and the order of magnitude of the forces involved, depends on surface tension, contact angles, particle densities, sizes, and shapes [*Gillies et al.,* 2005].

We hypothesize that capillary forces play an important role in colloid mobilization and transport in porous media. Under relatively dry conditions, when solid surfaces are covered with a thin waterfilm, colloid particles will be pinned to the porous media surface by capillary forces, but when water films expand, the same capillary forces can cause particles to detach and move along with moving liquid-gas interfaces.

While the general effect of liquid-gas interfaces on colloid mobilization and transport in porous media has been recognized, it is not clear what the exact mechanisms of colloid mobilization are. Colloids may be trapped in pendular liquid rings [*Wan and Tokunaga,* 1997], strained in thin liquid films [*Veerapaneni et al.,* 2000*; Saiers and Lenhart,* 2003], attached to the liquid-gas interface [*Wan et al.,* 1994], or attached at the solid-liquid-gas phase interface [*Chen and Flury,* 2005*; Crist et al.,* 2005]. Colloid mobilization can occur when liquid films expand, thereby releasing trapped colloids. It was also shown that capillary forces acting between colloids and the liquid-gas interface can mobilize colloids [*Shang et al.,* 2008a*; Sharma et al.,* 2008].

The forces acting between a particle and a liquid-gas interface can be measured by tensiometry [*Zhang et al.,* 1996*; Zhang et al.,* 1997] or atomic force microscopy [*Preuss and Butt,* 1998b*; Preuss and Butt,* 1998c*; Gillies et al.,* 2005]. In most cases, spherical particles are used for force measurements, and sphere tensiometry has even

been proposed as an alternative to du Noüy ring and Wilhelmy plate methods for measuring surface tensions and contact angles [*Gunde et al.,* 1995*; Ecke et al.,* 1999].

The capillary forces acting on a spherical particle at the liquid-gas interface can be described by the Young-Laplace equation, and numerical solutions have been developed [*Princen,* 1969*; Zhang et al.,* 1996*; Zhang et al.,* 1997*; Zhang et al.,* 1999]. For particles with sharp edges, the boundary condition for the contact angle at the sharp edges requires additional assumptions [*Hesla and Joseph,* 2004*; Singh and Joseph,* 2005], making the solution of the Young-Laplace equation more complicated. For particles with irregular shape, neither experimental measurements nor theoretical calculations are available.

The overall objective of this study was to quantify the forces acting on a solid particle when an air-water interface passes over the particle, with the goal to clarify the role of moving air-water interfaces on colloid mobilization in porous media. Specifically, we (1) quantify, both experimentally and theoretically, the forces acting on particles of different shape, and (2) discuss the implications for colloid mobilization under unsaturated flow conditions in porous media.

5.3 Theory

5.3.1 Force Balance for a Particle in Contact with a Liquid Film

Consider a particle attached to a flat surface covered by a liquid film (Figure 5.1). We assume that the density (ρ_a) of the gas phase is much smaller than that of the liquid (ρ_l) and the solid phases (ρ_s), and thus can be neglected. We use the following conventions: (1) the position of the horizontal bottom line of the particle is the reference position, (2) the position above the reference position is positive, (3) downward forces are positive and upward forces negative. The vertical components of the forces acting on the particle are as follows:

1. DLVO force (f_{DLVO}) between the particle and the surface (downward or upward depending on surface charges and solution chemistry).

2. Weight (f_w) of the particle (downward).

3. Surface tension force (f_s) (downward or upward depending on contact angle).

4. Buoyancy force (f_b) (upward).

5. Hydrostatic pressure force (f_p) due to pressure difference across the curved air-water interface.

If the sum of the above forces

$$F = f_{\mathrm{DLVO}} + f_w + f_s + f_b + f_p \tag{5.1}$$

is negative $F < 0$, then the particles will detach from the solid surface and will float at the air-water interface; if $F > 0$, the particle will be pinned to the solid surface. The sum of surface tension and hydrostatic pressure force is commonly called the capillary force, f_{cap}.

5.3.2 Sphere

The forces acting on a sphere at a liquid-gas interface have been worked out in relation to flotation and sphere tensiometry [*Princen,* 1969*; Huh and Mason,* 1974*; Huh and Mason,* 1976*; Schulze,* 1977*; Fieber and Sonntag,* 1979*; Zhang et al.,* 1996*; Singh and Joseph,* 2005]. We assume that a spherical bead with radius R is adhering to point B on a horizontal solid surface and that the contact angle of the bead is θ (Figure 5.1a). When a water film builds up on the flat solid surface, the water film forms a meniscus and a contact line (AC) around the sphere. We designate the immersion angle as ψ, the distance from the center bottom B of the bead to the horizontal air-water interface as y, and the deflecting depth of the water film as z_0 (Figure 5.1a). The vertical components of the forces exerted on the sphere are (symbols are explained in the Appendix):

$$f_w = \frac{4}{3}\pi R^3 \rho_s g \tag{5.2}$$

$$f_b = -\frac{\pi}{3} R^3 (1 - \cos\psi)^2 (2 + \cos\psi) \rho_l g \tag{5.3}$$

The surface tension force (downward if $\psi + \theta < 180^o$, upward if $\psi + \theta > 180^o$) can be calculated as [*Zhang et al.,* 1996*; Singh and Joseph,* 2005]:

$$f_s = -(2\pi R \sin\psi)\gamma \cos(270 - \psi - \theta) = (2\pi R \sin\psi)\gamma \sin(\psi + \theta) \tag{5.4}$$

The pressure force is given as [*Zhang et al.,* 1996*; Singh and Joseph,* 2005]:

$$f_p = \pi(R\sin\psi)^2 \Delta p = \pi(R\sin\psi)^2 \rho_l g z_0 \tag{5.5}$$

When the weight of the particle is tared in the air phase by a balance, and we neglect the DLVO force f_{DLVO} for the moment, Eq. (5.1) becomes

$$F = -(2\pi R\sin\psi)\gamma\sin(\psi+\theta) - \frac{\pi}{3}R^3(1-\cos\psi)^2(2+\cos\psi)\rho_l g + \pi(R\sin\psi)^2\rho_l g z_0 \tag{5.6}$$

The deflection depth z_0 is related to the height of the water film H by [*Zhang et al.,* 1996]:

$$H = z_0 - R(1 + \cos\psi) \tag{5.7}$$

5.3.3 Cylinder

For particles with sharp edges or rims such as cylinders, cubes, and prisms, the contact line moves along the smooth surfaces as the liquid film expands or shrinks, until it comes to rest at a sharp edge (Figure 5.1b). Further movement of the liquid-gas interface will not change the contact line, but rather the contact angle changes. This is in conflict with the Young equation which states that the equilibrium contact angle is constant. In this case, we can use the Gibbs extension to Young's equation [*Singh*

and Joseph, 2005]:

$$\theta_0 < \theta < 180^o - \alpha + \theta_0 \tag{5.8}$$

where α is the wedge angle and θ_0 is the equilibrium contact angle for the vertical face. The angles θ_0 and $180^o - \alpha + \theta_0$ are the limits of the contact angle θ according to the Gibbs extension, and θ can take on any value between the limits (Figure 5.1b).

We describe the forces exerted on a cylindrical particle as follows [*Princen,* 1969*; Hesla and Joseph,* 2004*; Singh and Joseph,* 2005]. We assume that a cylinder with radius R and length L is adhering to point B on a horizontal solid surface and that the contact angle between water-air interface and the vertical edge of the cylinder is θ (Figure 5.1b). When a liquid film builds up on the flat solid surface, the water film forms a meniscus around the cylinder and the contact angle is the advancing contact angle between the cylinder and the liquid. When the liquid-gas interface reaches the sharp edge of cylinder, the contact angle θ increases from θ_0 to $\theta = 180^o - \alpha + \theta_0$. The vertical components of the forces exerted on the cylinder are:

$$f_w = \pi R^2 \rho_s g L \tag{5.9}$$

$$f_b = -\pi R^2 \rho_l g L \tag{5.10}$$

If the contact angle θ at the pinned interface is larger than 90^o, the surface tension and pressure forces are given by [*Singh and Joseph,* 2005]:

$$f_s = -2\pi R \gamma \sin(\theta - 90^o) \tag{5.11}$$

$$f_p = -\rho_l g (H - L) \pi R^2 \tag{5.12}$$

When the weight of the particle is tared in the air phase with a balance and we neglect the DLVO force for the moment, Eq. (5.1) becomes

$$F = -2\pi R\gamma \sin(\theta - 90^o) - \rho_l g H \pi R^2 \tag{5.13}$$

For the calculation of the pressure force, we need to know the height of the water film H as a function of the deflection depth z_0 [*Singh and Joseph,* 2005]:

$$H = z_0 + L \tag{5.14}$$

5.3.4 Numerical Solution

We consider an unbounded liquid-gas interface in contact with an axisymmetric particle (Figure 5.1). The Young-Laplace equation describes the shape of the axi-symmetric meniscus [*Princen,* 1969*; Veerapaneni et al.,* 2000]:

$$\gamma \left\{ \frac{d^2y/dx^2}{[1 + (dy/dx)^2]^{3/2}} + \frac{dy/dx}{x[1 + (dy/dx)^2]^{1/2}} \right\} - g\rho_l y = 0 \tag{5.15}$$

together with the boundary conditions,

$$\frac{dy}{dx} = -\tan\phi_0 \quad \text{at} \quad x = x_0 \tag{5.16}$$

$$\frac{dy}{dx} = 0 \quad \text{at} \quad x \to \infty \tag{5.17}$$

For Eq. (5.15), the y-coordinate represents the vertical distance from the liquid-gas interface. By scaling with the capillary constant $c = \sqrt{\rho_l g/\gamma}$ we can define the following dimensionless variables [*Princen,* 1969*; Veerapaneni et al.,* 2000]:

$$\hat{x} = cx \quad \text{and} \quad \hat{y} = cy \tag{5.18}$$

The Young-Laplace equation can then be transformed into a system of dimensionless differential equations [*Princen,* 1969*; Veerapaneni et al.,* 2000]:

$$\frac{d\sin\phi}{d\hat{x}} + \frac{\sin\phi}{\hat{x}} - \hat{y} = 0 \tag{5.19}$$

$$\frac{d\hat{x}}{d\phi} = \frac{-\hat{x}\cos\phi}{\hat{x}\hat{y} + \sin\phi} \tag{5.20}$$

$$\frac{d\hat{y}}{d\phi} = \frac{\hat{x}\sin(\phi)}{\hat{x}\hat{y} + \sin\phi} \tag{5.21}$$

with the boundary conditions [*Princen,* 1969*; Veerapaneni et al.,* 2000]:

$$\phi = \phi_0, \quad \hat{y} = \hat{y_0} \quad \text{at} \quad \hat{x} = \hat{x}_0 \tag{5.22}$$

$$\phi = 0, \quad \hat{y} = 0 \quad \text{at} \quad \hat{x} \to \infty \tag{5.23}$$

Eqs. (5.19) to (5.23) have to be solved by numerical integration. Because the integration starts at infinity, an appropriate starting point has to be chosen. We followed the approach described by *Zhang et al.* [1996], which uses modified Bessel functions to find the starting point:

$$\sin(\phi^*) = Bk_1(\hat{x}^*) \tag{5.24}$$

$$\hat{y}^* = Bk_0(\hat{x}^*) \tag{5.25}$$

$$\hat{y}^* = \frac{k_0(\hat{x}^*)}{k_1(\hat{x}^*)}\sin(\phi^*) \tag{5.26}$$

where ($\hat{x}^*$, $\hat{z}^*$, ϕ^*) is an initial point on the liquid-gas interface.

The solution of the Young-Laplace equation has to satisfy the following conditions at the contact line with the particle:

$$\hat{x_0} = \hat{R}\sin(\psi) \quad \text{(for a sphere)} \tag{5.27}$$

$$\hat{x_0} = \hat{R} \quad \text{(for a cylinder)} \tag{5.28}$$

We solved the Young-Laplace equation (Eqs. (5.19) to (5.28)) by a 4th-order Runge-Kutta method using Mathlab (6.5.1, The MathWorks, Natick, Massachusetts).

The solution of the Young-Laplace equation in combination with Eqs. (5.6), (5.7), (5.13), (5.14) can be used to develop force-position relationships [*Huh and Mason,* 1974*; Fieber and Sonntag,* 1979*; Gunde et al.,* 1995*; Zhang et al.,* 1996]. An example of such a relation for a sphere, which is initially in the air phase and which is subsequently passing through a liquid-gas interface, is shown in Figure 5.2. The dimensionless force $\hat{F} = F/(R^3\rho_w g)$ is plotted versus relative position $\hat{H}/\hat{R}$ (dimensionless form $\hat{H} = cH$ and $\hat{R} = cR$) for contact angles $\theta = 0^o$, 60^o, 90^o, 120^o, and 180^o. The curve begins at point A, where the sphere just touches the liquid-gas interface; then the liquid-gas interface jumps to its equilibrium condition at the sphere (point B), and an attractive capillary force is recorded. As the sphere moves downward, the capillary force decreases and the buoyancy force starts to increase until at point C no net force ($\hat{F} = 0$) is exerted. When the sphere moves further down, the net force becomes negative, i.e., in upward direction, until a maximum upward force is reached at point D; further downward movement of the sphere causes the upward force to reduce again, until at point E the maximum deformation at the liquid-gas interface is reached; then the interface snaps off the sphere and the force recovers to $\hat{F} = -4\pi/3$.

For $\theta = 0^o$, the snap off occurs at point (2, $-4\pi/3$), where $\hat{F} = -4\pi/3$ is the buoyancy force. If the contact angle θ is larger than 0^o, surface tension and pressure

cause an additional upward force, as shown by the increasing maximal upward force in Figure 5.2. The larger the contact angle, the larger is the maximum upward force, and the larger is the maximum deformation of the liquid-gas interface.

In contrast to a sphere, for a cylindrical particle the liquid-gas interface pins at the sharp edge, and the contact angle θ between cylinder and interface will increase to 180^o before snap off occurs, at which point the sum of surface tension and pressure forces is maximal.

The force-distance curves were used to determine the maximum upward forces $\hat{F}_{\max}$ and the maximum immersion depths $\hat{H}_{max}$, and the results are plotted in Figure 5.3. This figure shows that (1) for a given radius $\hat{R}$, the maximum upward force and maximum deformation of the air-water interface, increase with contact angle θ; (2) for a given contact angle $\theta > 0$, the maximum upward force and maximum deformation increase when the size of the particle is reduced; (3) for a given contact angle $\theta > 0$, the slopes of the maximum force-radius curve and of the maximum immersion depth-radius curve become increasingly steeper when $\hat{R}$ is reduced. The force and immersion depth for the cylinder are independent of contact angle, and the maximum force occurs at $\theta = 180^o$.

Figure 5.3 also shows the weight of a spherical particle with density of 2.65 g cm^{-3}, typical of soils and sediment particles. The dimensionless weight for such a particle using water as the fluid for the scaling is $\hat{f} = \frac{4}{3}\pi R^3 \rho_s g/(R^3 \rho_w g) = 11.1$. When the particle size $\hat{R}$ decreases to a certain value, e.g., $\hat{R} \approx 0.5$ for $\theta = 60^o$, the upward force

equals the weight of the particle and the particle will float on the interface. When the surface of the particle becomes more hydrophilic, the size of the particle must become smaller before flotation can occur.

5.3.5 DLVO Force

If we assume the soil particles are spherical, we can use DLVO (Derjaguin-Landau-Verwey-Overbeek) theory for a sphere-plate system to calculate colloid-sediment interaction energies. The total interaction energy can be calculated as [*Gregory*, 1975; *Gregory*, 1981]:

$$\Delta G_{\text{tot}} = 64\pi\epsilon R\left(\frac{kT}{ve}\right)^2 \Upsilon_1\Upsilon_2 \exp(-\kappa h) - \frac{AR}{6h}\left[1 - \frac{5.32h}{\lambda_0}\ln\left(1 + \frac{\lambda_0}{5.32h}\right)\right] \quad (5.29)$$

where the left-hand term is the electrostatic and the right-hand term is the van der Waals interactive energy, respectively; $\Upsilon_i = \tanh(ve\psi_{0,i}/(4kT))$ where $\psi_{0,i}$ are the surface potential of the colloids and the sediments, respectively; and λ_0 is a characteristic length of 100 nm. The total DLVO or adhesive force is:

$$f_{\text{DLVO}} = \frac{\mathrm{d}}{\mathrm{d}h}(\Delta G_{\text{tot}}) \quad (5.30)$$

We assumed a separation distance of h = 0.3 nm [*Elimelech et al.*, 1995; *Sharma et al.*, 2008] to calculate the values of the DLVO forces.

5.4 Materials and Methods

5.4.1 Particles used for Force Measurements

We used particles of well-defined geometry as well as soil particles for the force measurements. The particles of well-defined geometry consisted of spheres, cylinders, disks, and sheets (Table 5.1). These particles were all purchased from McMaster-Carr (Santa Fe Springs, CA), cleaned by sequential immersion in acetone (once), ethanol (once), and deionized water (>3 times). The dimensions of the particles were measured with a micrometer caliper with an error of ±0.01 mm. The density of the each type of material was calculated from the average weight and average volume.

The natural subsurface particles were obtained from the sediments of the Hanford Environmental Restoration Disposal Facility (ERDF), located 8 miles from the Columbia River between the 200 East and 200 West Areas of the Hanford Site (south-central Washington State, USA). Five different types of particles (3 particles each) with size between 1 mm and 5 mm were selected (Table 5.2, Figure 5.4). Particles were identified optically and microscopically. The particles were cleaned by sequential immersion in ethanol for 24 hours, and deionized water for 24 hours, followed by air-drying.

The particles were mounted onto U-shaped hooks, made of steel wire (Figure 5.5). Two different diameter wires were used, a 0.5-mm wire was used for the three smallest spheres, the regular-shape PTFE objects, and a 0.78-mm wire was used for the two

largest spheres and the regular-shape steel objects. The wires were cut to about 7-cm long segments, and bent to hooks. The tips of the hooks were flattened with a file to ensure enough contact area with spheres and regular-shape objects. The hooks were cleaned in the same manner as the particles. The glass and steel particles were then glued onto the hooks using Instant Krazy Glue (Elmer's Products, Inc., Columbus, Ohio). As the PTFE particles were difficult to glue to the hooks, a hole was drilled into each PTFE object with a microdrill (Dremel Moto-Tool model 395, Dremel, Racine, WI). A small amount of glue was applied into the hole, and the tip of the hook was inserted into the hole. The natural subsurface particles were glued onto the tip of the hook in the middle of one side.

5.4.2 Contact Angle Measurement

We determined the air-water-solid advancing contact angle on the objects as follows. A bead with 4 or 4.76-mm particle size was mounted on a microscopy slide using a double-sided tape. A micro-syringe with a steel needle (outer diameter 0.5 mm) was used to deposit a drop of water next to the bead, and the contact angle was measured with a digital goniometer (Drop Shape Analysis System, DSA100, Krüss GmbH, Hamburg, Germany).

5.4.3 Force-Position Curve Measurements

We measured the forces between the particles and the air-water interface by using a tensiometer (Process Tensiometer, K100, Krüss GmbH, Hamburg, Germany). The hook with an attached particle was mounted onto the microbalance of the tensiometer. The air inside the sample chamber of the tensiometer was saturated with moisture by keeping wet paper towels inside the chamber. A cup with 65-mm inner diameter was used to hold the water in which the particle was immersed. Nano-pure water with an EC of 0.5 μS m^{-1} was used. Temperature of the water was controlled by a circulating water bath to be 20$\pm$0.5°C.

At the beginning of the measurements, the hook and the particle were in the air phase, and the tensiometer balance was tared to zero. The particle was then successively immersed into the water by raising the water cup, whose velocity was controlled by the tensiometer. The force on the object was recorded in 0.05-mm position increments as the particle passed through the air-water interface. When the particle was completely immersed in the water, the water cup was lowered at the same velocity until the particle was in its original position above the air-water interface. This sequence was repeated five times for each particle. The data were then used to construct force-position curves.

As the force measured is dependent of the surface tension of the fluid, we verified the surface tension of the water in the cup using the Wilhelmy plate method. The surface tensions of water before and after immersion of the objects did not significantly change.

Average surface tension was 72.4±0.4 mN m^{-1} before each force-position measurement cycle, and 72.0±0.3 mN m^{-1} after the measurements.

An initial test was performed to assess the effect of immersion velocity on the force measurements. For this test, we used only one size (4.8 or 5.0 mm) of each sphere type. We determined force-position curves at interface velocities ranging from 0.25 to 10 mm min^{-1}. Standard errors of the force for different velocities were within 4%, suggesting that the air-water interface reached equilibrium with the bead at speeds up to at least 10 mm min^{-1}. We selected an immersion speed of 1.0 mm min^{-1} for the experimental measurements.

5.5 Results and Discussion

5.5.1 Force-position Curves

Figure 5.6 shows examples of measured force curves. These curves can be categorized into the following segments: (a) before the hook touches the air-water interface, the weight of the sphere and hook was tared to zero, no net force is recorded; (b) when the bottom of the hook touches the water, a downward attractive (positive) force, due to the capillary force on the hook itself, is recorded; (c) when the hook is further immersed into water, the attractive force reduces, and when the air-water interface bends downward, capillary and buoyancy forces on the hook cause an upward lifting (negative) force; (d) the upward force reaches its maximum just before the air-water

interface detaches from the horizontal part of the hook and the force recovers to nearly zero; (e) once the particle touches the air-water interface, a maximum downward attractive force is recorded; (f) as the particle continues to be immersed into the water, the surface tension and buoyancy forces cause the force to become smaller until it becomes an upward lifting (negative) force, the force reaches a minimum and then increases slightly; (g) when the maximum deformation of the air-water interface is reached, the deformed air-water interface snaps back to its original flat surface; and (h) the surface tension force on the wire and the buoyancy forces on the object and wire contribute to the upward force thereafter; the slight slope observed as the particle is continued to be immersed corresponds to the increase of the buoyancy force.

During emersion the forces are downward (positive) throughout the emersion process. The hysteresis observed between immersion and emersion is due to contact angle hysteresis (advancing vs receding). In addition, the non-symmetry due to the presence of the hook also contributes to hysteresis.

The measured force-position curves are, for a large part, affected by the interactions of the hook with the air-water interface. The relevant sections for the particle interactions with the air-water interface are sections (e), (f), (g), and (h). We are particularly interested in the magnitude of the upward lifting forces during particle immersion, and the maximum upward force just before snap off of the particle from the air-water interface. The maximum upward capillary force $f_{cap,max}$ can be determined from the force-position curves as the difference Δf between the maximum upward

force before snap off and the force just after snap off between (g) and (h) (Figure 5.6). As there is only an insignificant movement of the horizontal section of the air-water interface with respect to the particle during snap off, the measured force $f_{cap,max}$ is not affected by buoyancy differences.

Figure 5.6 also shows that for all the particles investigated in our study, we measured upward repulsion forces, i.e., the air-water interface caused an upward force when the interface moved over the particles. The tensiometer measurements were well suited to quantify the forces, even for the irregular shaped sediment particles.

5.5.2 Maximum Capillary Force

For spherical particles, the maximum capillary force increases with increasing radius (Figure 5.7a). The measured maximum capillary force increased with radius and hydrophobicity of the beads (Figure 5.7a). Experimental data generally agreed well with calculated values. For PTFE, the relative errors were less than 5% and for steel less than 9%. For glass, the errors were larger (up to 43% for the smallest sphere), which was likely caused by the small forces measured. In dimensionless form (Figure 5.7a), the maximum upward surface tension and hydrostatic force increase when the particle size is reduced, and the slopes of the curve become increasingly steeper as the particle size becomes smaller.

Figure 5.8 shows the theoretical maximum capillary forces for spheres and cylinders with different contact angles. The theoretical maximum capillary forces for the

cylinders are always larger than those for spheres with the same diameter and are independent of contact angle. The independence of the force on contact angle is because snap off occurs at an effective contact angle of 180^o. This causes particles with sharp edges to have larger negative capillary forces than particles with smooth edges.

The experimental and theoretical forces for the steel and PTFE particles with sharp edges are summarized in Table 5.3. The experimental data agree well with theoretical calculations. The data confirm the independence of the maximum capillary force on the equilibrium contact angle. The maximum force occurs indeed when the contact angle $\theta = 180^o$. The data also show that the maximum capillary force was little affected by density and height of the particles.

The sediment particles with irregular shapes have sharp edges on the surface, which will increase the maximum capillary forces causing the particle to float or detach from a solid surface (Figure 5.2). Table 5.2 shows that the sediment particles had negative capillary forces as the air-water interface passed over the particles. We cannot calculate the capillary forces for the natural particles theoretically, but we can approximate the maximum capillary force by using a sphere and cylinder equivalent, i.e., a sphere and cylinder having a diameter equal to the maximum length of the natural particle. The maximum repulsive forces measured for the sediment particles are larger than theoretical values for equivalent spheres, but smaller than those of a cylinder (Table 5.2).

5.5.3 Force Balance Considerations

If the particle is in contact with a solid-liquid interface, the particle experiences DLVO forces, which can be calculated with Eq. (5.30). We are interested in colloid detachment and mobilization in natural subsurface media, so we consider the case of natural subsurface particles here. For illustrative purposes, we are using DLVO parameters as used in *Shang et al.* [2008a]: particle radius = 250 nm, electrophoretic mobility = -3.18 ± 0.07 (μm s^{-1})/(V cm^{-1}), ζ potential = $-$ 40.1 $\pm$ 0.9 mV, water contact angle = 25.9 $\pm$ 2.5 degree. Sediments and particles are assumed to have the same properties. The particle size of sediments is 797 μm, and sediments are assumed as the flat plates compared to particle radius 0.25 μm.

To illustrate the importance of the DLVO forces, we plotted the different forces as a function of ζ potential for a particle with radius 250 nm and contact angle $\theta = 25.9^o$ (Figure 5.9). Figure 5.9a shows that for colloids with radius 250 nm and contact angle $\theta = 25.9^o$, the attractive DLVO force is always smaller than the maximum replusive capillary force, even though DLVO force increases when ζ potential increases from -100 to 100 mV. The total attractive and repulsive forces are shown in Figure 5.9b, which indicates that repulsive forces are dominant. No matter what the surface charge of particles, the DLVO forces at the separation distance 0.3 nm are smaller than the repulsive capillary force.

The different forces acting on a spherical particle with contact angle $\theta = 25.9^o$ as a function of particle size are shown in Figure 5.10. Figure 5.10a shows that (1)

the maximum capillary force and the DLVO forces are dominant in the system when particle radius is less than about 0.1 mm; (2) the buoyancy force and weight are more and more important when particle radius is larger than about 0.1 mm. The net forces (Figure 5.10b) show that the maximum repulsive forces are dominating up to a particle size of 0.48 mm, after which attractive forces start to dominate. This means that for our system, particles less than 0.48 mm can be lifted off the sediment surfaces by the maximum upward force (the sum of maximum capillary and buoyancy force).

To show the effects of contact angle, the different forces are plotted as a function of contact angle for a particle with radius 250 nm (Figure 5.11). Figure 5.11a shows that (1) the buoyancy and weight forces are small compared to other two forces; (2) for colloids with radius 250 nm, the maximum replusive capillary force and the attractive DLVO force are the dominant forces to determine colloid retention and release. Figure 5.11b shows that for contact angles less than 15^o, attractive forces are dominant, above this contact angle repulsive forces dominate. This suggests that the repulsive forces are dominent for a large range of particle sizes and contact angles.

5.6 Implications for Colloid Mobilization in the Vadose Zone

Our experiments demonstrate that capillary forces acting at the air-water interface in porous media can cause strong repulsion of particles from the stationary surfaces

when water films expand or move through the porous medium. No matter whether the surface charge of particles is negative or positive, the particle size large or small, the maximum replusive capillary force is larger than the DLVO force. For particles in the size range of fine sands, silt, and clay, the repulsive force exceeds attractive DLVO and gravity forces. The capillary force is therefore a dominant force in colloid mobilization in an unsaturated environment. The repulsive capillary force becomes more dominant the smaller the particle, i.e., particles in the colloidal size fraction (diameter < 2 μm) will be most affected by the repulsive capillary force. In addition, a rough and irregular surface shape causes the capillary force to increase as compared to a smooth, spherical shape, making natural particles even more prone to detachment and mobilization due to moving air-water interfaces.

5.7 Tables and Figures

Table 5.1: Characteristics of spherical beads and sharp-edged particles.

Shape	Material	Diameter/length (mm)	Sphericity[a]/height (mm)	Density (g cm^{-3})	Contact angle (degree)
Sphere	Glass	2.37[b], 3.16[b], 3.95[b], 4.76, 6.34	<0.01	2.46	64 ± 1
Sphere	Steel	1.00[b], 2.00, 3.00, 4.00, 5.00	<0.01	7.85	83 ± 1
Sphere	PTFE	2.37[b], 3.17[b], 3.97[b], 4.76[b], 6.35	<0.01	2.16	121 ± 3
Cylinder	Steel	4.76	4.76	7.85	83 ± 1
Cylinder	PTFE	4.76	4.76	2.16	121 ± 3
Cube	Steel	4.76	4.76	7.85	83 ± 1
Cube	PTFE	4.76	4.76	2.16	121 ± 3
Disk	Steel	4.76	2.00	7.85	83 ± 1
Disk	PTFE	4.76	2.00	2.16	121 ± 3
Sheet	Steel	4.76	2.00	7.85	83 ± 1
Sheet	PTFE	4.76	2.00	2.16	121 ± 3

[a] Difference between measured maximum and minimum diameters.

[b] Particles can be floated by pure water.

Glass, Heat-resistant borosilicate.

Steel, Bearing-quality aircraft-grade E52100 alloy, chrome-coated.

PTFE, Virgin electrical grade fluoropolymer.

Table 5.2: Characteristics and maximum capillary force of natural Hanford sediments with irregular shape.

Sediments	Number	Max length	Max width	Max height	Contact angle	Maximum Capillary Force		
						Experimental	Theoretical[a]	
							Sphere	Cylinder
		(mm)	(mm)	(mm)	(degree)	(μN)	(μN)	(μN)
Basalt	1	1.57	1.50	1.12	23 ± 3	−220 ± 15	−14	−385
	2	2.99	1.97	1.04	23 ± 3	−370 ± 20	−27	−829
	3	3.37	2.60	1.32	23 ± 3	−247 ± 11	−31	−965
Quartz	1	2.11	1.91	1.08	37 ± 3	−321 ± 17	−49	−542
	2	3.23	2.80	1.24	37 ± 3	−254 ± 12	−76	−914
	3	3.86	3.23	1.55	37 ± 3	−523 ± 20	−92	−1153
Granite	1	1.97	1.71	1.11	22 ± 3	−194 ± 15	−16	−501
	2	4.32	3.34	1.29	22 ± 3	−197 ± 19	−37	−1340
	3	3.42	2.92	1.04	22 ± 3	−265 ± 13	−29	−984
Biotite	1	1.49	1.58	1.20	14 ± 5	−103 ± 9	−5	−366
	2	2.45	2.45	0.20	14 ± 5	−427 ± 17	−8	−649
	3	3.13	2.75	0.11	14 ± 5	−496 ± 27	−11	−878
Calcite	1	3.1	2.68	1.77	14 ± 3	−13 ± 2	−11	−867
	2	3.85	3.12	1.78	14 ± 3	−95 ± 7	−13	−1148
	3	3.28	2.92	1.05	14 ± 3	−94 ± 38	−11	−932

± denotes one standard deviation.

[a] theoretical calculations of maximum capillary forces for spheres and cylinders are based on maximum lengths of Hanford sediments, and are therefore maximum expected forces.

Table 5.3: Maximum capillary forces (upward forces) for regular-shaped particles with sharp edges.

Material	Shape	Size	Contact Angle	Maximum Capillary Force	
				Experimental	Theoretical
		(mm × mm)	(degree)	(μN)	(μN)
Steel	cylinder	4.76 × 4.76	83 ± 1	−1468 ± 17	−1532
	cube	4.76 × 4.76	83 ± 1	−1608 ± 10	−1532
	disk	4.76 × 2.00	83 ± 1	−1497 ± 6	−1532
	sheet	4.76 × 2.00	83 ± 1	−1554 ± 26	−1532
PTFE	cylinder	4.76 × 4.76	121 ± 3	−1466 ± 14	−1532
	cube	4.76 × 4.76	121 ± 3	−1548 ± 8	−1532
	disk	4.76 × 2.00	121 ± 3	−1500 ± 7	−1532
	sheet	4.76 × 2.00	121 ± 3	−1535 ± 7	−1532

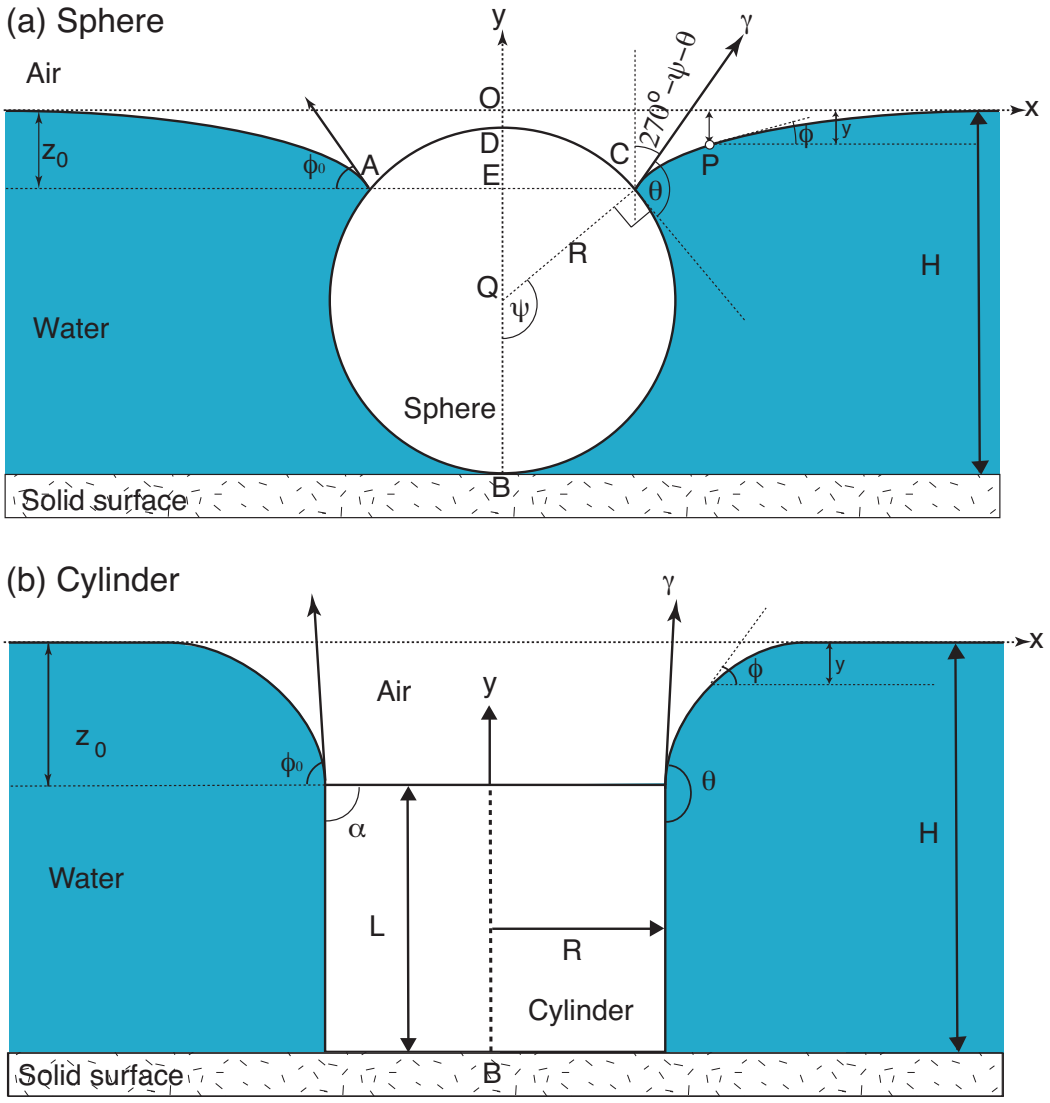

Figure 5.1: (a) A sphere and (b) cylinder adhering to a horizontal solid surface in contact with a water film of height H.

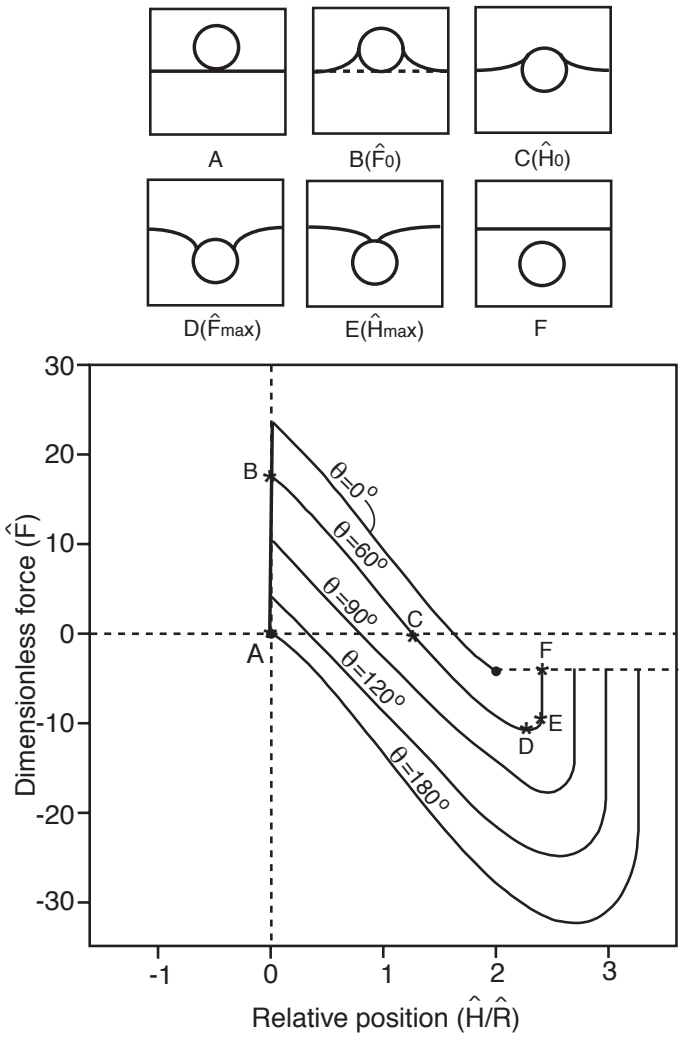

Figure 5.2: Examples of theoretical force-position curves for a sphere with $\hat{R} = 0.5$. Contact angles of water on the spheres are noted in the figure. The weight of the sphere in air is tared to zero. Letters indicate geometrical configurations and respective positions in the force-position curves shown for $\theta = 60^o$.

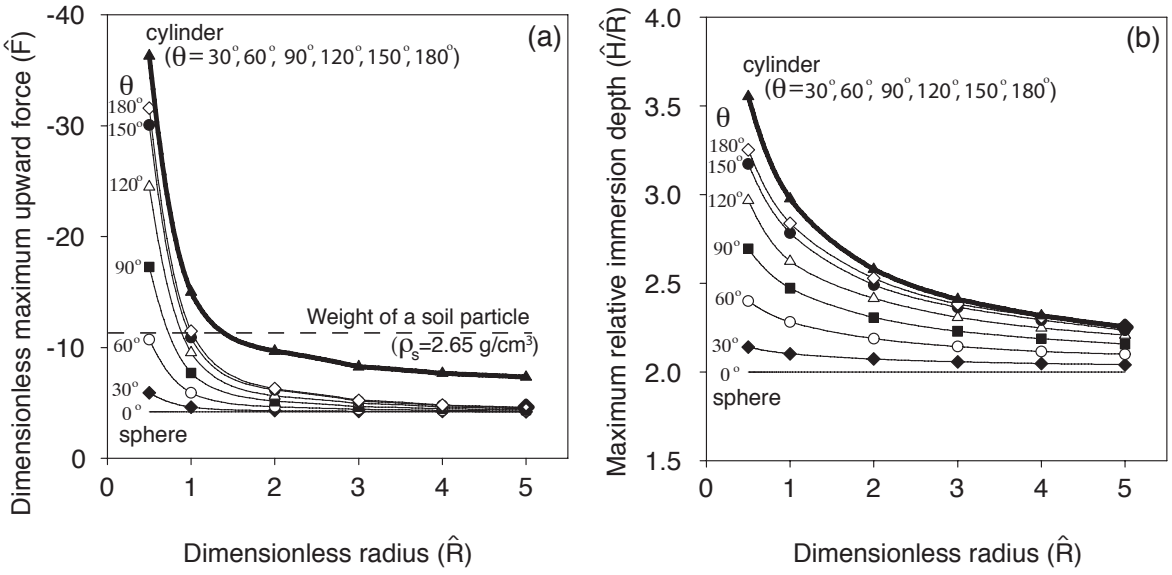

Figure 5.3: (a) Theoretical maximum upward force (dimensionless) and (b) theoretical maximum immersion depth (dimensionless) of spheres and cylindrical cylinders ($\hat{L} = 2\hat{R}$) with different radius and contact angle θ. Also shown is the dimensionless weight of a typical spherical soil particle with density $\rho_s = 2.65$ g cm^{-3}. The thick line is for the cylinder.

Figure 5.4: Five different natural Hanford sediment particles (basalt, quartz, granite, biotite, and calcite) with irregular shapes.

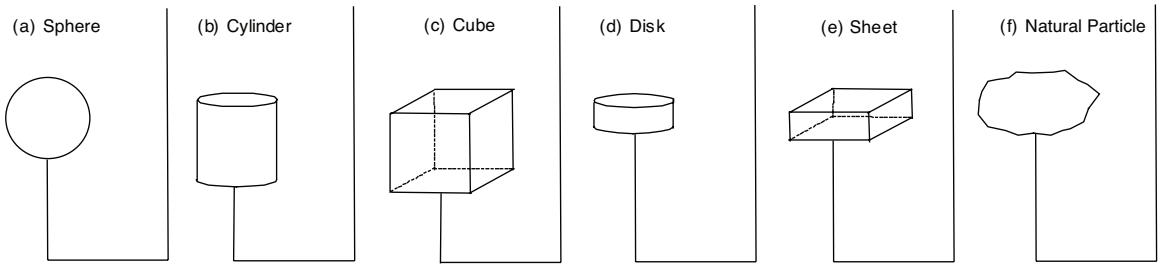

Figure 5.5: Different shape particles (sphere, cylinder, cube, disk, sheet, and natural particle) with hooks.

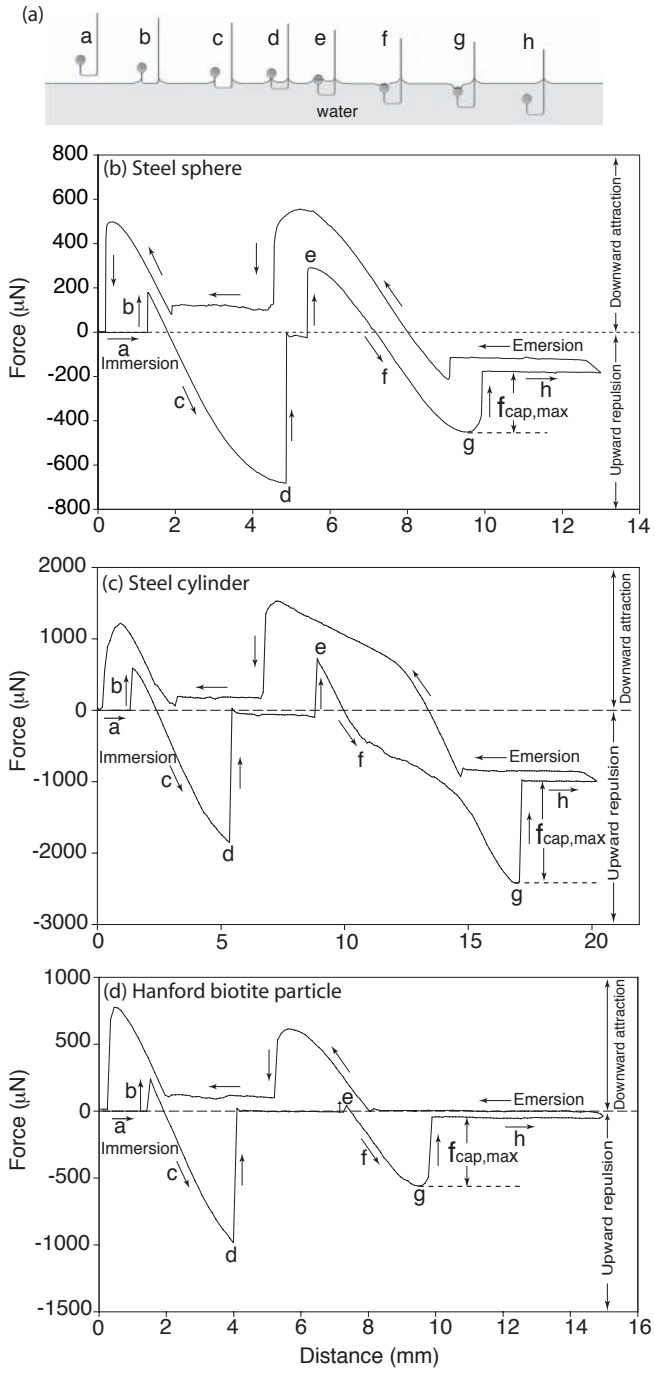

Figure 5.6: (a) Schematic of immersion of a particle into water, (b) corresponding measured force-position curve for a 3-mm diameter steel sphere, (c) a 4.76 mm diameter and 4.76 mm height steel cylinder, and (d) a Hanford biotite particle. $f_{cap,max}$: maximum upward capillary force.

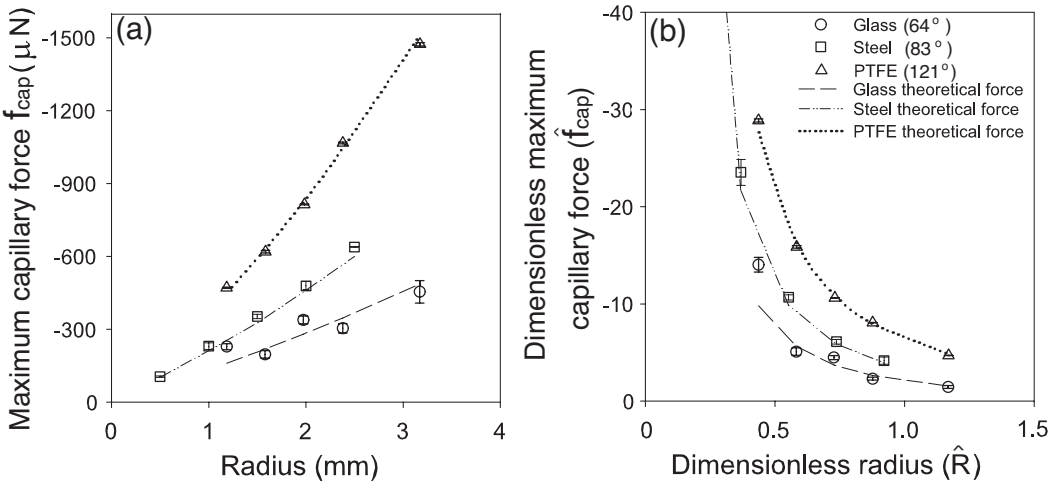

Figure 5.7: Measured (open symbols) and theoretical (small symbols) maximum capillary force of spherical beads as a function of sphere radius: (a) dimensional and (b) dimensionless form. Error bars represent ± one standard deviation.

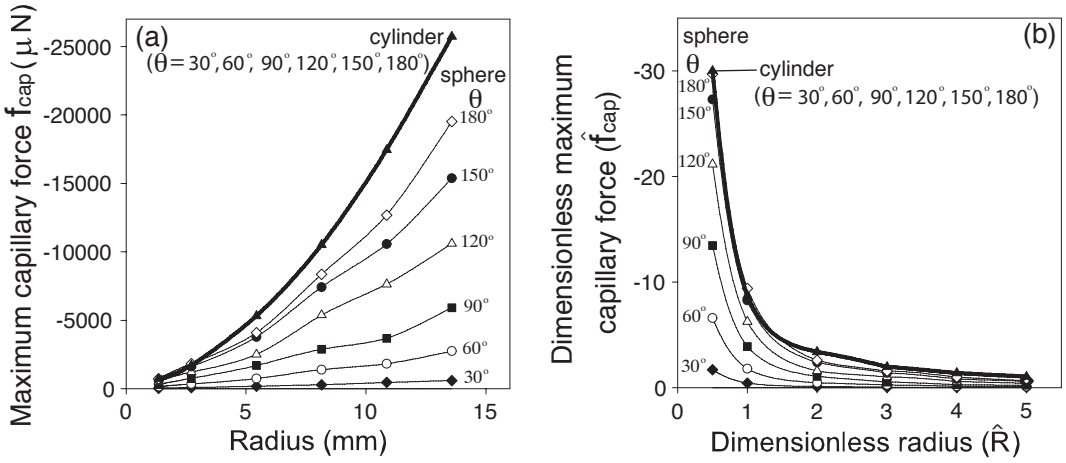

Figure 5.8: Theoretical maximum surface tension and hydrostatic force on a sphere and cylindrical cylinder ($L = 2R$) for different radii and contact angles: (a) dimensional and (b) dimensionless form. The thick line is for the cylinder.

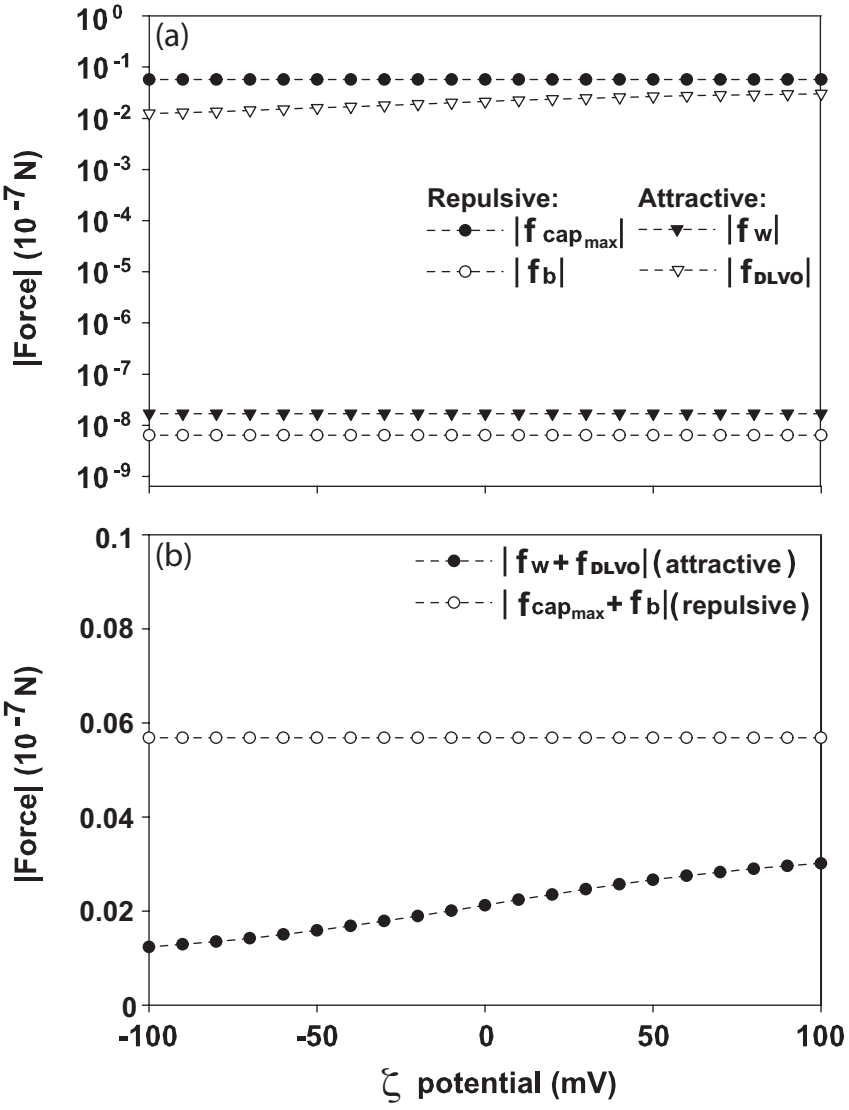

Figure 5.9: (a) Attractive and repulsive forces, and (b) net attractive and net maximum repulsive forces acting on spherical particle in contact with an air-water interface as a function of ζ potential for a fixed particle radius (250 nm), a contact angle (25.9^o), and a density of 2.65 g cm^{-3}. f_w: weight, f_{DLVO}: the sum of van der Waals force and electrostatic force, $f_{cap,max}$: maximum upward capillary force, f_b: buoyancy force. ζ potential of sediments is fixed to -40.1 mV.

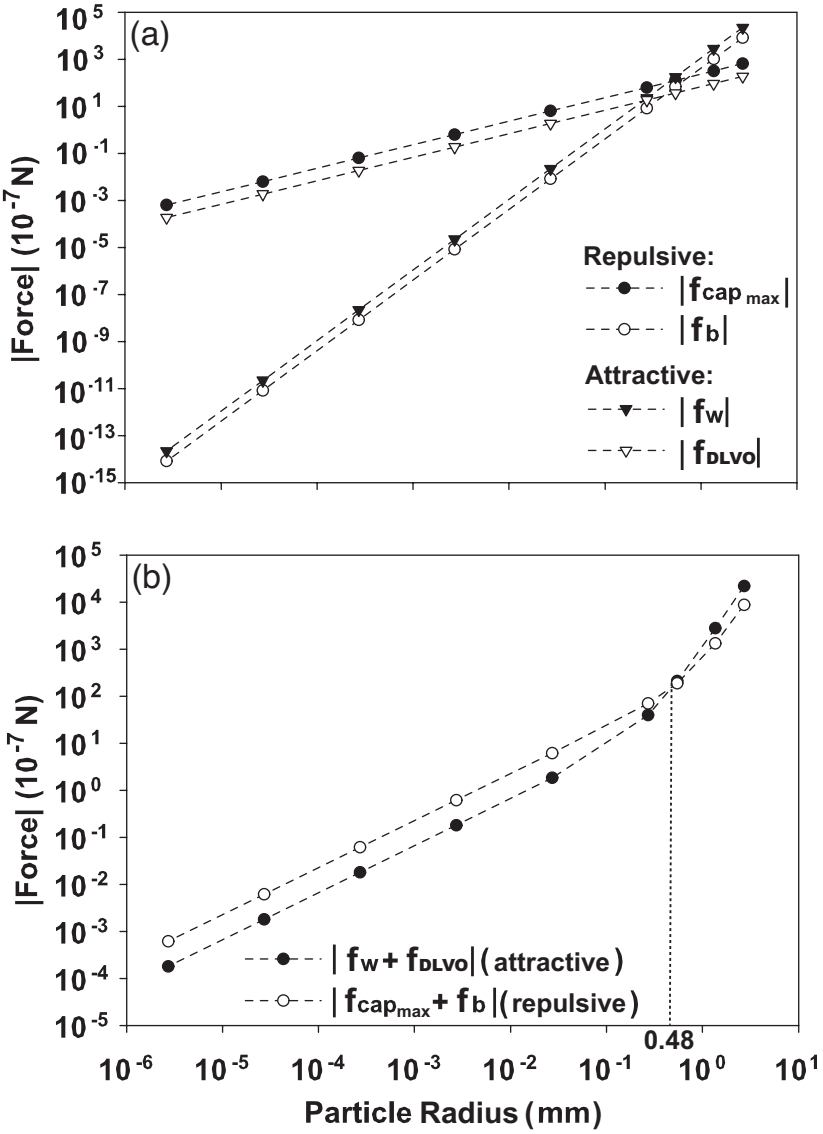

Figure 5.10: (a) Attractive and repulsive forces, and (b) net attractive and net maximum repulsive forces acting on spherical particle with ζ potential -40.1 mV in contact with an air-water interface as a function of particle radius for a fixed contact angle (25.9^o).

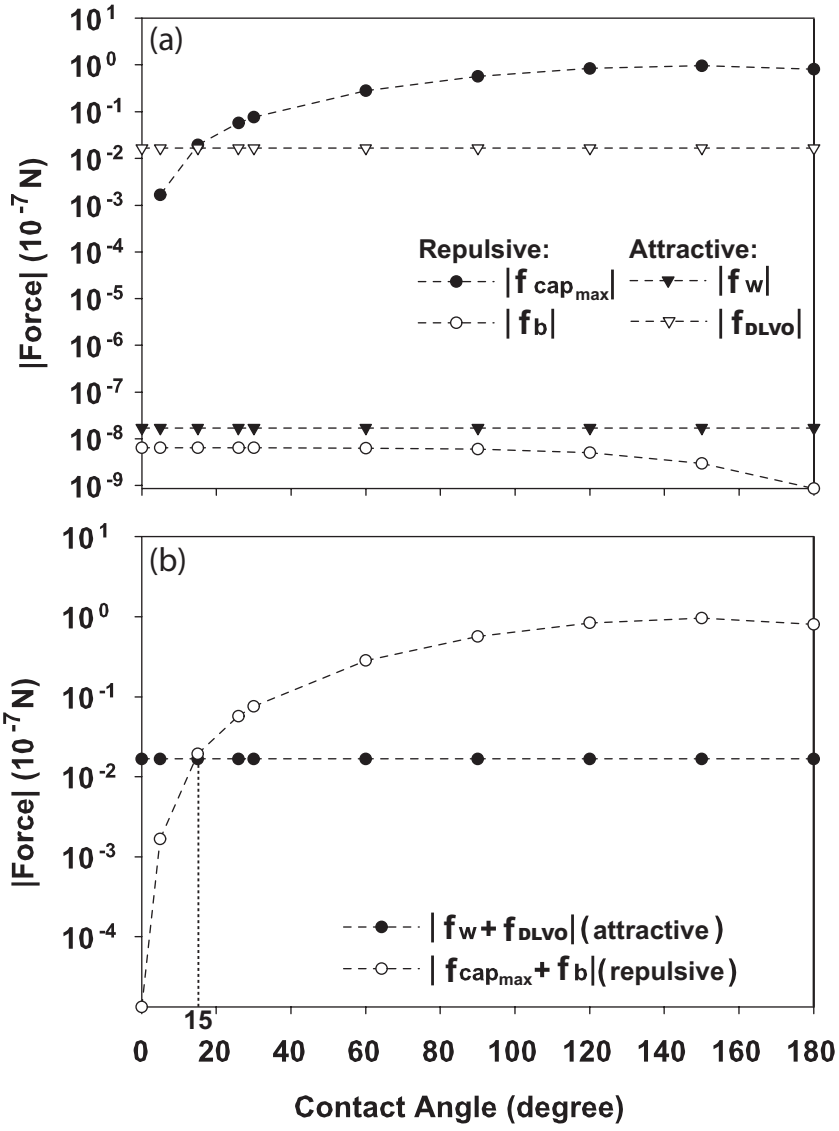

Figure 5.11: (a) Attractive and repulsive forces, and (b) net attractive and net maximum repulsive forces acting on spherical particle with ζ potential -40.1 mV in contact with an air-water interface as a function of contact angle for a fixed particle radius (250 nm).

5.8 Appendices

5.8.1 Appendix A: List of Symbols

Latin Symbols

A	Hamaker constant [M L^2 T^{-2}]
B	integration constant [−]
c	capillary constant $c = \sqrt{\rho_l g/\gamma}$ [L^{-1}]
e	electron charge (1.6×10^{-19} C) [I T]
f_{DLVO}	the sum of van der Waals force and electrostatic force between the particle and the surface (downward or upward depending on surface charges and solution chemistry) [M L T^{-2}]
f_b	buoyancy force (upward) [M L T^{-2}]
f_p	pressure force due to pressure difference across the curved air-water interface [M L T^{-2}]
f_{cap}	sum of surface tension and hydrostatic pressure force [M L T^{-2}]
$f_{cap,max}$	maximum upward capillary force [M L T^{-2}]
f_s	surface tension force (downward or upward depending on contact angle) [M L T^{-2}]
f_w	weight of the particle (downward) [M L T^{-2}]
$\hat{f}$	dimensionless force [−]
$\hat{f}_{cap}$	the sum of dimensionless surface tension and dimensionless hydrostatic pressure force [−]
F	the sum of f_{DLVO}, f_w, f_s, f_b, and f_p [M L T^{-2}]
$\hat{F}$	dimensionless sum forces of f_{DLVO}, f_w, f_s, f_b, and f_p [−]

$\hat{F}_0$ dimensionless force when $\hat{H} = 0$ [−]

$\hat{F}_{max}$ dimensionless maximum upward force [−]

g gravitational acceleration [L T^{-2}]

h separation distance [L]

H height of water film [L]

$\hat{H}$ dimensionless height of water film below reference line [−]

$\hat{H}_0$ dimensionless height when $\hat{F} = 0$ [−]

$\hat{H}_{max}$ dimensionless maximum height of water film above reference line [−]

k Boltzmann constant (1.38×10^{-23} J K^{-1}) [M L^2 T^{-2} T^{-1}]

$k_0(x)$ modified Bessel function of the second kind of order zero [−]

$k_1(x)$ modified Bessel function of the second kind of order one [−]

L height of cylinder [L]

R radius of sphere or cylinder [L]

$\hat{R}$ dimensionless radius of sphere or cylinder [−]

T absolute temperature [T]

v ion valence [−]

x horizontal distance measured from the axis of symmetry [L]

$\hat{x}$ dimensionless horizontal distance measured from the axis of symmetry [−]

$\hat{x}_0$ dimensionless horizontal distance measured from the axis of symmetry to where the liquid−air interface meets the particle [−]

$\hat{x}^*$ dimensionless horizontal distance of the initial point on the liquid-gas interface [−]

y vertical distance measured upward/downward from the interface [L]

$\hat{y}^*$ dimensionless vertical distance of the initial point on the liquid-gas interface [−]

$\hat{y}$ dimensionless vertical distance measured upward/downward from the interface [−]

z_0 deflection depth related to the length of the water film [L]

$\hat{z_0}$ dimensionless vertical distance measured upward/downward from the interface to where the liquid−air interface meets the particle [−]

Greek Symbols

α	wedge angle [degree]
γ	liquid surface tension [M T^{-2}]
ΔG_{tot}	total interaction energy [M L^2 T^{-2}]
Δp	pressure difference [M L^{-1} T^{-2}]
ϵ	permittivity of the liquid [I^2 T^4 L^{-3} M^{-1}]
Υ_i	surface potential of the colloids and the sediments or the liquid-gas interface [M T^{-3} L^2 I^{-1}]
ρ_a	density of air phase [M L^{-3}]
ρ_l	density of liquid phase [M L^{-3}]
ρ_s	density of solid phase [M L^{-3}]
ρ_w	density of water [M L^{-3}]
θ	water contact angle of the particle [degree]
θ_0	equilibrium contact angle for the vertical face of the particle with sharp edges [degree]
ϕ	angular inclination of the interface to the horizontal [degree]
ϕ_o	angular inclination of the interface to the horizontal line when the interface meets the particle surface [degree]
ϕ^*	dimensionless angle of the initial point on the liquid-gas interface [−]
κ	Debye-Hückel reciprocal length [L^{-1}]
λ_0	characteristic length of system [L]
ψ	filling angle between the center of the colloidal sphere and the water-colloid contact line [degree]

5.8.2 Appendix B: An example of the complete solution of the Young-Laplace equation for a sphere

An example of the complete solution of the Young-Laplace equation for a sphere is shown in Figure 5.12, where the dimensionless force $\hat{F} = F/(R^3\rho_w g)$ is plotted versus relative position $\hat{H}/\hat{R}$ (dimensionless form $\hat{H} = cH$ and $\hat{R} = cR$) for contact angles $\theta = 0^o$, 60^o, 90^o, 120^o, and 180^o. The curve begins at the point A, where the sphere just touches the liquid-gas interface; then it goes through the maximum height point position B ($\hat{H}_{\max}$), below which the interface begin to pull the sphere into the liquid phase; the maximum downward force point C ($\hat{F}_{\max}$); the point D ($\hat{H} = 0$); the point E ($\hat{F} = 0$) above which the force is downward and below which the force is upward; the maximum upward force is reached at point F; the maximum deformation of liquid-gas interface is at point G, and at point H (2,$-4\pi/3$) the sphere is completely immersed in the liquid phase.

sectionAppendix C: Force measurement schematic − tensiometer A tensiometer (Process Tensiometer, K100, Krüss GmbH) was used to monitor and measure the forces between a particle and the liquid-gas interface when the particle passed through the interface (Figure 5.13). The weight of the particle is tared in the air phase by the balance of the tensiometer before the force measurement.

5.8.3 Appendix D: Figures of the particles with the hooks

Figure 5.14 and 5.15 show the spheres and natural particles attached to the hooks.

5.8.4 Appendix E: Figures of a sphere with different speeds

To assess the effect of immersion velocity on the force measurements, we used one size (4.8 or 5.0 mm) of each sphere type. The force-position curves at interface velocities ranging from 0.25 to 10 mm min^{-1} are shown in Figure 5.16. Therefore, no significant effect of the velocity on force-position curves was excepted.

5.8.5 Appendix F: Bead flotation experiment

To demonstrate that the air-water interface can detach particles from a surface, we used 0.8 and 2 mm diameter glass beads (VWR, catalogue number 26396-506). One batch of the beads was coated with paraffin to make the beads hydrophobic. For the coating, a few pieces of paraffin were placed on a glass microscopy slide and heated with a hot plate, until the paraffin melted. Then, the glass beads were rolled over the melted paraffin film by using sharp-tipped tweezers. The heating was maintained for about 10 minutes to thin the coating, until most of the paraffin melted off the microscopy slide. The slides and the coated beads were then cooled at room temperature.

When a bead sits on a surface (e.g., the bottom of the plastic cuvette in Figure 5.17), the weight of the bead and the net DLVO force keep the bead on the surface. To lift the bead, which is equivalent to detaching a particle from its adhesion surface, the sum of upward surface tension, hydrostatic force, and buoyancy force must be greater than the weight of the bead and the net DLVO force. When a 2-mm-diameter, hydrophilic glass bead (contact angle $\theta = 64^o$) was used in the experiment,

the bead could not be lifted by the water-air interface. When the same sized glass bead was coated with a thin layer of paraffin ($\theta = 109^o$), the bead could be lifted (Figure 5.17a, and supporting video file). When the size of the glass bead was reduced (0.8 mm), the uncoated hydrophilic glass bead could be lifted up with the rising water table (Figure 5.17b, and supporting video file).

5.8.6 Appendix G: Sediment flotation experiment

Hanford sediment particles, cleaned by acetone (once), ethanol (once), and deionized water (>3 times), were dry-sieved through 2 mm, 1 mm, 0.5 mm, 0.25 mm, 0.106 mm, and 0.053 mm diameter screens to separate the sediments into 5 size groups: 0.053 −0.106 mm, 0.106−0.25 mm, 0.25−0.5 mm, 0.5−1 mm, 1−2 mm (Figure 5.18). Flotation experiments were conducted with a 5 cm diameter column vertically oriented, and the bottom of the column equipped with a single-layer nylon membrane (450 mesh, 32 μm pore opening, Gilson Company, Lewis Center, OH). We weighed out 0.05, 0.1, 0.2, 1, 2 g of materials respectively, for the 0.053−0.106 mm, 0.106−0.25 mm, 0.25−0.5 mm, 0.5−1 mm, 1−2 mm groups. The sediment particles were spread randomly onto the nylon membrane. The column was then placed above the water surface in a beaker. The water level was increased at a speed of 1.0 mm min^{-1}. The sediment material floating at the air-water interface and most of the liquid in the column were taken out from the column using a spoon. Then, the collected sediments were dried, and the total dry mass measured gravimetrically.

A considerable fraction of the sediments could be floated at the air-water interface. The percentage of particles floating at the interface increased with decreasing particle size (Figure 5.19). More than 60% per weight of particles less than 0.1 mm could be floated at the air-water interface. Our calculations show that the magnitude of different forces is as a function of particle size, and that the capillary force becomes more and more important, the smaller the particles are (Figure 5.10). Figure 5.19 clearly indicates that the detachment force is more dominant because of the capillary force when the particle size is smaller.

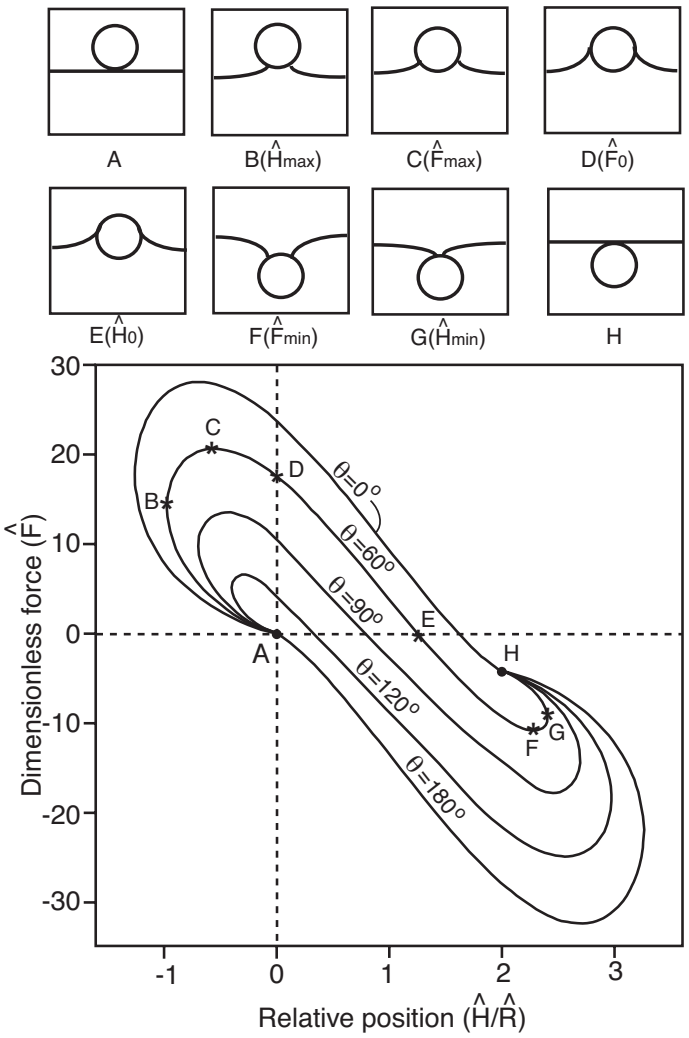

Figure 5.12: Examples of complete theoretical force-position curves for a sphere with $\hat{R} = 0.5$. Contact angles of water on the spheres are noted in the figure. The weight of the sphere in air is tared to zero. Letters indicate geometrical configurations and respective positions in the force-position curves.

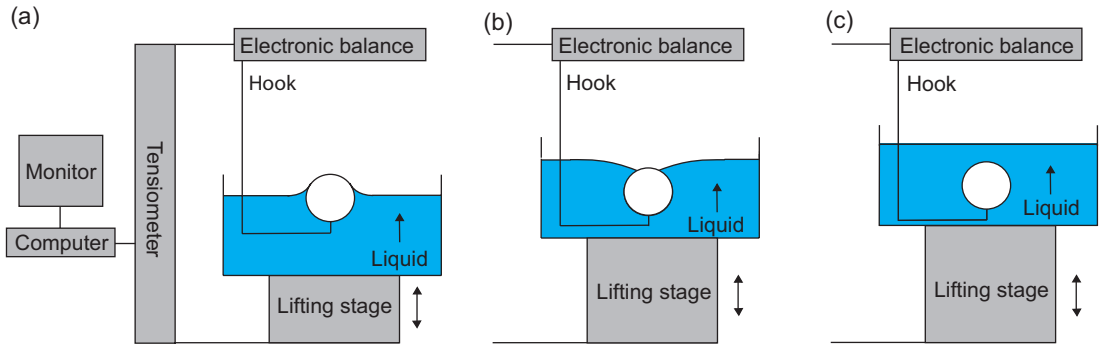

Figure 5.13: Force measurement schematic of a spherical particle in contact with a liquid-gas interface using a tensiometer showing different stages of particle positions with respect to the liquid-gas interface.

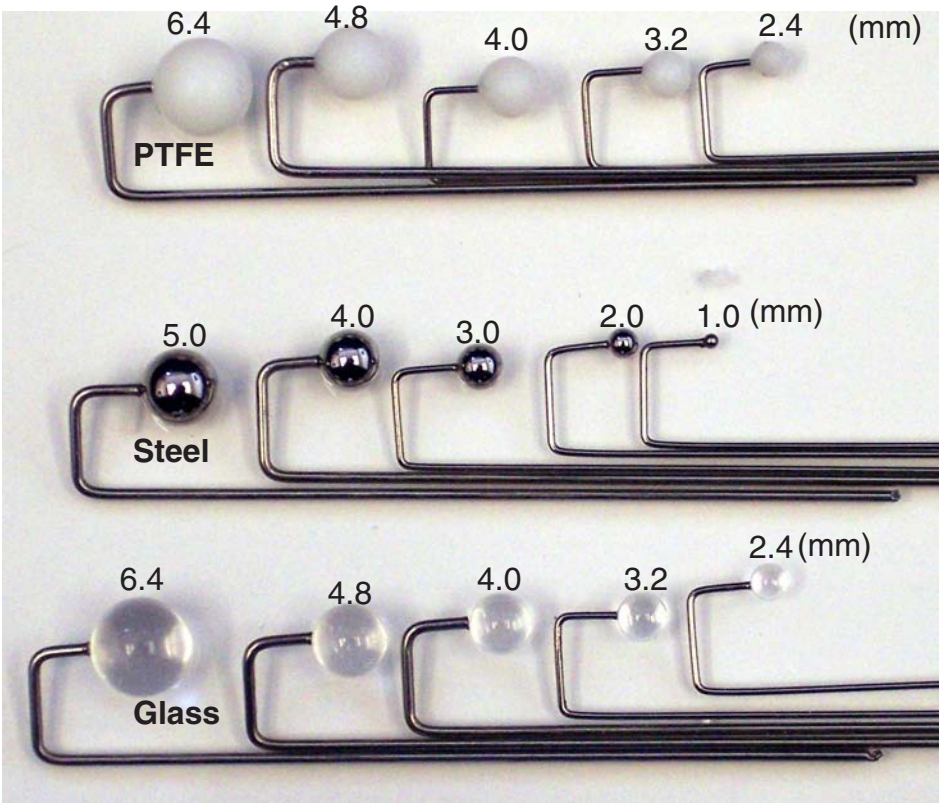

Figure 5.14: Five different radii spheres (glass, steel, PTFE) with hooks.

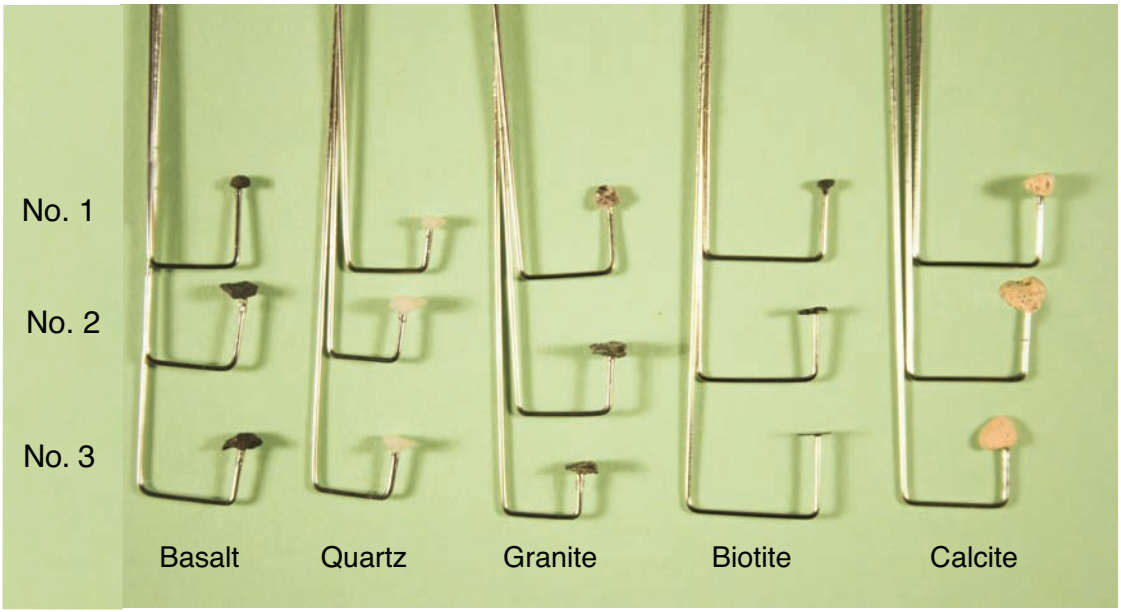

Figure 5.15: Irregular shaped, natural Hanford sediment particles (basalt, quartz, granite, biotite, and calcite) with hooks.

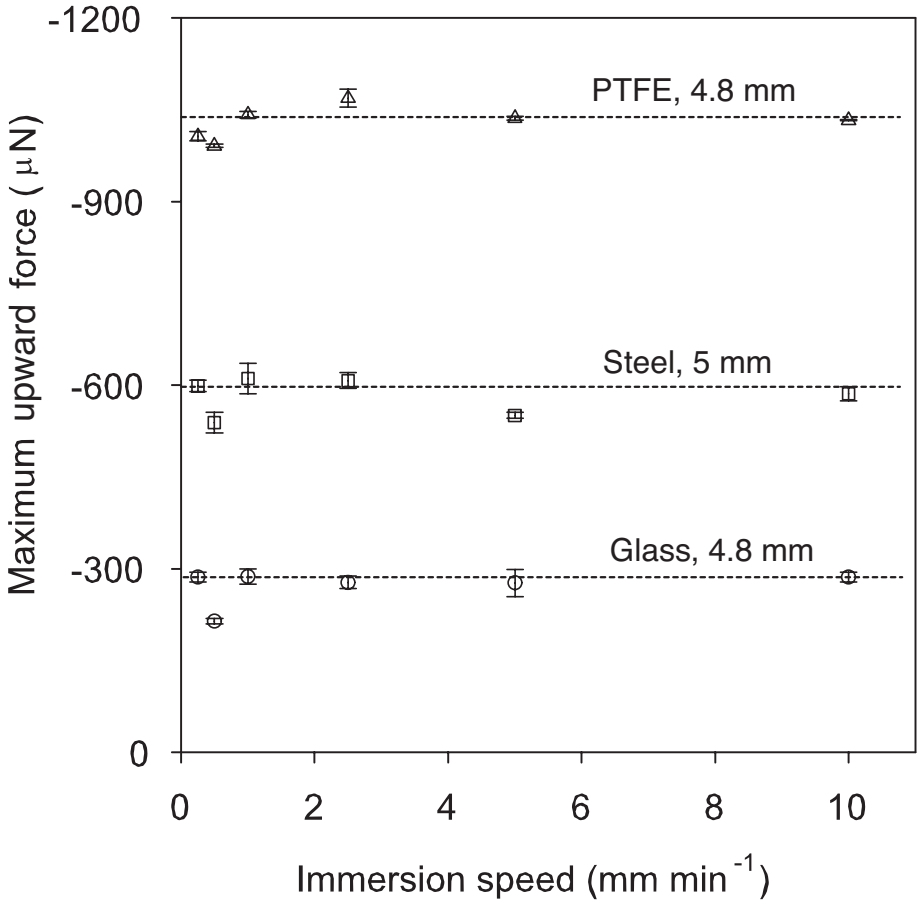

Figure 5.16: Maximum upward force (μN) of glass, steel, and PTFE beads immersed into water at different speeds (mm min^{-1}).

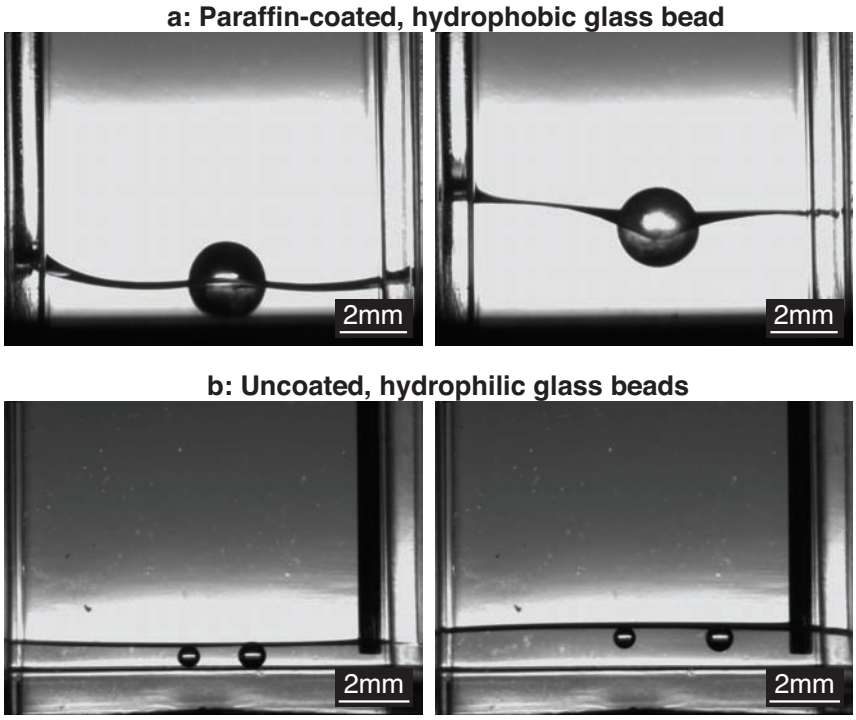

Figure 5.17: (a) Capillary, and buoyancy force can overcome the weight of a paraffin-coated, hydrophobic glass bead ($\theta = 108.9^o$, 2 mm in diameter) and lift the bead along with a raising air-water interface; (b) uncoated, hydrophilic glass beads ($\theta = 64.0^o$, 0.8 mm in diameter) can be lifted up too. Supplementary video files show the dynamics of the detachment.

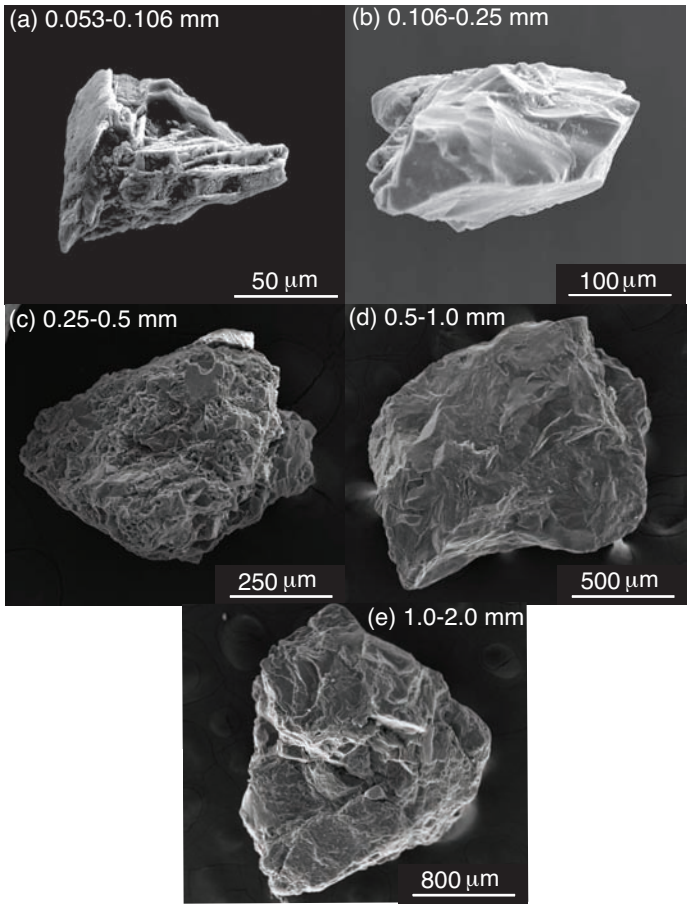

Figure 5.18: Irregular shapes of natural Hanford sediments in the five particle size groups: (a) 0.053−0.106 mm, (b) 0.106−0.25 mm, (c) 0.25−0.5 mm, (d) 0.5−1 mm, and (e) 1−2 mm.

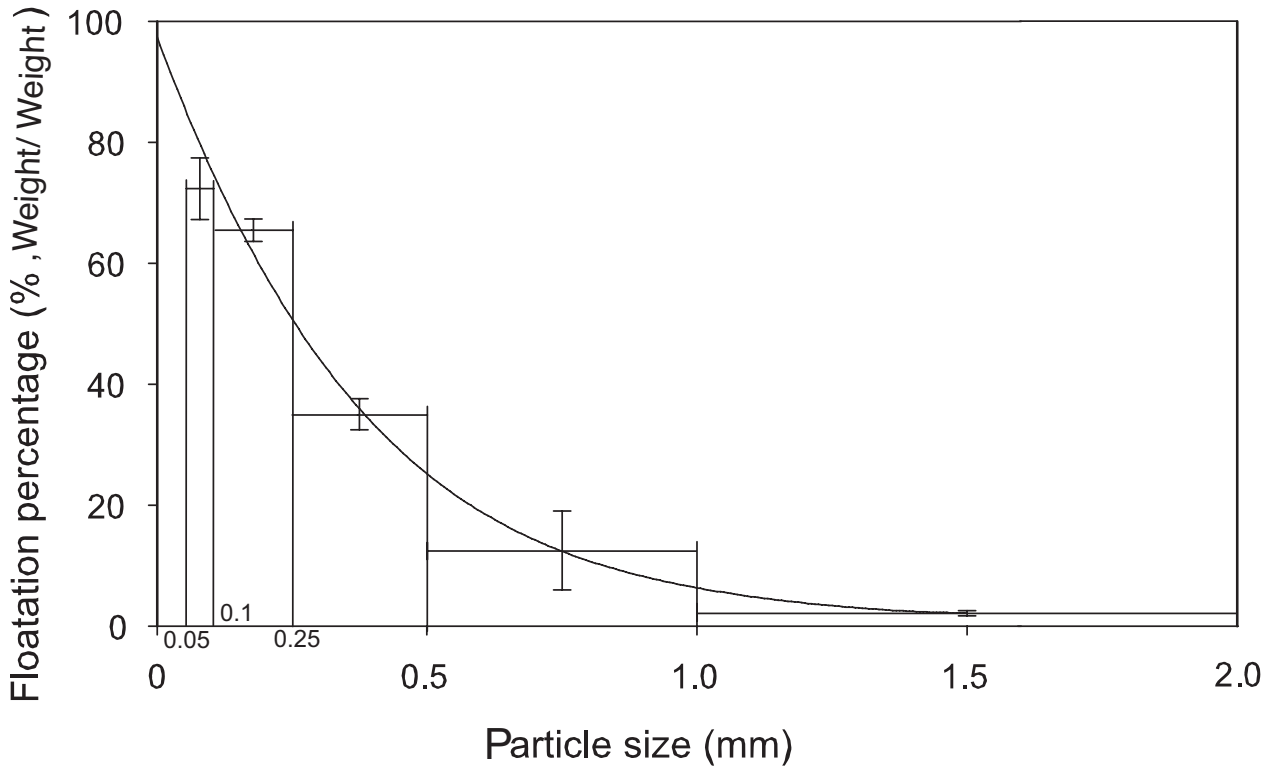

Figure 5.19: Flotation percentages of natural Hanford sediments as a function of average particle size. Vertical error bars denote ± one standard deviation. Solid line is an exponential trend line.

Chapter 6

Summary and Conclusions

This dissertation includes four topics related to subsurface colloid thermodynamic properties and their effects on colloid transport: (1) impact of flow rate, water content, and capillary forces on *in situ* colloid mobilization during infiltration in unsaturated sediments; (2) comparison of different methods to measure contact angles of subsurface colloids; (3) force measurements between particles and the air-water interface; (4) the effects of relative humidity and cations on contact angle and interfacial energy of subsurface colloids. These studies include column experiments, numerical simulations, contact angle measurements, force measurements.

To test *in situ* colloid mobilization, we used columns repacked with Hanford sediments. Transient flow conditions were experimentally controlled by different flow rates to simulate various infiltration rates. We carried out five series of column experiments with initial infiltration rates of 0.018, 0.036, 0.072, 0.144 and 0.288 cm/min and the degree of water saturation ranged from 53 to 81% under conditions unfavorable for colloid attachment. The results showed that *in situ* colloids were eluted by the infil-

trating water with the peak colloid concentrations in the outflow coinciding with the arrival of the infiltration front. When the flow rate was larger, the amount of colloids released from the column was greater. The advection-dispersion equation with a first-order colloid release reaction was used to analyze the experimental data, and we found that the colloid release rate coefficient increased with the increase of water content. To elucidate the mechanism of colloid mobilization, we calculated hydrodynamic, capillary, electrostatic and van der Waals forces exerted on colloids, and found that capillary forces played a prominent role in controlling colloid release.

However, capillary forces are difficult to determine unless we can measure the contact angles of colloids. Making meaningful contact angle measurements for subsurface colloids is a complex problem because of small particle size, irregular shape, and various surface charge. To compare and find optimal contact angle methods for subsurface colloids, five different methods, static sessile drop, dynamic sessile drop, Wilhelmy plate, thin-layer wicking, and column wicking were used to determine the contact angle of typical subsurface colloids. We found that the static and dynamic sessile drop methods yielded the most consistent contact angles. The time-depedent contact angle for the static sessile drop was caused by liquid-solid interactions (e.g., smectite) or imbibition of liquid (e.g., kaolinite). For porous films, the contact angles decreased with time, and we consider the initial contact angle to be the most accurate.

We investigated the effects of relative humidity and cations on contact angles and surface tensions of subsurface colloids. The results showed that cations caused different

contact angles with water and formamide, but had no effects on contact angles with diiodomethane. Different cations Na^+, K^+, Mg^{2+}, and Ca^{2+} had similar effects on contact angle measurements. The contact angles of polar liquids changed randomly with humidity, and the contact angles of apolar liquid increased with humidity. The calculations using the acid-base approach showed that cations had no effects on γ_s^{LW}, and that relative humidity decreased γ_s^{LW}.

To show that capillary forces can cause strong repulsion of particles from stationary surfaces, we measured and theoretically calculated theoretical maximum capillary forces. Using tensiometer technology, we measured the maximum repulsive capillary force between a sphere, cylinder, cube, disk, sheet, or natural particle, and the air-water interface. Attractive and maximum repulsive forces acting on a spherical particle in contact with an air-water interface were calculated as a function of surface charge, particle radius, or contact angle. We found that capillary forces acting at the air-water interface caused strong repulsion of particles from the stationary surfaces when water films expanded or moved through the porous medium. The maximum repulsive capillary forces were similar to our theoretical calculations. The calculations showed that the maximum repulsive capillary force was larger than attractive DLVO forces and was a dominant force in colloid mobilization in unsaturated soil and sediments. No matter whether the surface charge was small or large, positive or negative, the maximum capillary forces were larger than attractive DLVO forces. When contact angles $\theta > 15.9^o$, repulsive capillary forces were dominant forces for typical subsurface particles with ra-

dius of 250 nm. When the particles were smaller, the repulsive capillary force became more dominant. In addition, a rough and irregular surface shape caused the capillary force to increase as compared to a smooth, spherical shape, making natural particles susceptible to detachment and mobilization due to moving air-water interfaces.

Bibliography

Abe, K., H. Takiguchi, and K. Tamada, Dynamic contact angle measurement of Au(111)-thiol self-assembled monolayers by the Wilhelmy plate method, *Langmuir*, *16*, 2394–2397, 2000.

Abu-Lail, N. I., and T. A. Camesano, The effect of solvent polarity on the molecular surface properties and adhesion of Escherichia coli, *Colloids Surf. Biointerfaces*, *51*, 62–70, 2006.

Bachmann, J., A. Ellies, and K. H. Hartge, Development and application of a new sessile drop contact angle method to assess soil water repellency, *J. Hydrol. (Amsterdam)*, *231*, 66–75, 2000a.

Bachmann, J., M. Deurer, and G. Arye, Modeling water movement in heterogeneous water-repellent soil: 1. Development of a contact angle-dependent water-retention model, *Vadose Zone J.*, *6*, 436–445, 2007.

Bachmann, J., R. Horton, R. R. V. D. Ploeg, and S. Woche, Modified sessile drop method for assessing initial soil- water contact angle of sandy soil, *Soil Sci. Soc.*

Am. J., *64*, 564–567, 2000b.

Bachmann, J., S. K. Woche, and M. O. Goebel, Extended methodology for determining wetting properties of porous media, *Water Resour. Res.*, *39*, 1353, doi:10.1029/2003WR002143, 2003.

Breiner, J. M., M. A. Anderson, H. W. K. Tom, and R. C. Graham, Properties of surface-modified colloidal particles, *Clays Clay Miner.*, *54*, 12–24, 2006.

Chassin, P., C. Jounay, and H. Quiquampoix, Measurement of the surface free-energy of calcium-montmorillonite, *Clay Miner.*, *21*, 899–907, 1986.

Chateau, X., P. Moucheront, and O. Pitois, Micromechanics of unsaturated granular media, *J. Eng. Mech.*, *128*, 856–863, 2002.

Chen, G., and M. Flury, Retention of mineral colloids in unsaturated porous media as related to their surface properties, *Colloids Surf. Physicochem. Eng. Aspects*, *256*, 207–216, 2005.

Chenu, C., Y. Le Bissonnais, and D. Arrouays, Organic matter influence on clay wettability and soil aggregate stability, *Soil Sci. Soc. Am. J.*, *64*, 1479–1486, 2000.

Cherrey, K. D., M. Flury, and J. B. Harsh, Nitrate and colloid transport through coarse Hanford sediments under steady state, variably saturated flow, *Water Resour. Res.*, *39*, 1165, doi:10.1029/2002WR001944, 2003.

Chibowski, E., and F. González-Caballero, Theory and practice of thin-layer wicking, *Langmuir*, *9*, 330–340, 1993.

Chibowski, E., and L. Holysz, Use of the Washburn equation for surface free energy determination, *Langmuir*, *8*, 710–716, 1992.

Chibowski, E., and R. Perea-Carpio, Problems of contact angle and solid surface free energy determination, *Adv. Colloid Interface Sci.*, *98*, 245–264, 2002.

Chibowski, E., M. L. Kerkeb, and F. González-Caballero, Effect of inorganic-ions on changes in the energetic heterogeneity of the cholesterol surface, *Langmuir*, *9*, 2491–2495, 1993.

Chipera, S. J., and D. L. Bish, Baseline studies of the clay minerals society source clays: Powder x-ray diffraction analyses, *Clays Clay Miner.*, *49*, 398–409, 2001.

Chorom, M., and P. Rengasamy, Dispersion and zeta potential of pure clays as related to net particle charge under varying pH, electrolyte concentration and cation type, *Eur. J. Soil Sci.*, *46*, 657–665, 1995.

Cooper, R., V. Thoss, and H. Watson, Factors influencing the release of dissolved organic carbon and dissolved forms of nitrogen from a small upland headwater during autumn runoff events, *Hydrol. Processes*, *21*, 622–633, 2007.

Costanzo, P. M., W. Wu, R. F. Giese, and C. J. van Oss, Comparison between direct contact angle measurements and thin layer wicking on synthetic monosized cuboid hematite particles, *Langmuir*, *11*, 1827–1830, 1995.

Crist, J. T., Y. Zevi, J. F. McCarthy, J. A. Troop, and T. S. Steenhuis, Transport and retention mechanisms of colloids in partially saturated porous media, *Vadose Zone J.*, *4*, 184–195, 2005.

Czigany, S., M. Flury, and J. B. Harsh, Colloid stability in vadose zone Hanford sediments, *Environ. Sci. Technol.*, *39*, 1506–1512, 2005.

Dahneke, B., Kinetic theory of the escape of particles from surfaces, *J. Colloid Interface Sci.*, *50*, 89–107, 1975.

de Jonge, H., O. Jacobsen, L. de Jonge, and P. Moldrup, Particle-facilitated transport of prochloraz in undisturbed sandy loam soil columns, *J. Environ. Qual.*, *27*, 1495–1503, 1998.

de Jonge, L. W., P. Moldrup, G. H. Rubk, K. Schelde, and J. Djurhuus, Particle leaching and particle-facilitated transport of phosphorus at field scale, *Vadose Zone J.*, *3*, 462–470, 2004.

DeJonge, L. W., O. H. Jacobsen, and P. Moldrup, Soil water repellency: Effects of water content, temperature, and particle size, *Soil Sci. Soc. Am. J.*, *63*, 437–442, 1999.

deJonge, L. W., P. Moldrup, and O. H. Jacobsen, Soil-water content dependency of water repellency in soils: Effect of crop type, soil management, and physical-chemical parameters, *Soil Sci.*, *172*, 577–588, 2007.

Dekker, L. W., and C. J. Ritsema, Wetting patterns and moisture variability in water repellent Dutch soils, *J. Hydrol. (Amsterdam)*, *231*, 148–164, 2000.

Dekker, L. W., C. J. Ritsema, K. Oostindie, and O. H. Boersma, Effect of drying temperature on the severity of soil water repellency, *Soil Sci.*, *163*, 780–796, 1998.

Dekker, L. W., S. H. Doerr, K. Oostindie, A. K. Ziogas, and C. J. Ritsema, Water repellency and critical soil water content in a dune sand, *Soil Sci. Soc. Am. J.*, *65*, 1667–1674, 2001.

Dettre, R. H., and R. E. J. Johnson, Contact angle hysteresis. IV. Contact angle measurements on heterogeneous surfaces, *J. Phys. Chem.*, *69*, 1507–1515, 1965.

Drelich, J., J. Miller, and R. Good, The effect of drop (bubble) size on advancing and receding contact angles for heterogeneous and rough solid surfaces as observed with sessile-drop and captive-bubble techniques, *J. Colloid Interface Sci.*, *179*, 37–50, 1996.

Ecke, S., M. Preuss, and H. J. Butt, Microsphere tensiometry to measure advancing and receding contact angles on individual particles, *J. Adhes. Sci. Technol.*, *13*, 1181–1191, 1999.

Eick, J., R. Good, and A. Neumann, Thermodynamics of contact angles. II. Rough solid surfaces, *J. Colloid Interface Sci.*, *53*, 235–238, 1975.

El-Farhan, Y. H., N. M. Denovio, J. S. Herman, and G. M. Hornberger, Mobilization and transport of soil particles during infiltration experiments in an agricultural field, Shenandoah valley, Virginia, *Environ. Sci. Technol.*, *34*, 3555–3559, 2000.

Elimelech, M., J. Gregory, X. Jia, and R. A. Williams, *Particle Deposition and Aggregation: Measurement, Modelling, and Simulation*, Butterworth-Heinemann, Oxford, 1995.

Fieber, C., and H. Sonntag, Theoretical consideration on the applicability of the sphere method for measuring interfacial tension and contact angle, *Colloid Polymer Sci.*, *257*, 874–881, 1979.

Flury, M., and N. N. Wai, Dyes as tracers for vadose zone hydrology, *Rev. Geophys.*, *41*, 1002, doi:10.1029/2001RG000109, 2003.

Flury, M., J. B. Mathison, and J. B. Harsh, *In situ* mobilization of colloids and transport of cesium in Hanford sediments, *Environ. Sci. Technol.*, *36*, 5335–5341, 2002.

Gao, B., J. E. Saiers, and J. N. Ryan, Deposition and mobilization of clay colloids in unsaturated porous media, *Water Resour. Res.*, *40*, W08602, doi:10.1029/2004WR003189, 2004.

Gao, B., J. E. Saiers, and J. N. Ryan, Pore-scale mechanisms of colloid deposition and mobilization during steady and transient flow through unsaturated granular media, *Water Resour. Res.*, *42*, W01410, doi:10.1029/2005WR004233, 2006.

Gao, B., T. S. Steenhuis, Y. Zevi, V. L. Morales, J. L. Nieber, B. K. Richards, J. F. McCarthy, and J.-Y. Parlange, Capillary retention of colloids in unsaturated porous media, *Water Resour. Res.*, *44*, W04504, doi:10.1029/2006WR005332, 2008.

Giese, R. F., and C. J. van Oss, *Colloid and Surface Properties of Clays and Related Minerals*, CRC Press, Oxford, 2002.

Giese, R. F., P. M. Costanzo, and C. J. van Oss, The surface free energies of talc and pyrophyllite, *Phys. Chem. Miner.*, *17*, 611–616, 1991.

Gillies, G., M. Kappl, and H. Butt, Direct measurements of particle-bubble interactions, *Adv. Colloid Interface Sci.*, *114*, 165–172, 2005.

Gish, T. J., K. J. S. Kung, D. C. Perry, J. Posner, G. Bubenzer, C. S. Helling, E. J. Kladivko, and T. S. Steenhuis, Impact of preferential flow at varying irrigation rates by quantifying mass fluxes, *J. Environ. Qual.*, *33*, 1033–1040, 2004.

Goebel, M., J. Bachmann, S. K. Woche, W. R. Fischer, and R. Horton, Water potential and aggregate size effects on contact angle and surface energy, *Soil Sci. Soc. Am. J.*, *68*, 383–393, 2004.

Gregory, J., Interaction of unequal double layers at constant charge, *J. Colloid Interface Sci.*, *51*, 44–51, 1975.

Gregory, J., Approximate expressions for retarded van der Waals interaction, *J. Colloid Interface Sci.*, *83*, 138–145, 1981.

Grolimund, D., and M. Borkovec, Long-term release kinetics of colloidal particles from natural porous media, *Environ. Sci. Technol.*, *33*, 4054–4060, 1999.

Grolimund, D., K. Barmettler, and M. Borkovec, Release and transport of colloidal particles in natural porous media. 1. Modeling, *Water Resour. Res.*, *37*, 559–570, 2001.

Grolimund, D., M. Borkovec, K. Barmettler, and H. Sticher, Colloid-facilitated transport of strongly sorbing contaminants in natural porous media: a laboratory column study, *Environ. Sci. Technol.*, *30*, 3118–3123, 1996.

Gschwend, P. M., D. A. Backhus, J. K. MacFarlane, and A. L. Page, Mobilization of colloids in groundwater due to inltration of water at a coal ash disposal site, *J. Contam. Hydrol.*, *6*, 307–320, 1990.

Gunde, R., S. Hartland, and R. Mader, Sphere tensiometry: a new approach to simultaneous and independent determination of surface tension and contact angle, *J. Colloid Interface Sci.*, *176*, 17–30, 1995.

Hadjiiski, A., R. Dimova, N. D. Denkov, I. B. Ivanov, and R. Borwankar, Film trapping technique: Precise method for three-phase contact angle determination of solid and fluid particles of micrometer size, *Langmuir*, *12*, 6665–6675, 1996.

Harris, R. F., Effect of water potential on microbial growth and activity, in *Water Potential Relations in Soil Microbiology*, edited by J. F. Parr, W. R. Gardner, and L. F. Elliot, pp. 23–95, Soil Science Society of America, Madison, WI, 1981.

Hesla, T. I., and D. D. Joseph, The maximum contact angle at the rim of a heavy floating disk, *J. Colloid Interface Sci.*, *279*, 186–191, 2004.

Hiemenz, P. C., and R. Rajagopalan, *Principles of Colloid and Surface Chemistry*, 3rd ed., Marcel Dekker, New York, 1997.

Hough, D. B., and L. R. White, The calculation of Hamaker constants from Liftshitz theory with applications to wetting phenomena, *Adv. Colloid Interface Sci.*, *14*, 3–41, 1980.

Huh, C., and S. G. Mason, The flotation of axisymmetric particles at horizontal liquid interfaces, *J. Colloid Interface Sci.*, *47*, 271–289, 1974.

Huh, C., and S. G. Mason, Sphere tensiometry: an evaluation and critique, *Canadian J. Chem.*, *54*, 969–978, 1976.

Hunter, R. J., *Foundations of Colloid Science*, 2nd ed., Oxford University Press, Oxford, 2001.

Jerez, J., M. Flury, J. Shang, and Y. Deng, Coating of silica sand with aluminosilicate clays, *J. Colloid Interface Sci.*, *294*, 155–164, 2006.

Johnson, R. E. J., and R. H. Dettre, Contact angle hysteresis. III. Study of an idealized heterogeneous surface, *J. Phys. Chem.*, *68*, 1744–1750, 1964.

Kaiser, K., and W. Zech, Rates of dissolved organic matter release and sorption in forest soils, *Soil Sci.*, *163*, 714–725, 1998.

Kaplan, D. I., P. M. Bertsch, and D. C. Adriano, Mineralogical and physicochemical differences between mobile and nonmobile colloidal phases in reconstructed pedons, *Soil Sci. Soc. Am. J.*, *61*, 641–649, 1997.

Kaplan, D. I., P. M. Bertsch, D. C. Adriano, and W. P. Miller, Soil-borne mobile colloids as influenced by water flow and organic carbon, *Environ. Sci. Technol.*, *27*, 1193–1200, 1993.

Karagúzel, C., M. F. Can, E. Sónmez, and M. S. Celik, Effect of electrolyte on surface free energy components of feldspar minerals using thin-layer wicking method, *J. Colloid Interface Sci.*, *285*, 192–200, 2005.

King, P. M., Comparison of methods for measuring severity of water repellence of sandy soils and assessment of some factors that affect its measurement, *Aust. J. Soil Res.*, *19*, 275–285, 1981.

Kjaergaard, C., T. Poulsen, P. Moldrup, and L. W. de Jonge, Colloid mobilization and transport in undisturbed soil columns. I. Pore structure characterization and tritium transport, *Vadose Zone J.*, *3*, 413–423, 2004.

Klitzke, S., and F. Lang, Hydrophobicity of soil colloids and heavy metal mobilization: Effects of drying, *J. Environ. Qual.*, *36*, 1187–1193, 2007.

Kretzschmar, R., M. Borkovec, D. Grolimund, and M. Elimelech, Mobile subsurface colloids and their role in contaminant transport, *Adv. Agron.*, *66*, 121–193, 1999.

Kretzschmar, R., W. P. Robarge, and A. Amoozegar, Influence of natural organic-matter on colloid transport through saprolite, *Water Resour. Res.*, *31*, 435–445, 1995.

Kukavica-Ibrulj, I., A. Darveau, J. Jean, and I. Fliss, Hepatitis A virus attachment to agri-food surfaces using immunological, virological and thermodynamic assays, *J. Appl. Microbiol.*, *97*, 923–934, 2004.

Kung, K. J. S., M. Hanke, C. S. Helling, E. J. Kladivko, T. J. Gish, T. S. Steenhuis, and D. B. Jaynes, Quantifying pore-size spectrum of macropore-type preferential pathways, *Soil Sci. Soc. Am. J.*, *69*, 1196–1208, 2005.

Kwok, D., C. Lam, A. Li, A. Leung, R. Wu, E. Mok, and A. Neumann, Measuring and interpreting contact angles: a complex issue, *Colloids Surf. Physicochem. Eng. Aspects*, *142*, 219–235, 1998.

Kwok, D., R. Lin, M. Mui, and A. Neumann, Low-rate dynamic and static contact angles and the determination of solid surface tensions, *Colloids Surf. Physicochem. Eng. Aspects*, *116*, 63–77, 1996.

Kwok, D. Y., and A. W. Neumann, Contact angle measurement and contact angle interpretation, *Adv. Colloid Interface Sci.*, *81*, 167–249, 1999.

Laegdsmand, M., K. G. Villholth, M. Ullum, and K. H. Jensen, Processes of colloid mobilization and transport in macroporous soil monoliths, *Geoderma*, *93*, 33–59, 1999.

Laegdsmand, M., L. W. de Jonge, and P. Moldrup, Leaching of colloids and dissolved organic matter from columns packed with natural soil aggregates, *Soil Sci.*, *170*, 13–27, 2005.

Lam, C. N. C., N. Kim, D. Hui, D. Y. Kwok, M. L. Hair, and A. W. Neumann, The effect of liquid properties to contact angle hysteresis, *Colloids Surf. Physicochem. Eng. Aspects*, *189*, 265–278, 2001.

Lam, C. N. C., R. Wu, D. Li, M. L. Hair, and A. W. Neumann, Study of the advancing and receding contact angles: liquid sorption as a cause of contact angle hysteresis, *Adv. Colloid Interface Sci.*, *96*, 169–191, 2002.

Lenhart, J. J., and J. E. Saiers, Colloid mobilization in water-saturated porous media under transient chemical conditions, *Environ. Sci. Technol.*, *37*, 2780–2787, 2003.

Levin, J. M., J. S. Herman, G. M. Hornberger, and J. E. Saiers, Colloid mobilization from a variably saturated, intact soil core, *Vadose Zone J.*, *5*, 564–569, 2006.

Li, Z., R. F. Giese, and C. J. van Oss, Surface thermodynamic properties of synthetic hydrotalcite compounds, *Langmuir*, *10*, 330–333, 1994.

Long, J., M. Hyder, R. Huang, and P. Chen, Thermodynamic modeling of contact angles on rough, heterogeneous surfaces, *Adv. Colloid Interface Sci.*, *118*, 173–190, 2005.

Low, P. F., Principles of ion diffusion in clays, in *Chemistry in the Soil Environment*, edited by D. E. Baker, pp. 31–45, ASA Special Publication No. 40, American Society of Agronomy, Madison, WI, 1981.

Majdalani, S., E. Michel, L. Di-Pietro, and R. Angulo-Jaramillo, Effects of wetting and drying cycles on in situ particle mobilization, *Eur. J. Soil Sci.*, 2007.

Marion, G. M., and K. L. Babcock, Predicting specific conductance and salt concentrations of dilute aqueous solution, *Soil Sci.*, *122*, 181–187, 1976.

Mashal, K., J. B. Harsh, M. Flury, A. R. Felmy, and H. Zhao, Colloid formation in Hanford sediments reacted with simulated tank waste, *Environ. Sci. Technol.*, *38*, 5750–5756, 2004.

McBride, M. B., Surface chemistry of soil minerals, in *Minerals in the Soil Environment*, edited by J. B. Dixon, and S. B. Weed, pp. 35–88, Soil Science Society of America, Madison, WI, 1989.

McCarthy, J. F., Colloid-facilitated transport of contaminants in groundwater: mobilization of transuranic radionuclides from disposal trenches by natural organic matter, *Phys. Chem. Earth*, *23*, 171–178, 1998.

McCarthy, J. F., and C. Degueldre, Sampling and characterization of groundwater colloids for studying their role in the subsurface transport of contaminants, in *Environmental Particles*, vol. II, edited by J. Buffle, and H. van Leeuwen, pp. 247–315, Lewis Publisher, Boca Raton, FL, 1993.

McCarthy, J. F., and J. M. Zachara, Subsurface transport of contaminants, *Environ. Sci. Technol.*, *23*, 496–502, 1989.

McCarthy, J. F., and L. D. McKay, Colloid transport in the subsurface: Past, present, and future challenges, *Vadose Zone J.*, *3*, 326–337, 2004.

Mermut, A. R., and G. Lagaly, Baseline studies of the clay minerals society source clays: Layer-charge determination and characteristics of those minerals containing $2:1$ layers, *Clays Clay Miner.*, *49*, 393–397, 2001.

Michel, J. C., L. M. Riviere, and M. N. Bellon-Fontaine, Measurement of the wettability of organic materials in relation to water content by the capillary rise method, *Eur. J. Soil Sci.*, *52*, 459–467, 2001.

Mohammadi, R., and A. Amirfazli, Contact angle measurement for dispersed microspheres using scanning confocal microscopy, *J. Dispersion Sci. Technol.*, *25*, 567–574, 2004.

Oliver, J., C. Huh, and S. Mason, An experimental study of some effects of solid surface roughness on wetting, *Colloids Surf.*, *1*, 79–104, 1980.

Papendick, R. I., and G. S. Campbell, Theory and measurement of water potential, in *Water Potential Relations in Soil Microbiology*, edited by J. F. Parr, W. R. Gardner, and L. F. Elliot, pp. 1–22, Soil Science Society of America, Madison, WI, 1981.

Paunov, V. N., Novel method for determining the three-phase contact angle of colloid particles adsorbed at air-water and oil-water interfaces, *Langmuir*, *19*, 7970–7976, 2003.

Petersen, C., J. Holm, C. Koch, H. Jensen, and S. Hansen, Movement of pendimethalin, ioxynil and soil particles to field drainage tiles, *Pest. Manage. Sci.*, *59*, 85–96, 2003.

Pitois, O., and X. Chateau, Small particle at a fluid interface: Effect of contact angle hysteresis on force and work of detachment, *Langmuir*, *18*, 9751–9756, 2002.

Preuss, M., and H. Butt, Direct measurement of particle-bubble interactions in aqueous electrolyte: dependence on surfactant, *Langmuir*, *14*, 3146–3174, 1998a.

Preuss, M., and H. J. Butt, Direct measurement of particle-bubble interactions in aqueous electrolyte: Dependence on surfactant, *Langmuir*, *14*, 3164–3174, 1998b.

Preuss, M., and H. J. Butt, Measuring the contact angle of individual colloidal particles, *J. Colloid Interface Sci.*, *208*, 468–477, 1998c.

Preuss, M., and H. J. Butt, Direct measurement of forces between particles and bubbles, *Int. J. Miner. Process.*, *56*, 99–115, 1999.

Princen, H. M., Equilibrium shape of interfaces, drops, and bubbles. Rigid and deformable particles at interfaces, *Surface Colloid Sci.*, *2*, 1–84, 1969.

Raymond, L., and J. Kerns, Structural charge site influence on the interlayer hydration of expandable three-sheet clay minerals, *Clays Clay Miner.*, *16*, 73–81, 1967.

Roy, S. B., and D. A. Dzombak, Colloid release and transport processes in natural and model porous media, *Colloids Surf. Physicochem. Eng. Aspects*, *107*, 245–262, 1996.

Ruckenstein, E., and D. C. Prieve, Adsorption and desorption of particles and their chromatographic separation, *AIChE J.*, *22*, 276–283, 1976.

Ryan, J. N., and M. Elimelech, Colloid mobilization and transport in groundwater, *Colloids Surf. Physicochem. Eng. Aspects*, *107*, 1–56, 1996.

Ryan, J. N., and P. M. Gschwend, Chemical conditions conducive to the release of mobile colloids from Ultisol profiles, *Environ. Sci. Technol.*, *28*, 1717–1726, 1994.

Ryan, J. N., T. H. Illangasekare, M. I. Litaor, and R. Shannon, Particle and plutonium mobilization in macroporous soils during rainfall simulations, *Environ. Sci. Technol.*, *32*, 476–482, 1998.

Saiers, J. E., and J. J. Lenhart, Colloid mobilization and transport within unsaturated porous media under transient-flow conditions, *Water Resour. Res.*, *39*, 1019, doi:10.1029/2002WR001370, 2003.

Schelde, K., P. Moldrup, O. H. Jacobsen, H. de Jonge, L. W. de Jonge, and K. Komatsu, Diffusion-limited mobilization and transport of natural colloids in unsaturated macroporous soil, *Vadose Zone J.*, *1*, 125–136, 2002.

Scheludko, A., B. V. Toshev, and D. T. Bojadjiev, Attachment of particles to a liquid surface (Capillary theory of flotation), *J. Chem. Soc. Faraday Trans. I*, *72*, 2815–2828, 1976.

Schulze, H. D., New theoretical and experimental investigations on the stability of bubble/particle aggregates in flotation: a theory on the upper particle size on floatability, *Int. J. Mineral Processing*, *4*, 241–259, 1977.

Schwertmann, U., and R. M. Cornell, *Iron Oxides in the Laboratory: Preparation and Characterization*, VCH, Weinheim, 1991.

Sen, T. K., and K. C. Khilar, Review on subsurface colloids and colloid-associated contaminant transport in saturated porous media, *Adv. Colloid. Interface Sci.*, *119*, 71–96, 2006.

Sen, T. K., S. Shanbhag, and K. C. Khilar, Subsurface colloids in groundwater contamination: a mathematical model, *Colloids Surf. Physicochem. Eng. Aspects*, *232*, 29–38, 2004.

Shang, J., M. Flury, G. Chen, and J. Zhuang, Impact of flow rate, water content, and capillary forces on in situ colloid mobilization during infiltration in unsaturated sediments, *Water Resour. Res.*, *44*, DOI10.1029/2007WR006516, 2008a.

Shang, J., M. Flury, J. B. Harsh, and R. L. Zollars, Comparison of different methods to measure contact angles of subsurface colloids, *J. Colloid Interface Sci.*, pp. In review, 2008b.

Sharma, M. S., H. Chamoun, D. S. H. Sita Rama Sarma, and R. S. Schechter, Factors controlling the hydrodynamic detachment of particles from surfaces, *J. Colloid Interface Sci.*, *149*, 121–134, 1992.

Sharma, P., H. M. Abdou, and M. Flury, Effect of the lower boundary condition and flotation on colloid mobilization in unsaturated sandy sediments, *Vadose Zone J.*, *7*, in press, 2008.

She, H. Y., and B. Sleep, The effect of temperature on capillary pressure-saturation relationships for air-water and perchloroethylene-water systems, *Water Resour. Res.*, *34*, 2587–2597, 1998.

Siebold, A., A. Walliser, M. Nordin, M. Oppliger, and J. Schultz, Capillary rise for thermodynamic characterization of solid particle surface, *J. Colloid Interface Sci.*, *186*, 60–70, 1997.

Simunek, J., K. Huang, and M. T. van Genuchten, *The HYDRUS Code for Simulating the One-Dimensional Movement of Water, Heat and Multiple Solutes in Variably-Saturated Media*, Research report No. 144, U.S. Salinity Laboratory, Agricultural Research Service, U.S. Department of Agriculture, Riverside, 1998.

Simunek, J., M. T. van Genuchten, D. Jacques, J. W. Hopmans, M. Inoue, and M. Flury, Solute transport during variably saturated flow—inverse methods, in *Methods of Soil Analysis, Part 4, Physical Methods*, edited by J. H. Dane, and G. C. Topp, pp. 1435–1449, Soil Science Society of America, Madison, WI, 2002.

Singh, P., and D. D. Joseph, Fluid dynamics of floating particles, *J. Fluid Mech.*, *530*, 31–80, 2005.

Steenhuis, T., A. Dathe, Y. Zevi, J. L. Smith, B. Gao, S. B. Shaw, D. DeAlwis, S. Amaro-Garcia, R. Fehrman, M. E. Cakmak, I. C. Toevs, B. M. Liu, S. M. Beyer, J. T. Crist, A. G. Hay, B. K. Richards, D. DiCarlo, and J. F. McCarthy, Biocolloid retention in partially saturated soils, *Biologia*, *61*, S229–S233, 2006.

Sur, J., and H. K. Pak, Capillary force on colloidal particles in a freely suspended liquid thin film, *Phys. Rev. Lett.*, *86*, 4326–4329, 2001.

Teixeira, P., J. Azeredo, R. Oliveira, and E. Chibowski, Interfacial interactions between nitrifying bacteria and mineral carriers in aqueous media determined by contact angle measurements and thin layer wicking, *Colloids Surf. Biointerfaces*, *12*, 69–75, 1998.

Tejas, R. D., L. Dongqing, H. F. Warren, and P. W. Jonathan, Determination of surface free energy of interactive dry powder liposome formulations using capillary penetration technique, *Colloids Surf. Biointerfaces*, *22*, 107–113, 2001.

Totsche, K. U., S. Jann, and I. Kögel-Knabner, Single eventdriven export of polycyclic aromatic hydrocarbons and suspended matter from coal tar-contaminated soil, *Vadose Zone J.*, *6*, 233–243, 2007.

Tróger, J., K. Lunkwitz, K. Grundke, and W. Burger, Determination of the surface tension of microporous membranes using wetting kinetics measurements, *Colloids Surf. Physicochem. Eng. Aspects*, *134*, 299–304, 1998.

van Genuchten, M. T., A closed-form equation for predicting the hydraulic conductivity of unsaturated soils, *Soil Sci. Soc. Am. J.*, *44*, 892–898, 1980.

van Oss, C. J., *Interfacial Forces in Aqueous Media*, Marcel Dekker, New York, 1994.

van Oss, C. J., *Interfacial Forces in Aqueous Media*, 2nd ed., CRC Press, New York, 2006.

van Oss, C. J., and C. F. Gillman, Phagocytosis as a surface phenomenon. Contact angles and phagocytosis of non-opsonized bacteria, *J. Reticuloendothel. Soc.*, *12*, 283–292, 1972a.

van Oss, C. J., and C. F. Gillman, Phagocytosis as a surface phenomenon. II. Contact angles and phagocytosis of encapsulated bacteria before and after opsonization by specific antiserum and complement, *J. Reticuloendothel. Soc.*, *12*, 497–502, 1972b.

van Oss, C. J., M. K. Chaudhury, and R. J. Good, Interfacial Lifshitz-van der Waals and polar interactions in macroscopic systems, *Chem. Rev.*, *88*, 927–941, 1988.

van Oss, C. J., R. F. Giese, Z. Li, K. Murphy, J. Norris, M. K. Chaudhury, and R. J. Good, Determination of contact angles and pore sizes of porous media by column and thin-layer wicking, *J. Adhes. Sci. Technol.*, *6*, 413–428, 1992.

Veerapaneni, S., J. Wan, and T. Tokunaga, Motion of particles in film flow, *Environ. Sci. Technol.*, *34*, 2465–2471, 2000.

Wan, J., and T. K. Tokunaga, Measuring partition coefficients of colloids at air-water interfaces, *Environ. Sci. Technol.*, *32*, 3293–3298, 1998.

Wan, J. M., and J. L. Wilson, Colloid transport in unsaturated porous media, *Water Resour. Res.*, *30*, 857–864, 1994.

Wan, J. M., and T. K. Tokunaga, Film straining of colloids in unsaturated porous media: conceptual model and experimental testing, *Environ. Sci. Technol.*, *31*, 2413–2420, 1997.

Wan, J. M., J. L. Wilson, and T. L. Kieft, Influence of the gas-water interface on transport of microorganisms through unsaturated porous media, *Appl. Environ. Microbiol.*, *60*, 509–516, 1994.

Washburn, E., The dynamics of capillary flow, *Phys. Rev.*, *17*, 273–283, 1921.

Woche, S. K., M. O. Goebel, M. B. Kirkham, R. Horton, R. R. Van der Ploeg, and J. Bachmann, Contact angle of soils as affected by depth, texture, and land management, *Eur. J. Soil Sci.*, *56*, 239–251, 2005.

Wu, W., Baseline studies of the Clay Minerals Society source clays: colloid and surface phenomena, *Clays Clay Miner.*, *49*, 446–452, 2001.

Wu, W., J. R. F. Giese, and C. J. van Oss, Change in surface properties of solids caused by grinding, *Powder Technol.*, *89*, 129–132, 1996.

Zevi, Y., A. Dathe, J. F. McCarthy, B. K. Richards, and T. S. Steenhuis, Distribution of colloid particles onto interfaces in partially saturated sand, *Environ. Sci. Technol.*, *39*, 7055–7064, 2005.

Zhang, L., L. Ren, and S. Hartland, More convenient and suitable methods for sphere tensiometry, *J. Colloid Interface Sci.*, *180*, 493–503, 1996.

Zhang, L., L. Ren, and S. Hartland, Detailed analysis of determination of contact angle using sphere tensiometry, *J. Colloid Interface Sci.*, *192*, 306–318, 1997.

Zhang, P., W. P. Johnson, and R. Rowland, Bacterial tracking using ferrographic seperation, *Environ. Sci. Technol.*, *33*, 2456–2460, 1999.

Zhuang, J., J. F. McCarthy, J. S. Tyner, E. Perfect, and M. Flury, In-situ colloid mobilization in Hanford sediments under unsaturated transient flow conditions: Effect of irrigation pattern, *Environ. Sci. Technol.*, *41*, 3199–3204, 2007.

Zhuang, J., M. Flury, and Y. Jin, Colloid-facilitated Cs transport through water-saturated Hanford sediment and Ottawa sand, *Environ. Sci. Technol.*, *37*, 4905–4911, 2003.

Zimon, A. D., *Adhesion of Dust and Powder*, Plenum Press, New York, 1969.